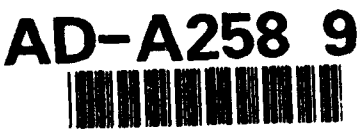

AFIT/GAE/ENY/92D-05

Behavior of a Quasi-Isotropic Ply Metal Matrix Composite Under Thermo-Mechanical and Isothermal Fatigue Loading

THESIS

Karl A. Hart
Captain, USAF

AFIT/GAE/ENY/92D-05

APPROVED FOR PUBLIC RELEASE; DISTRIBUTION UNLIMITED

AFIT/GAE/ENY/92D-05

Behavior of a Quasi-Isotropic Ply Metal Matrix Composite Under Thermo-Mechanical and Isothermal Fatigue Loading

THESIS

Presented to the Faculty of the School of Engineering

of the Air Force Institute of Technology

Air University

In Partial Fulfillment of the

Requirement for the Degree of

Master of Science in Aeronautical Engineering

Karl A. Hart

Captain, USAF

December 1992

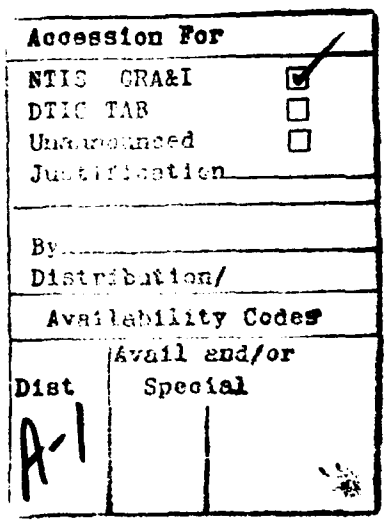

APPROVED FOR PUBLIC RELEASE; DISTRIBUTION UNLIMITED

Acknowledgements

Writing this thesis has been one of the most challenging things I have ever done. I am fortunate in that I enjoyed this struggle so much. The entire project, from start to finish, is an understanding that cannot be appreciated until you actually work on it. One must display commitment, determination, and patience not normally seen day to day.

I owe a lot to God for I believe that He truly inspired me in my writing. I also need to applaud many who have supported my efforts including Mark Derriso and the other lab technicians, they were there to solve my major problems of the day, every day; Bob Lewis and the other metallographers, they taught me how to properly cut and polish specimens to perfect conditions; and Capt Brian Sanders, the resident lab PhD student, he wrote time saving software and provided expert guidance on fatigue testing.

I would like to extend my deepest gratitude to my advisor, Dr. Shankar Mall, for without him, none of this would have been possible. Also, I thank AFOSR in Washington DC for their support in my research.

Lastly and most certainly not the least, I thank my loving wife, Nanette, who was always there even though I wasn't. A final note: this thesis was written in memory of my father, Paul, who passed away during the last year.

Karl A. Hart

Table of Contents

List of Figures

List of Tables

List of Symbols

[A]	Extensional stiffness matrix
B	Empirical constant in the Linear Life Fraction Model
CTE	Coefficient of Thermal Expansion
D	Diameter of fiber
D_o	Diameter of the fiber and interphase region
E, E_x	Longitudinal laminate modulus
E_{d11}	Longitudinal interphase region modulus
E_f, E_{f11}	Longitudinal fiber modulus
E_i	Constituent modulus of elasticity
E_m, E_{m11}	Longitudinal matrix modulus
E_m^*	Modified longitudinal matrix modulus
E_1, E_{111}	Longitudinal ply modulus
E_2	Transverse ply modulus
G_f	Fiber shear modulus
G_i	Constituent shear modulus
G_m	Matrix shear modulus
G_{xy}	In-plane laminate shear modulus
G_{12}	In-plane ply shear modulus
IF	Isothermal fatigue
IP	In-phase
n	Empirical constant in the Linear Life Fraction Model
N	Laminate fatigue life

N_f	Fatigue life due to a fiber dominated failure mode
N_m	Fatigue life due to a matrix dominated failure mode
N_o	Empirical constant in the Linear Life Fraction Model
OP	Out-of-phase
Q_{ij}	Stiffness matrix element
Q_{ij}	Modified stiffness matrix element
R	Load ratio (minimum applied stress over maximum applied stress)
δT, $\delta Temp$	Change in temperature from ambient conditions
TMF	Thermo-mechanical fatigue
V_m	Volume fraction of the matrix
V_f	Volume fraction of the fiber
α	Longitudinal coefficient of thermal expansion of the laminate
α_{l11}	Longitudinal coefficient of thermal expansion of the ply
α_{d11}	Longitudinal coefficient of thermal expansion of the interphase region
α_{f11}	Longitudinal coefficient of thermal expansion of the fiber
α_{m11}	Longitudinal coefficient of thermal expansion of the matrix
β	Correction factor for the room temperature matrix modulus
ϵ_T	Total strain
ϵ_m	Mechanical strain
ϵ_t	Thermal strain

n	Halpin-Tsai modulus factor
ν_f	Fiber Poisson's ratio
ν_m	Matrix Poisson's ratio
ν_{xy}	Major in-plane Poisson's ratio of the laminate
ν_{12}	Major in-plane Poisson's ratio of a ply
ν_{21}	Minor in-plane Poisson's ratio of a ply
$\delta(\sigma_{applied})$	Change in the laminate's applied stress
σ_{f11}	Longitudinal fiber microstress
σ_{111}	Longitudinal ply microstress
σ_{max}	Maximum axial stress in the 0° fiber
$\delta\sigma_m$	Matrix axial stress range
$\delta(\sigma_{mechanical})$	Change in the laminate's mechanical strain
σ_{m11}	Longitudinal matrix microstress
σ^*	Maximum fiber stress at tension failure under static load at 427°C
σ_{11}	Longitudinal tensile stress
σ_{22}	Transverse tensile stress
τ	Correction factor for the elevated temperature matrix modulus
θ	Fiber angle in the ply
ZETA	Geometry and loading parameter for Halpin-Tsai equations

Abstract

The objective of this study was to investigate the behavior of the SCS6/Ti-15-3 metal matrix composite with a quasi-isotropic layup $[0/\pm45/90]_s$, when tested under static and fatigue conditions. Specimens were subjected to low load static tests (to measure longitudinal modulus), an ultimate static strength test, in-phase and out-of-phase thermo-mechanical loading tests, and isothermal fatigue loading tests. For the failure tests, the load, temperature, and strain data were measured and replication, fractography, and metallography were performed to determine both the failure modes and the associated damage mechanisms.

Experimental results indicated in-phase and isothermal loading produced a fracture mode that was more fiber dominated while the out-of-phase loading produced a fracture mode that was more matrix dominated. However, these results also demonstrated a stronger tendency of fiber domination in all three profiles at higher maximum applied loads. Conversely, all three profiles demonstrated a stronger tendency of matrix domination at lower maximum applied loads. Thus, the conclusion can be drawn that the failure is both profile dependent and load dependent.

Additional analyses, using classical laminated plate theory, Halpin-Tsai equations, the Metal Matrix Composite Analyzer (METCAN), and the Linear Life Fraction Model (LLFM), brought further comprehension of the material properties and failure patterns. The metal matrix composite, in the "as-received" condition, contained plies where a portion of the fiber/matrix interfaces were debonded. For the maximum applied stresses chosen in the fatigue testing, the 90° plies and a percentage of the 45° plies failed (fibers debonding from the matrix) immediately with greater damage becoming evident with additional cycles. Also, the out-of-phase cycling exhibited a clear matrix dominated failure mode while the in-phase and isothermal cycling showed a lack of clear domination. The LLFM supports this suggesting that there may be a non-linear combination of fiber and matrix domination for these latter profiles.

Behavior of a Quasi-Isotropic Ply Metal Matrix Composite Under Thermo-Mechanical and Isothermal Fatigue Loading

I. Introduction

A. Background

As the speed of new aerospace vehicles pushes the supersonic and hypersonic speed envelopes, aerodynamic heating and structural weight are becoming even greater factors in the design of these vehicles. Proper vehicle performance, therefore, requires the use of lightweight materials capable of maintaining excellent strength characteristics at elevated temperatures. Examples of these types of vehicles are the Advanced Tactical Fighter and the National Aerospace Plane.

This need for new structural materials has led to the use of composites, mostly because their properties can be tailored in almost any desired direction (hence, aeroelastic tailoring). The tailoring requirement becomes apparent when one studies an aircraft wings' spanwise stiffness which needs to be large to reduce flutter. To save weight, this stiffening can be optimized by increasing it in only one direction. Since this optimization is rather difficult with the sole use of monolithic materials, one can begin to

appreciate the significant advantages of composites.

Composites are generally divided into two different classifications: fiber-reinforced and particle-reinforced. Fiber-reinforced composites are further broken down into single-layered and multi-layered categories (1:4). In the multi-layered, fiber-reinforced category, the primary layups which designers have developed include: uni-directional [0°], cross-ply [0°/90°], and quasi-isotropic [0°/±45°/90°]. Varied use of these different layups allows the designer to change the stiffness of the structure in the desired direction. These requirements come from the accomplishment of detailed static and dynamic stress analyses and early vehicle strength tests.

To combat extreme environmental conditions and enjoy the advantages of composites, material scientists have developed the metal matrix composite (MMC) which has metal as the matrix instead of some derivative form of plastic or glass. One such candidate MMC likely to give positive results, and the target of this study, is SCS6/Ti-15-3, a titanium matrix that is reinforced with silicon carbide fibers.

Titanium is used in this MMC because it has more favorable material properties at elevated temperatures than aluminum, the more commonly employed metal in the aerospace industry. To further improve the strength and stiffness without adding any appreciable weight, reinforcing silicon

carbide fibers are added to the titanium. These fibers have an inner carbon core surrounded by silicon carbide, which are then surrounded by a complex outer shell consisting of alternating layers of silicon and carbon with a non-stoichiometric composition. This particular MMC has a potential use up to 700°C (13:1).

As discussed before, the materials selected must perform just as satisfactorily at elevated temperatures as at room temperatures. This problem becomes more complicated because, as the aerospace vehicle progresses through its service life, it will see many cycles of temperature loading and mechanical loading. These loadings will be in-phase or out-of-phase with each other, or the mechanical loading may occur at a constant temperature. However these loadings are induced, they equate to fatigue which leads to:

1. Crack initiation in a material through plastic deformation. Even though the service life stress levels in the structure may be in the elastic range of the material, local effects may cause stress concentrations to raise the local stresses to the plastic range. These concentrations are due to inclusions, voids, and fiber/matrix interfaces. The resulting plastic deformations furnish the means for fatigue cracking through residual compressive forces encountered during the cyclic removal of the loading (3:57-59).

2. Crack propagation. The way the crack grows must be determined to better understand how the material will behave during its service life. For a composite, the propagation is affected by its constituents: the fibers, the matrix, and the plies.

3. Fatigue fracture. This usually occurs without warning. At every stress level, the number of cycles to failure must be known for any structural component undergoing thermal loading, mechanical loading, or both. For a particular stress level, if the predicted service life of the structural component in question is less than the service life of the aircraft, the component must be redesigned or frequently inspected.

Comprehensive research into these effects of thermal cycling in the SCS6/Ti-15-3 MMC has already been accomplished. A few who have made substantial gains in this area include Pollack and Johnson (19) who performed isothermal fatigue (IF) tests on various layups like the cross ply $[0/90]_{2s}$, the unidirectional ply $[0]_8$, and the quasi-isotropic ply $[0/\pm45/90]_s$ at a frequency of 10 Hz and a constant temperature of 650°C; Gabb et al. (6) who completed static, IF, and thermo-mechanical fatigue (TMF) tests on uniaxial plies, [0] and [90]; and, Majumdar and Newaz (14), (7), who conducted IF (650°C) and TMF (315°C - 650°C) tests on quasi-isotropic layups. Their studies and those of

others will be discussed in greater detail in Chapter II.

B. Problem Definition

Even though SCS6/Ti-15-3 has many benefits over monolithic materials and over more established aluminum based MMC's (such as aluminum-boron), it possesses two drawbacks:

1. The characteristics that distinguish titanium based MMC's is their higher matrix strengths, higher matrix-fiber interface strengths, and their capability to withstand higher temperature environments. These advantages, however, can become possible detriments because of the large difference in the coefficients of thermal expansion between the matrix and the fiber. The outcome is higher stresses and strains at the fiber-matrix interface due to thermal expansion and contraction during the material's service life resulting in weakened interfaces and debonding. This weakening leads to a potentially significant degradation in strength and reliability (14:9).

2. A reaction zone is developed during the manufacturing of the titanium MMC located at the interface between the matrix and the fiber. This zone is critical to the MMC's strength because the titanium reacts with the carbon-rich coating on the fibers which leads to changing interfacial properties during fatigue cycling. Thermal loading further stimulates this reaction thus promoting fatigue damage.

Since these changing interfacial properties are difficult to predict, they must be studied. Also, the type of fatigue damage that occurs at the reaction zone must be analyzed so the material designers can properly modify the material's manufacturing processes to reduce these fatigue effects.

In light of the advantages and disadvantages just discussed and the developments and results of other research, the intent of this thesis is to further examine the service life and failure mechanisms of unnotched SCS6/Ti-15-3 specimens. These specimens were subjected to various maximum applied stress levels and three different loading profiles: in-phase fatigue, out-of-phase fatigue, and isothermal fatigue. The temperature range for the thermo-mechanical fatigue tests was 149°C - 427°C while the temperature for the isothermal tests was 427°C. All fatigue tests were run at 0.02083 Hz (48 seconds per cycle). To date, no published studies have investigated this material using these testing parameters on a quasi-isotropic layup.

II. Summary of Current Knowledge

Many tools are available in evaluating the performance of metal matrix composites and fall into two categories: qualitative and quantitative. This chapter will discuss work that has been accomplished in both areas. First, a summary of the comprehensive studies that have been concluded will be given. Following this, three numerical techniques will be reviewed:

1. METCAN, the METal matrix Composite ANalyzer, along with its fundamental micromechanical equations developed by Hopkins and Chamis.

2. The macromechanical equations developed by Halpin and Tsai used in classical laminated plate theory.

3. The Linear Life Fraction Model developed by Russ et al.

A. Literature Review

Several studies have already been undertaken to characterize the fatigue behavior of SCS6/Ti-15-3, both in the area of thermo-mechanical fatigue (TMF) and isothermo-fatigue (IF). These studies are discussed as follows for reference:

Pollock and Johnson (19:1-11) performed IF tests on cross ply $[0/90]_{2s}$, angle ply $[0_2/\pm45]_s$, quasi-isotropic ply $[0/\pm45/90]_s$, and unidirectional ply $[0]_8$ layups at 650°C and

10 Hz. They conducted fracture surface analysis to determine fatigue damage mechanisms. They drew the following conclusions:

1. The fibers contributed more to the tensile strength and fatigue endurance of the laminate at the elevated temperature than at room temperature. This is because the matrix is weaker at the higher temperature.

2. Initial damage developed in either the fibers or the matrix. High strains and short lives resulted in fiber failure with no matrix fatigue cracking. Low strains and long lives resulted in extensive matrix cracking and no fiber breakage away from the fracture surface.

3. The cyclic life of the laminate was dictated by the stress level in the 0° fibers.

Johnson, Lubowinski, and Highsmith (10:1-11) tested five different layups at room temperature both statically and in fatigue. Off axis layups experienced fiber/matrix interface failures at stress levels lower than the matrix properties. The stress levels in the 0° fibers could be used to correlate the fatigue lives at room temperature of laminates that have 0° fibers. Therefore, the 0° plies play an essential part in governing fatigue life.

Ermer (5:59) tested uniaxial layups for TMF cycling. He discovered that the reaction zones had expanded and that

cracks formed in the matrix and grew outward, radially from the fibers.

Gabb et al. (6:8-10) performed static (at 300°C and 550°C), IF (550°C), and TMF tests on uniaxial plies (0° and 90°). These tests showed a constant modulus of elasticity for the first 2/3 of specimen life but a steady decrease for the final 1/3. They also showed that cracks either started at the surface or at the fiber/matrix interface near the surface. The TMF cycling caused a considerable amount of damage at the reaction zone.

Their research also suggested that the fatigue life probably was not matrix dominated but fiber-matrix interface dominated.

Majumdar and Newaz (13) and (14) conducted IF (650°C) and TMF (315°C - 650°C) tests on quasi-isotropic layups. They adopted microscopic replica techniques to document fatigue damage mechanisms. The authors observed the following:

1. At any particular stress level, TMF was shown to have a shorter life than isothermal. The primary damage modes for the TMF specimens were fiber-matrix debonding and inter-ply delamination in the off-axis plies, but mostly with the 90° plies. However, the TMF specimens also indicated both transverse cracking at the fracture surface (which seemed to originate slightly before or during failure) and longitudi-

nal ply delamination near and away from the fracture site.

2. For specimens that had very short lives (under 100 cycles), the inner 90° fibers near the fracture surface were found to be protruding out the matrix. This indicated significant viscoplastic matrix elongation in the loading direction (causing a transverse contraction due to Poisson effect) and fiber-matrix debonding.

3. Delamination cracking occurred more frequently between closely spaced fibers. This type of cracking indicated that the local fiber density raised the stress/strain magnitude in the reaction zone and matrix between the adjacent fibers.

4. Microprobe analysis showed carbon-rich zones between the titanium plies. The presence of carbon can lead to the formation of titanium carbides which causes local embrittlement of the inter-ply region. As a result, this region can become locally weakened and may accelerate delamination cracking.

5. The authors believe that the failure scenario for TMF cycling of the quasi-isotropic specimens evolves from early damage and loss of stiffness of the 90° plies, followed by load transfer and cracking of the 0° plies.

Castelli et al. (4:12-18) completed IF and TMF tests on uniaxial specimens. They heat treated the specimens for 24

hours at 700°C. The IF testing was at 10 Hz and 427°C and the TMF testing was at 0.33 Hz and 93°C - 538°C. The IF tests showed extensive matrix cracking with fiber damage both near and away from the failure site. The in-phase TMF testing showed extensive fiber cracking with minimal matrix damage. The out-of-phase TMF testing showed extensive matrix damage with minimal fiber cracking. Common to all tests, the failure surfaces were flat due to the fatigue cracking, the fibers experienced pullout, and there was ductile matrix failure. The specimens subjected to higher mechanical stresses showed more fibers pulled out and larger areas of ductile matrix failure.

Schubbe (23:89-91) tested cross ply laminates in TMF cycling from 149°C - 427°C. He showed a general trend in the straining of the specimens over the course of the cycling. During the first 20 cycles, the specimens displayed a strain stabilization. Then, over the next 1,000 cycles, they showed a fairly quick increase in the mean strain (as compared to the entire life span of the specimen). This quick increase can be attributed to creep-rachetting.

The conclusions from the above research can be summarized as follows: The fatigue endurance of the laminate was predicated on the stress levels of the 0° fibers; the matrix cracks either started at the laminate surface or at the fiber/matrix interface; TMF cycling produced a shorter life

than IF cycling; in-phase TMF testing produced extensive fiber cracking with minimal matrix damage while out-of-phase testing produced extensive matrix cracking with minimal fiber damage; and, the failure for the quasi-isotropic MMC started in the 90° plies and progressed to the 0° plies.

However, to gain even further insight as to what induces failure within the MMC, numerical techniques have been formulated to predict this behavior as will be discussed in the next segment.

B. Analytical Techniques

Three numerical techniques were employed in an attempt to estimate the laminate properties and comprehend the fatigue behavior of the SCS6/Ti-15-3 MMC in a quasi-isotropic layup. This section will illustrate these three approaches.

1. METCAN - Metal Matrix Composite Analyzer (17). METCAN is a FORTRAN language computer program developed by NASA Lewis Research Center to analyze (both in a linear mode and nonlinear mode) fiber-reinforced metal matrix composites. It is primarily committed to providing material properties compatible with large structural analysis programs such as MSC/NASTRAN.

The file system for METCAN consists of the primary input file, the primary output report file, the constituent data-

bank file, and 10 postprocessing files. These postprocessing files contain information relating to various behavior/response variables such as time; ply temperature; instantaneous fiber, matrix, or interphase properties; fiber, matrix, or interphase total stresses; incremental ply and composite stresses and strains; and, instantaneous composite properties. All these variable are given at each corresponding load/time step of the loading history.

The program contains unique equations that serve as models of both the composite's constituent materials and general composite mechanics to evaluate the composite's thermal and mechanical characteristics. METCAN then uses the proper ply orientations to estimate the engineering properties of the laminate. Reference 12 presents a comprehensive summation of the unique equations; however, a brief synopsis is given here for reader edification.

Hopkins and Chamis Micromechanics Equations (9). Hopkins and Chamis developed a set of equations from a mechanics of materials formulation assuming a square array unit cell model of a single fiber, surrounding matrix, and an interphase region to explain the chemical reaction which commonly occurs between the fiber and matrix (see Figure 1). They then applied the principles of displacement compatibility, force equilibrium, and Fourier's law for heat conduction.

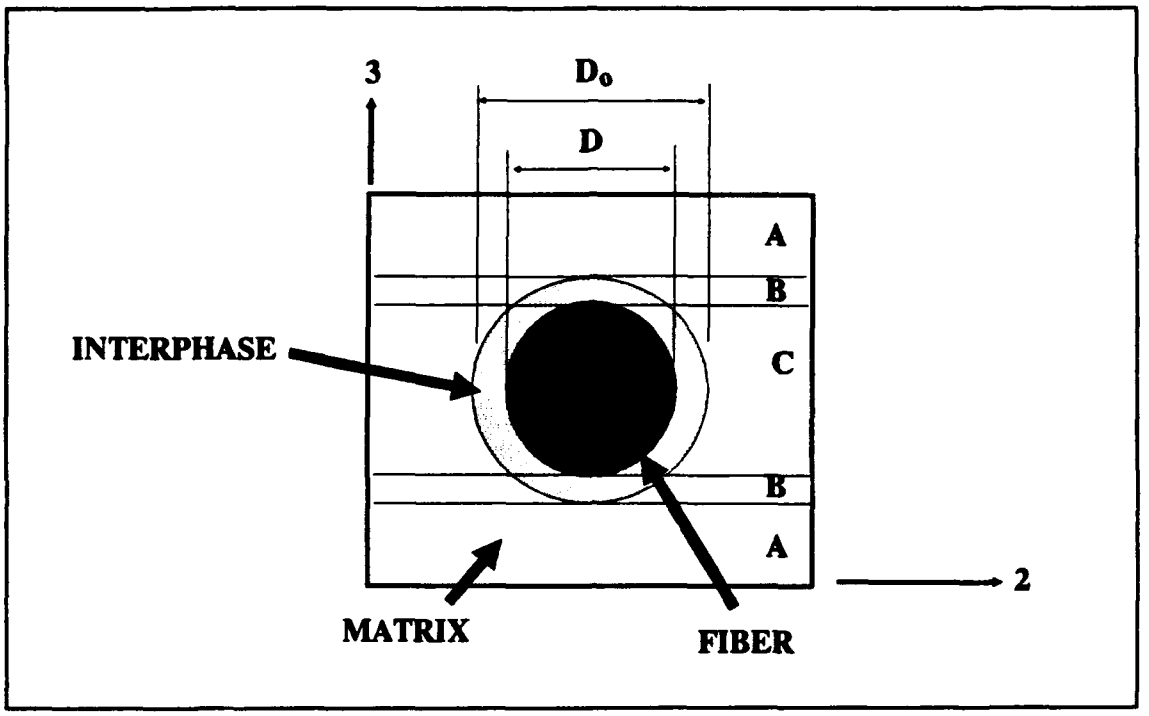

Figure 1. Square Array Unit Cell

In their development, they made the following assumptions:

a. Fibers are continuous and parallel in each ply.

b. Properties of all fibers in the composite are identical.

c. Complete bonding exists between constituents.

d. Constituent material behavior is thermoviscoplastic, anisotropic, and three-dimensional.

e. Interphase growth results from the degradation of fiber material and thus propagates inward causing a continuous decrease of the current fiber diameter from the original fiber diameter.

f. The transverse moduli do not account for the longitudinal Poisson restraining effect that the fiber transmits to the matrix. The restrained matrix effect is negligible for MMC's. (The effect is more significant in the resin matrix composites where the fiber/matrix stiffness ratio is much greater.)

g. Constituent microstresses are based on uniaxial behavior, they do not include any Poisson effects.

The micromechanics equations were then derived for the special case of a transversely isotropic (isotropic in the 2-3 plane) ply allowing for transversely isotropic constitu-

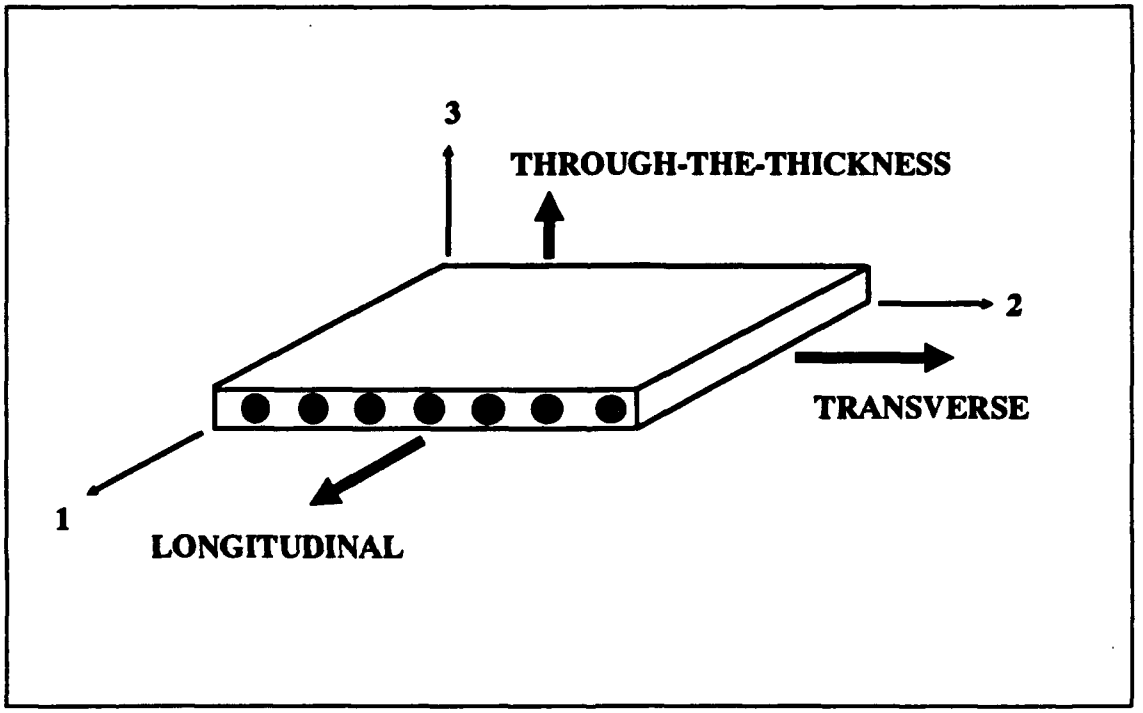

Figure 2. Unidirectional Composite Ply Coordinate System

ents. (See Figure 2.) These equations are comprised of expressions for ply equivalent mechanical properties (moduli, Poisson's ratios, and uniaxial strengths), ply equivalent thermal properties (conductivities, coefficients of expansion, and heat capacity), ply in-plane uniaxial strengths, and thermomechanical microstresses of the ply constituents (fiber, matrix, and interphase).

Referring to the square array unit cell in Figure 1, example equations are as follows where V, f, m, d, and l represent original volume fraction (before interphase growth), fiber, matrix, interphase, and ply quantity, respectively:

Longitudinal Modulus:

$$E_{l11}=V_m E_{m11}+V_f\left[\left[1-\left[\frac{D}{D_o}\right]^2\right]E_{d11}+\left[\frac{D}{D_o}\right]^2 E_{f11}\right] \qquad (1)$$

Longitudinal coefficient of thermal expansion:

$$\alpha_{l11}=V_m\left[\frac{E_{m11}}{E_{l11}}\right]\alpha_{m11}+V_f\left[\left[1-\left[\frac{D}{D_o}\right]^2\right]\left[\frac{E_{d11}}{E_{l11}}\right]\alpha_{d11}+\left[\frac{D}{D_o}\right]^2\left[\frac{E_{f11}}{E_{l11}}\right]\alpha_{f11}\right] \qquad (2)$$

Longitudinal fiber and matrix microstresses:

$$\sigma_{f11}=\left[\frac{\sigma_{l11}}{E_{l11}}+\delta T(\alpha_{l11}-\alpha_{f11})\right]E_{f11} \qquad (3)$$

$$\sigma_{m11}=\left[\frac{\sigma_{111}}{E_{111}} + \delta T(\alpha_{111}-\alpha_{m11})\right]E_{m11} \qquad (4)$$

These equations were then validated through the use of a three-dimensional finite element analysis (FEA). This was accomplished by comparing the equivalent ply properties (E_{111}, E_{122}, G_{112}, G_{123}, ν_{112}, ν_{123}, α_{111}, α_{122}) estimated by the micromechanics equations with the average ply properties simulated in the FEA. Properties for the interphase were taken to be an average of the fiber and matrix properties. Hopkins and Chamis indicated that they achieved excellent agreement.

The authors also discovered that, considering the results of the microstress distribution, it becomes more clear how material failures might occur at a local level and trigger the introduction of a crack. This type of data can give an awareness into the performance and integrity of composites at a micromechanical level which in turn will benefit designers in the area of structural applications.

2. Halpin-Tsai Equations. In reference 7, Halpin and Tsai realized that the elastic properties of composite materials can be divided into micro and macromechanics. Whereas METCAN made great utility of the unique micromechanic equations, the authors developed simpler and more generalized

equations to approximate the results of the more exact micromechanics analysis (1).

They go on to say that the elastic properties of unidirectional composites are influenced by a maximum of four independent macroscopic moduli for orthotropic materials (E_{11}, E_{22}, G_{12}, and G_{23}) and three independent macroscopic moduli for transversely isotropic materials (E_{11}, E_{22}, and G_{12}). Since the material properties can be separated from the geometric properties in a laminated composite according to the invariant theory (24) of composite materials, Halpin and Tsai deduced that they could calculate, through a set of simple formulas, a direct link between the properties of constituent materials and those of laminated composites.

They achieved this link through utilizing: 1) special relationships of the stiffness matrix elements for orthotropic and transversely isotropic materials, 2) plane strain ($\epsilon_3 = 0$), and 3) uniaxial extension ($\epsilon_1 + \epsilon_2 = 0$). The equations that resulted are easily understood and can readily be used in the design process. Also, these equations are quite accurate if the fiber volume fraction does not approach unity (1:76). The equations for the transverse composite modulus are as follows:

$$\frac{E_2}{E_m} = \frac{1+ZETA*n*V_f}{1-n*V_f} \qquad (5)$$

$$n = \frac{(E_f/E_m)-1}{(E_f/E_m)+ZETA} \tag{6}$$

The equations for the in-plane shear modulus are:

$$\frac{G_{12}}{G_m} = \frac{1+ZETA*n*V_f}{1-n*V_f} \tag{7}$$

$$n = \frac{(G_f/G_m)-1}{(G_f/G_m)+ZETA} \tag{8}$$

ZETA is a measure of reinforcement and depends on the fiber geometry, packing geometry, and loading conditions. Values for ZETA are determined by comparing E_2 and G_{12} with exact elasticity solutions through curve fitting techniques (1:76). Halpin and Tsai suggest using ZETA = 1 for the shear modulus and ZETA = 2 for the transverse modulus for fibers with circular cross sections.

Even though these equations compare well with exact elasticity solutions, Agarwal and Broutman (1) advise that they cannot perfectly estimate the composite's moduli. This is due to the variations in the manufacturing processes causing changes in the composite moduli.

To completely calculate all the necessary engineering constants, one needs to make additional use of equations obtained from: 1) the rule of mixtures, 2) a functional rela-

tionship between the elements of the stiffness matrix, and, 3) strength of materials. These equations are:

$$E_1 = E_f V_f + E_m V_m \tag{9}$$

$$\nu_{12} = \nu_f V_f + \nu_m V_m \tag{10}$$

$$\nu_{12} E_2 = \nu_{21} E_1 \tag{11}$$

$$G_f = \frac{E_f}{2(1+\nu_f)} \tag{12}$$

$$G_m = \frac{E_m}{2(1+\nu_m)} \tag{13}$$

3. Linear Life Fraction Model.

In addition to trying to understand the behavior of the laminate's engineering properties during failure, one usually looks for a single parameter that allows data consolidation to determine the laminate's fatigue life. Such parameters may include maximum and minimum fiber axial stresses, the maximum and minimum axial matrix stresses, the fiber axial stress range, the matrix axial stress range, cycles to failure, and applied loading profiles.

Russ et al. (22) attempted to make this characterization with SCS-6/Ti-24-11 but could not. As a result, they de-

veloped a numerical model that uses several parameters, called the Linear Life Fraction Model (LLFM). This model was built on the premise that the composite's failure is due to a linear combination of a fiber dominated failure mode and a matrix dominated failure mode. Their equation is:

$$\frac{N}{N_f} + \frac{N}{N_m} = 1 \tag{14}$$

where N_f and N_m are the cycles to failure due solely to each mode and N is the total cycles to failure. Russ et al. assumed that the fiber dominated failure mode is a function of the fiber maximum stress and the matrix dominated failure mode is a function of the matrix stress range. N_f and N_m can be found from the following equations:

$$N_f = 10^{\{N_o(1 - \sigma_{max}/\sigma^*)\}} \tag{15}$$

$$N_m = B(\delta\sigma_m)^{-n} \tag{16}$$

N_o, B, and n are empirical constants, σ^* is the maximum fiber stress at tension failure under static load at 427°C as calculated from METCAN, σ_{max} is the maximum axial stress in the 0° fibers for a given maximum applied stress level, and $\delta\sigma_m$ is the axial stress range in the matrix for a given

maximum applied stress level.

Mall et al. (15) reported that experimental data from their in-phase and out-of-phase TMF tests correlated well with their predictions using these equations. However, their predictions were not as good with their isothermal experimental results. They claimed that neither the stress range nor the maximum stress in the fiber individually is an optimal parameter for correlation. Rather, they introduced an expression involving both, replacing σ_{max} in the above N_f equation with $\sigma_{max}(1-R)^m$, where m is an empirical constant ranging between 0 and 1 and R is the minimum to maximum applied stress ratio. They were able to achieve good correlation between the test data and this new predictor for all three profiles.

III. Experimental Equipment/Procedures

To properly investigate the fatigue behavior of the SCS6/Ti-15-3 MMC, rectangular specimens were fabricated and tested under load control thermomechanical and isothermal fatigue conditions. This chapter will discuss in detail all phases of the testing and analysis processes accomplished. Included will be the specific fatigue profiles, the material and equipment, the fatigue test components and controls, the strain measurement, the modulus measurement, and the fracture analysis.

A. Testing. A total of 15 tests were conducted:

1. The first was a static test at 427°C to determine the baseline behavior under a monotonically increasing load. This provided the stress and strain levels of first ply failure, the matrix yielding point, and the ultimate strength of the composite.

2. Four tests were conducted under an in-phase (IP) TMF condition. The loading is IP when the maximum temperature of each thermal cycle coincides with the maximum stress of each mechanical load cycle. Different stress levels were selected to characterize the fatigue response of the laminate, and these levels were between the first ply failure stress and the laminate's ultimate tensile strength. To achieve the ideal S-N curve (maximum applied stress vs

cycles to failure curve), the following cycle ranges would normally be targeted: 100 cycles, 1,000 cycles, 10,000 cycles, and 100,000 cycles. However, due to time limitations (because of the low load frequency), 100,000 cycles could not be achieved.

Both the thermal and mechanical load rates were 0.02083 Hz (one cycle every 48 seconds), the temperature ranged from 149°C to 427°C, and the stress ratio (minimum applied stress to maximum applied stress) was 0.1.

3. Five tests were conducted under an out-of-phase (OP) TMF condition. The loading is OP when the maximum temperature of each thermal cycle coincides with the minimum stress of each mechanical load cycle. The applied stress levels, load rate, applied stress ratio, and cycle ranges were the same as the in-phase TMF tests.

4. Five tests were conducted under an isothermal fatigue condition. The temperature was maintained at a constant 427°C while the mechanical load rate, the applied stress levels, the applied stress ratio, and cycle ranges were the same as the TMF tests.

B. Materials and Equipment

1. Material.

An eight ply titanium matrix fiber reinforced composite in a quasi-isotropic $[0/\pm45/90]_s$ laminate form was used for

this research. The exact designation for this material is SCS-6/Ti-15V-3Cr-3Al-3Sn (weight percent), or SCS6/Ti-15-3 for short. The composite was manufactured at Textron, Avco Specialty Metals, by hot isostatically pressing (HIP-ing) alternate layers of continuous silicon carbide fibers (with a diameter of 0.1359 mm) and thin foils of Ti-15-3. Ribbons of titanium were used to hold the fibers in alignment. The "as manufactured" plate provided to AFIT was 330 mm x 330 mm and had an average fiber volume ratio of 0.392. This volume ratio was obtained by the linear method using photomicography of the polished specimen edge. Material properties for the individual fiber and matrix materials are given in Table 1 (18:14,15). Ply and laminate properties are given in Table 2 (11) and (12).

Table 1. Material Properties of the Silicon Carbide Fiber and Ti-15-3 Matrix.

	Fiber	Matrix
Elastic Modulus (GPa):	400.0	91.80 (25°C) 80.44 (316°C) 72.24 (482°C)
CTE (mm/mm/°C):	4.86E-6	8.48E-6 (25°C) 9.16E-6 (316°C) 9.71E-6 (482°C)
Poisson's Ratio:	0.25	0.36

NOTE: Fiber properties are independent of temperature and are assumed to remain elastic (17:7).

Table 2. Engineering Properties for a SCS6/Ti-15-3 Ply and Quasi-Isotropic Laminate.

Ply Properties:	
a. Ambient Conditions:	b. 427°C:
E_1 = 204 GPa	E_1 = 199 GPa
E_2 = 122 GPa	E_2 = 115 GPa
ν_{12} = .315	
ν_{21} = .225	
G_{12} = 42.1 GPa	
Laminate Properties (ambient conditions):	
E_x = 139 GPa	
ν_{xy} = .325	

2. Material Preparation.

Using a diamond tipped circular blade, the specimens were cut from the "as manufactured" composite plate. Each specimen was 12.70 mm wide by 146.1 mm long and had a thickness of 1.692 mm. To avoid stress concentration effects related to exposed fibers, the gage length region did not have a smaller cross section. No problems were created from this setup, since all the failures happened in the gage length.

After the specimens were cut, they were heat treated at 700°C for 24 hours. The heat treatment was accomplished because the matrix of the MMC has a body centered cubic

crystal structure (beta phase) at room temperature; and, when exposed to high temperatures (427°C or higher) for long periods of time (24 hours), the structure will likely change to a hexagonal close-packed crystal (alpha phase). This transformation "age hardens" the matrix causing an increase in the tensile strength of the composite (20:14).

After the heat treatment was accomplished, polishing was performed. Using an automated MAXIMET polishing machine and a holding fixture, one long edge of each specimen was polished with diamond slurry on a #8 platen using 45μ, 15μ, 6μ, and 3μ, and finishing with 1μ. This polished edge was used for replication to monitor the damage initiation and growth during testing. The opposite edge of each specimen was only polished with the 45μ diamond slurry to remove any potential stress risers (burrs, nicks, chips, exposed fibers, etc).

Before testing, each specimen was visually and optically inspected. No specimens appeared to have any original, consequential damage. Detailed non-destructive testing was not accomplished before testing.

3. Fatigue Test Components.

a. Mechanical Load. The tests were performed on an 808 Material Test System (MTS) electroservo tensile test stand as shown in Figure 3. The test stand was configured to deliver up to a 4 kip load. This tester was equipped with

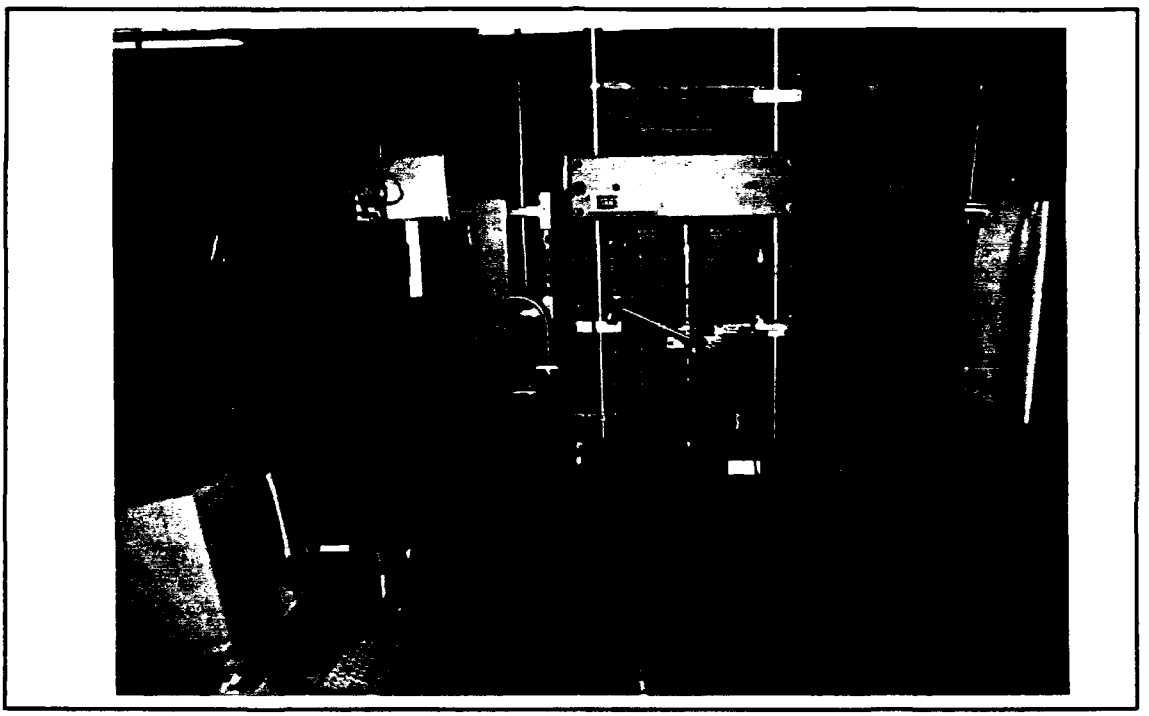

Figure 3. Test Setup

water-cooled wedge grips controlled by an MTS 458.20 Micro-console. A Wavetek Model 75 waveform generator provided a triangular ramping for the load input.

b. Thermal Load. Two quartz lamp heaters (one placed on each side of the specimen as shown in Figure 4) provided radiant heat to the 25.4 mm gage length region of the specimen. These lamps were cooled by a constant flow of water at 12°C. Two sets of chromel-alumel thermocouple wires were welded to each specimen's gage length region (one set in front and the other set in back) to provide feedback for maintaining the proper temperature of the specimens during testing. Copper rods containing small air jets were placed

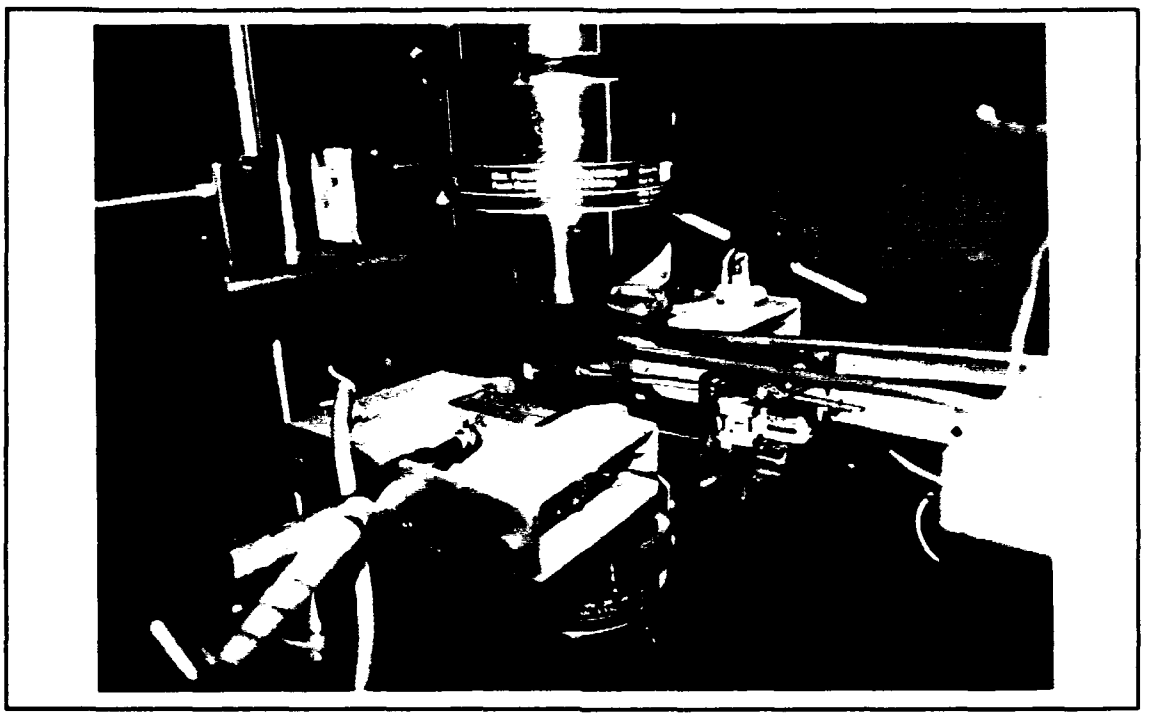

Figure 4. Quartz Lamp Heaters, Copper Rods With Air Jets, and Extensometer

next to the specimens to assist with the cooling phase of each cycle. A pressure setting of 210 MPa delivered the best air flow for the required temperature profiles.

The heaters were regulated by a Micricon 823 Process Controller. This Micricon uses three-mode PID control: Proportional (gain), Integral (reset), and Derivative (rate) (23:35-37).

1) The gain indicates how the output from the controller will change with respect to a variation in the error signal. A gain setting of 35 was used in this study.

2) The reset corrects the steady state error (offset)

by increasing or decreasing the output to modify the "droop" in the waveform caused by the gain. A reset setting of 25 repeats per minute was used in this study.

3) The rate regulates the time lag in the system. Because the fatigue testing software (discussed later) adjusted for any phase lags, a rate setting of 0.0 was used in this study.

A safety fixture was incorporated onto the test stand for allowing observers to watch the thermal and mechanical cycling without threat of injury to the eyes. This protection was provided by a heavily tinted plexiglass shield that could be swung out of the way when the test was on hold or stopped.

To reduce filament wear, the lamp heaters were set to a "lo-limit" value of 3% output rather than have them turn completely off after each thermal cycle.

4. Computer Control. A Zenith 248 personal computer, as seen in Figure 3, was used in conjunction with MATE263, a software package for TMF testing, and MTEST, an isothermal computer program for IF testing. These two programs allowed the computer to control all the major testing components and collect all required data. An adjacent dot matrix printer provided all necessary hardcopy.

MATE263 is a computer control program designed by Mr. George Hartman at the University of Dayton Research Insti-

tute and specifically used for thermo-mechanical fatigue testing. Parameters which had to be inputted included specimen geometry, material characteristics, temperature versus mechanical load profile (in-phase or out-of-phase), maximum and minimum temperatures, applied load ratio (minimum to maximum), maximum stress, and the extensometer calibration factor. These inputs allowed the program to specifically adapt the hardware to the required testing requirements.

Besides controlling the hardware, the MATE263 software package concurrently monitored the temperatures (from the thermocouples), the load, the displacement (from the extensometer), the cycle count, and the phase angle between the thermal cycling and the mechanical cycling. During each Data Acquisition Cycle, the program adjusted the mechanical load, temperatures, and phase angle as necessary.

MTEST, the isothermal fatigue testing program, was developed by Capt Brian Sanders, an AFIT PhD student. His program was very similar in nature to MATE263 except that it maintained constant heater lamp output resulting in an isothermal environment. This required an additional set of thermocouple wires.

5. Strain Measurement. The MTS 632.41B-01 extensometer, as seen in Figure 4 below the two copper rods, with a 2.54

cm (one inch) gage length was used to measure material displacements. This extensometer was fitted with two quartz rods that had conical tips on either end, were 9.53 cm long, and had a diameter of 4.75 mm. The extensometer arrangement was used versus the more standard strain gages because of the elevated temperature - the strain gages are not capable of withstanding elevated temperatures while the extensometer and quartz rods can.

To prevent slippage, the rod tips were pressed against the specimen edge with enough pressure to cause a high degree of friction between the rods and the specimen during testing. To prevent the extensometer from overheating, the rods were relatively long (keeping the extensometer body away from the direct lamp heating) and air was passed around the extensometer body.

The MTS 650.03 calibrator was used to calibrate the extensometer. Whenever new rods were installed onto the extensometer, the extensometer was mounted to the calibrator and zeroed at 2.54 cm using a telemicroscope. The calibration was then accomplished using the calibration subroutine of MATE263. The ensuing calibration factor was used by the two fatigue computer programs during testing to provide accurate strain readings.

6. Modulus Measurement. Before each fatigue test was initiated, two modulus tests were conducted - one at room

temperature and one at elevated temperature (427°C). Using the Modulus program, also written by Capt Sanders, a load was applied and increased to a predetermined maximum value then reduced to zero. To ensure that first ply failure was not reached, this maximum load was 50% of the value where first ply failure occurred (as determined by the static test). To verify first ply failure was not attained, the stress-strain plot generated by Modulus was examined for linearity.

To determine the modulus at 427°C, the Micricon was programmed to deliver constant heat. After the specimen was thoroughly heat soaked for at least 5 minutes at temperature, the elevated temperature modulus test was conducted.

C. Fracture Analysis. Damage mechanisms were investigated both before failure and after failure.

1. Before failure, the method of replicas was incorporated before and during the testing phase to obtain a pictorial history of damage at the edge as it occurred. Before testing had begun, replication was performed to document that no damage was present. During the testing phase, the tests were temporarily interrupted when the maximum strain levels had increased significantly since the last replication.

To produce the optimum replicas, the currently used fatigue program was put on hold, the heat lamps were swung

away (to allow the specimen to cool down to room temperature), the SPAN was reduced to zero, a preload equal to 50% of the maximum load was applied (to open existing cracks and make them more visible), and the air was turned off (to prevent premature evaporation of the acetone). The extensometer was not disturbed. A strip of acetate film (1.5 cm x 2.5 cm) was pressed against a cotton swab wetted with acetone and the gage length region of the polished specimen edge (as seen in Figure 5a). The swab was removed and the acetate strip was pressed again against the specimen edge. After 45 seconds, the acetate was peeled away from the edge and an impression was left on the film. Several replicas were taken during each interruption to ensure a clean edge impression was acquired.

An optical microscope (with camera) capable of providing 50X, 100X , 400X, and 1000X magnification was used to investigate the cracks found on the replicas. The following damage information was documented: the direction of the matrix cracks (either transverse or longitudinal to the loading), which fibers (0°, 45°, or 90°) the matrix cracks were emanating from, the general length of the cracks, the number of cracks, which fibers were cracked, and when the damage occurred (cycle count). For optimal photographic quality, a green light filter was used to improve contrast.

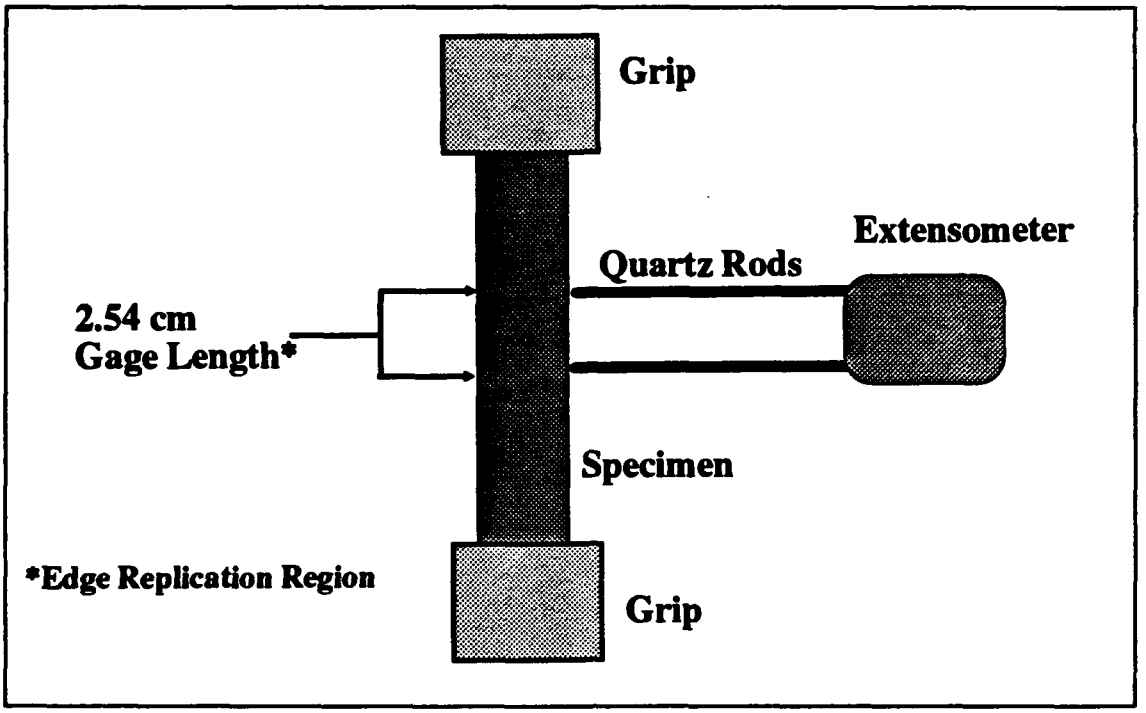

Figure 5a. Edge Replication in Specimen's Gage Length

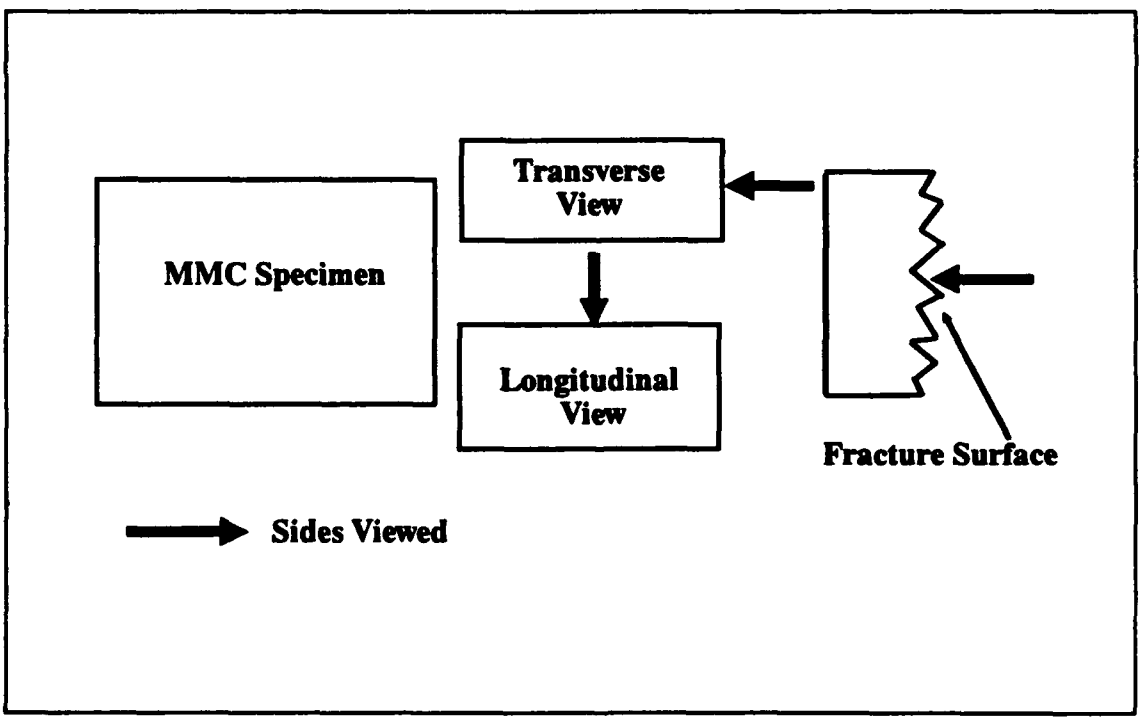

Figure 5b. Specimen Sectioning Outline

2. After failure, both metallography and fractography were employed near and away from the fracture site. After each specimen failed, it was segmented as indicated in Figure 5b using a diamond sectioning wheel. The fracture surface was mounted onto a slotted holder and required no further preparation.

The sectioned pieces (showing longitudinal and transverse edges) were mounted in a thermoplastic mounting compound and were subsequently polished. The surfaces were first polished on an automated MAXIMET polishing machine using a #8 platen and the following diamond slurry suspension sequence: 45μ, 9μ, 3μ, and 1μ. The specimens were then polished on the automated VIBROMETS, 1μ for 8 to 16 hours and 0.5μ for 8 to 16 hours. This produced a highly polished, almost mirrorlike surface suitable for metallographic analysis.

After all pieces of each specimen were properly mounted and polished as necessary, a scanning electron microscope was used to determine the types of failure - fiber pullout, ductile matrix, matrix cracking away from the failure site, and fiber cracking away from the failure site. These failure mechanisms were then correlated to the various stress/strain levels and loading conditions.

IV. Experimental Test Results and Discussion

The objective of this thesis is to characterize the behavior of the SCS_6/Ti-15-3 metal matrix composite of quasi-isotropic lay-up, $[0/\pm45/90]_S$, in a thermal/mechanical and isothermal/mechanical fatigue environment. This chapter will discuss the experimental results of the testing performed in the following manner:

A) test results summary including:

1) discussion of the static test performed,

2) selection of the test matrix,

3) summary of the initial modulus tests (performed on each specimen prior to any fatigue testing), and

4) table and graphs of the cycles to failure for all test conditions;

B) strain measurements;

C) the instantaneous Young's modulus; and,

D) the fracture analysis.

Note: The results of a numerical analysis using the Tsai-Halpin equations, classical laminated plate theory, METCAN, and the Linear Fracture Life Model are presented in Chapter V. A comparison between experimental results and numerical results are made in that chapter.

A. Test Results Summary

Fifteen tests were completed on the $[0/\pm45/90]_s$ SCS_6/Ti-15-3 composite: one was an elevated temperature static ultimate tension test, four were thermo-mechanical fatigue (TMF) in-phase (IP) tests, five were TMF out-of-phase (OP) tests, and five were isothermal mechanical fatigue (IF) tests. The TMF tests were conducted between 149°C and 427°C while the static tension test and the IF tests were conducted at a constant 427°C. All mechanical fatigue loads were applied with a triangular wave form at a load ratio (minimum applied load to maximum applied load) of 0.1 and a frequency of 0.02083 Hz (one complete cycle every 48 seconds).

1. Static Test.

The first step in conducting fatigue tests is to establish the stress levels for the fatigue profiles. The stress levels chosen for this investigation were based on where the two points of nonlinearity exist on the ultimate static test's elevated temperature stress-strain curve. This test was conducted at the maximum temperature of the TMF and IF tests (427°C). The first point of nonlinearity corresponds to the first ply failure and is associated with the fiber/matrix debonding in the 90° plies and possibly the 45° plies. The second point of non-linearity corresponds to the matrix yielding point (matrix plasticity). The results of

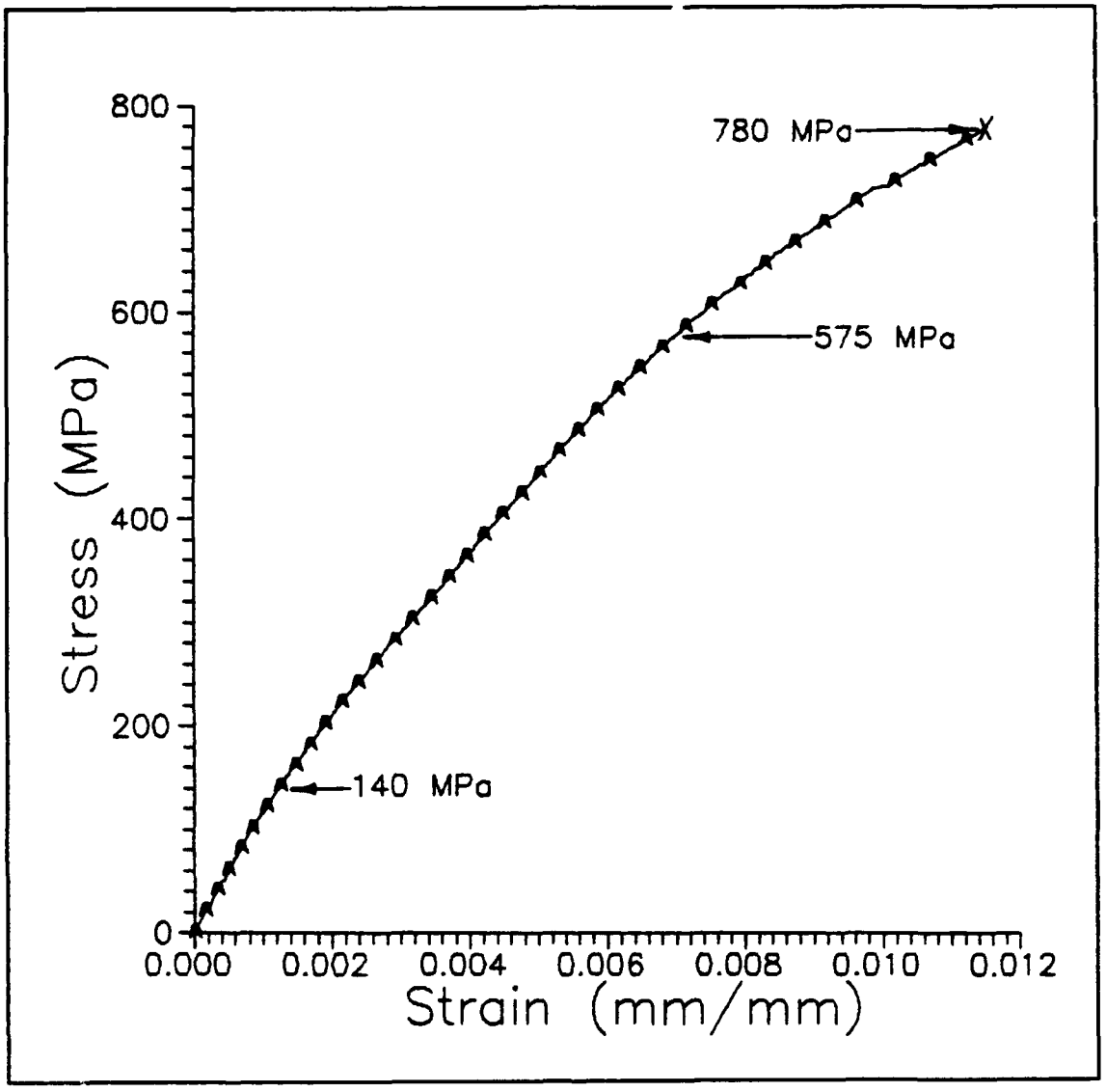

Figure 6. Static Ultimate Stress-Strain Curve at 427°C

the test are shown in Figure 6. First ply failure occurred at 140 MPa while matrix yielding occurred at 575 MPa. Thus, these two points served as the outer boundaries for the fatigue test applied stress spectrum. Once the second point of non-linearity was achieved, the load was increased until

specimen failure at 780 MPa.

2. Fatigue Test Matrix.

Ideal S-N curves (Stress vs Number of cycles to failure) have data points in the 100 cycle range, the 1,000 cycle range, the 10,000 cycle range, and the 100,000 cycle range. Due to the relatively slow cycle frequency used (0.02 Hz) and the limited time allowed for this investigation, the 100,000 cycle range was not attained. (Note: 10,000 cycles is approximately 1 week of testing time.) The maximum applied stress level used for testing was chosen to be 475 MPa (100 MPa below matrix yielding). The other stress levels were determined by the results at this initial stress level. Refer to Table 3 for a summary of the fatigue test matrix.

Table 3. Fatigue Test Matrix Summary

Maximum Applied Stress (MPa)	TMF (IP)	TMF (OP)	IF
475	X	X	X
450			X
425		X	X
400			X
375	X	X	X
360	X		
325	X	X	
310		X	

NOTE: IP is in-phase, OP is out-of-phase, IF is isothermal

3. Modulus Measurements Prior to Testing.

Prior to the static ultimate test and each fatigue test, the Young's Modulus was measured on each specimen both at ambient temperature and at the maximum testing temperature (427°C) using the Modulus program described in Chapter III. See Table 4 for a summary of the measurements. The average ambient modulus was 140.5 GPa and the average modulus at 427°C was 125.2 GPa, which is an 11% drop from its counterpart at ambient conditions. Pollock and Johnson attributed this amount of decline to a function of the percentage of

Table 4. Modulus Measurements Prior to Testing

Test:	Ambient Modulus: (GPa)	427°C Modulus: (GPa)
In-Phase:		
475 MPa	150.7	131.6
375 MPa	138.1	121.5
360 MPa	142.1	125.8
325 MPa	133.6	120.2
Out-of-Phase:		
475 MPa	139.5	122.9
425 MPa	138.7	122.9
375 MPa	137.9	124.0
325 MPa	133.6	119.4
310 MPa	146.6	131.1
Isothermal:		
475 MPa	148.2	136.1
450 MPa	133.6	120.8
425 MPa	137.3	122.7
400 MPa	148.5	130.5
375 MPa	148.1	132.1
Static Ultimate:	130.9	116.5
Average:	140.5	125.2

fibers parallel to the loading direction (0° plies) and the percentage of fibers in the remaining off-axis plies (19:6). The data from the modulus tests performed on the static specimen are plotted in Figure 7.

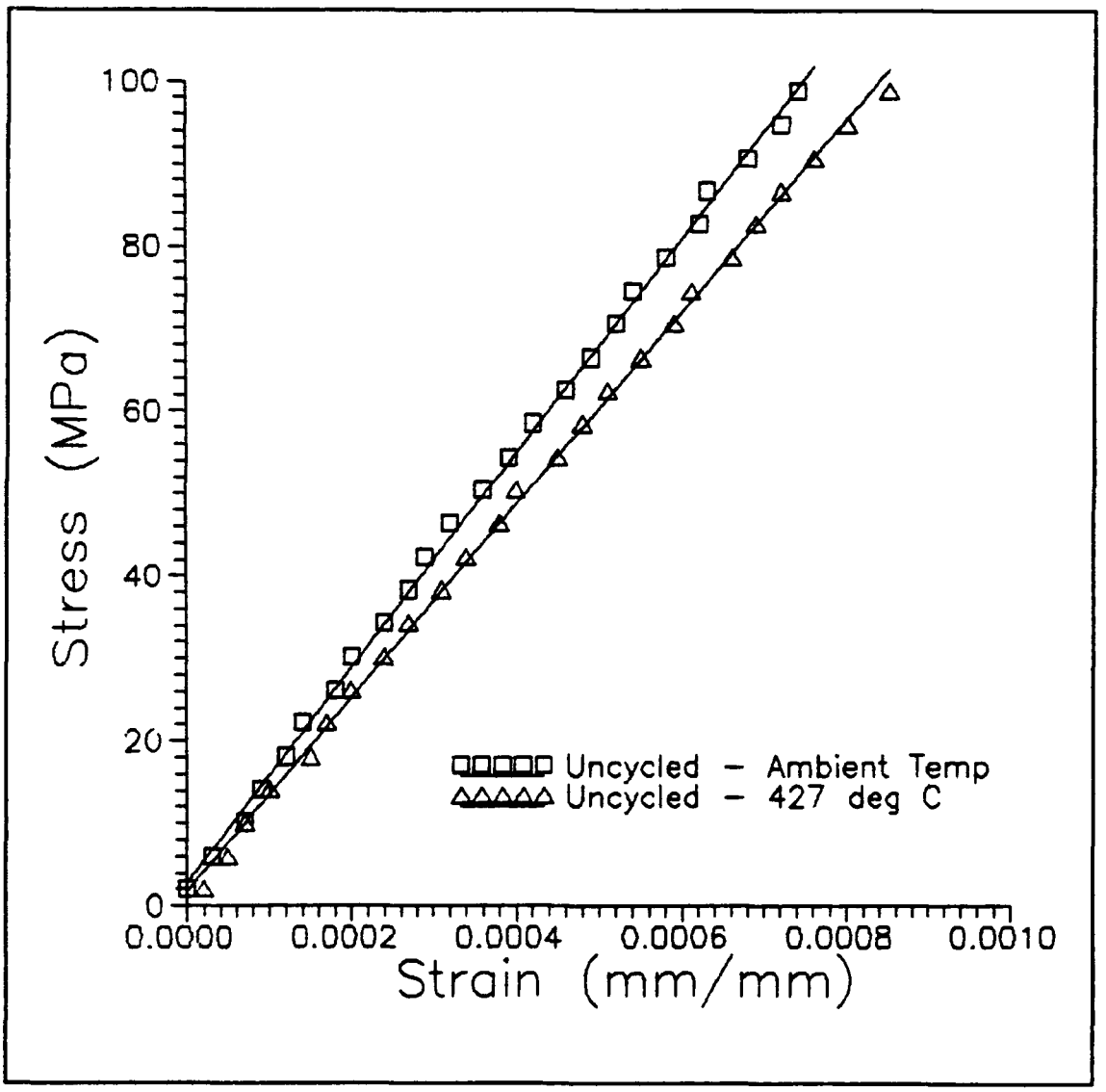

Figure 7. Modulus Data - Static Tests

4. Fatigue Life Results.

The TMF and IF results are summarized in Table 5. Also, they are plotted as maximum applied stress versus number of cycles to failure on a normal axis, in Figure 8, and maximum applied stress versus number of cycles to failure on a logarithmic axis, in Figure 9.

In comparing the composite's life with respect to the three different cycling schemes, it is interesting to note the "cross over" location, or, where the relative life of the composite reverses.

a. The cross over between in-phase cycling and out-of-phase cycling occurred at 340 MPa and 8,000 cycles. At a

Table 5. Fatigue Life Results

Test:	# Cycles to Failure (N):
In-Phase:	
475 MPa	590
375 MPa	899
360 MPa	1,572
325 MPa	24,121
Out-of-Phase:	
475 MPa	567
425 MPa	3,159
375 MPa	5,425
325 MPa	9,192
310 MPa	15,480
Isothermal:	
475 MPa	381
450 MPa	543
425 MPa	655
400 MPa	1,274
375 MPa	8,124

lower maximum stress level, in-phase cycling will produce a longer life than out-of-phase cycling. Conversely, above the cross-over point, out-of-phase cycling will produce a longer life than in-phase cycling.

Mall et al. (15:5) attributed this behavior to the con-

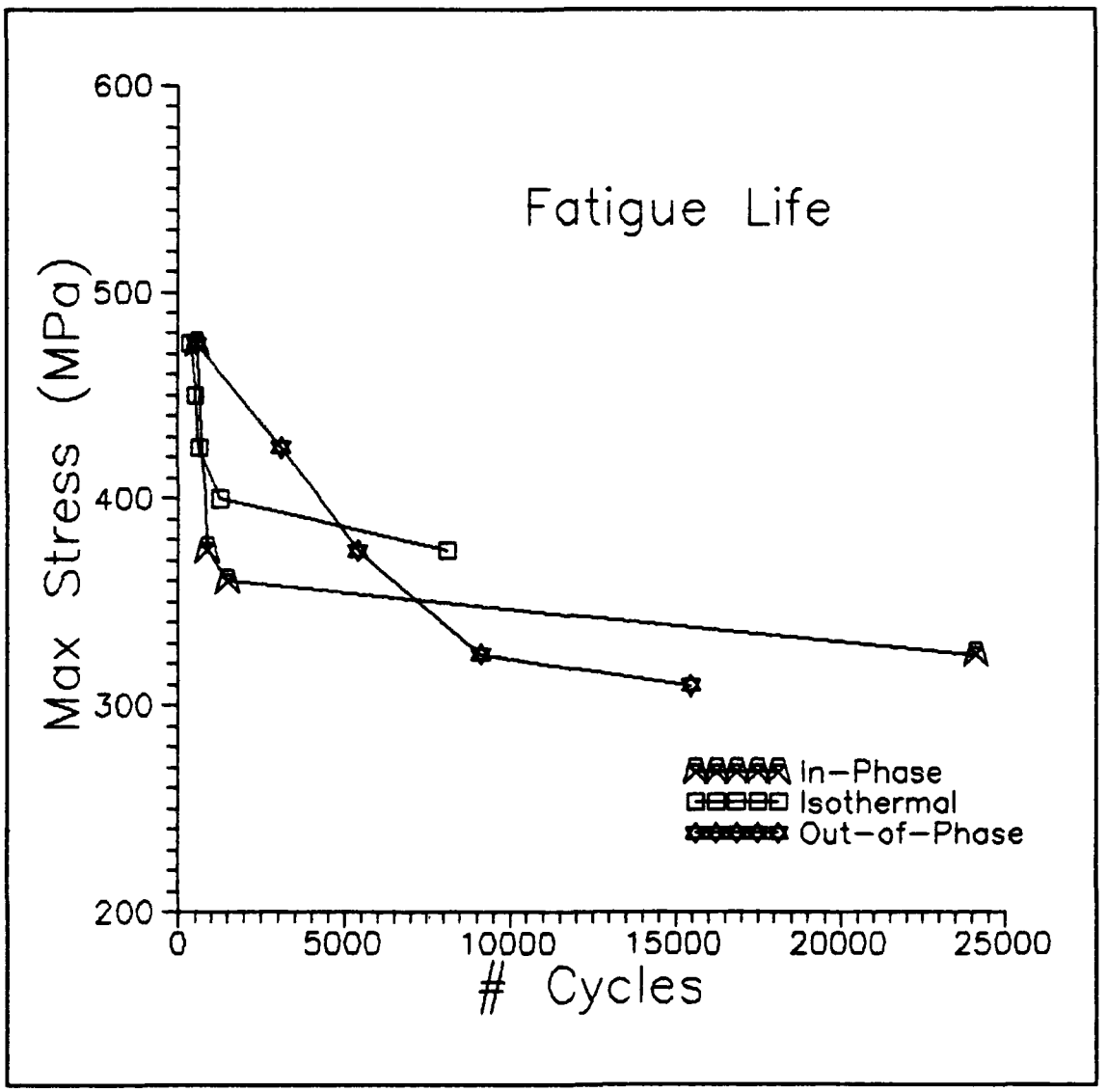

Figure 8. Fatigue Life, normally scaled axis

siderable mismatch in the coefficient of thermal expansion between the silicon carbide fiber and the titanium matrix and to the resulting micromechanical stresses in the fiber and matrix. This mismatch causes the fiber to experience stresses higher in range and in maximum value under IP

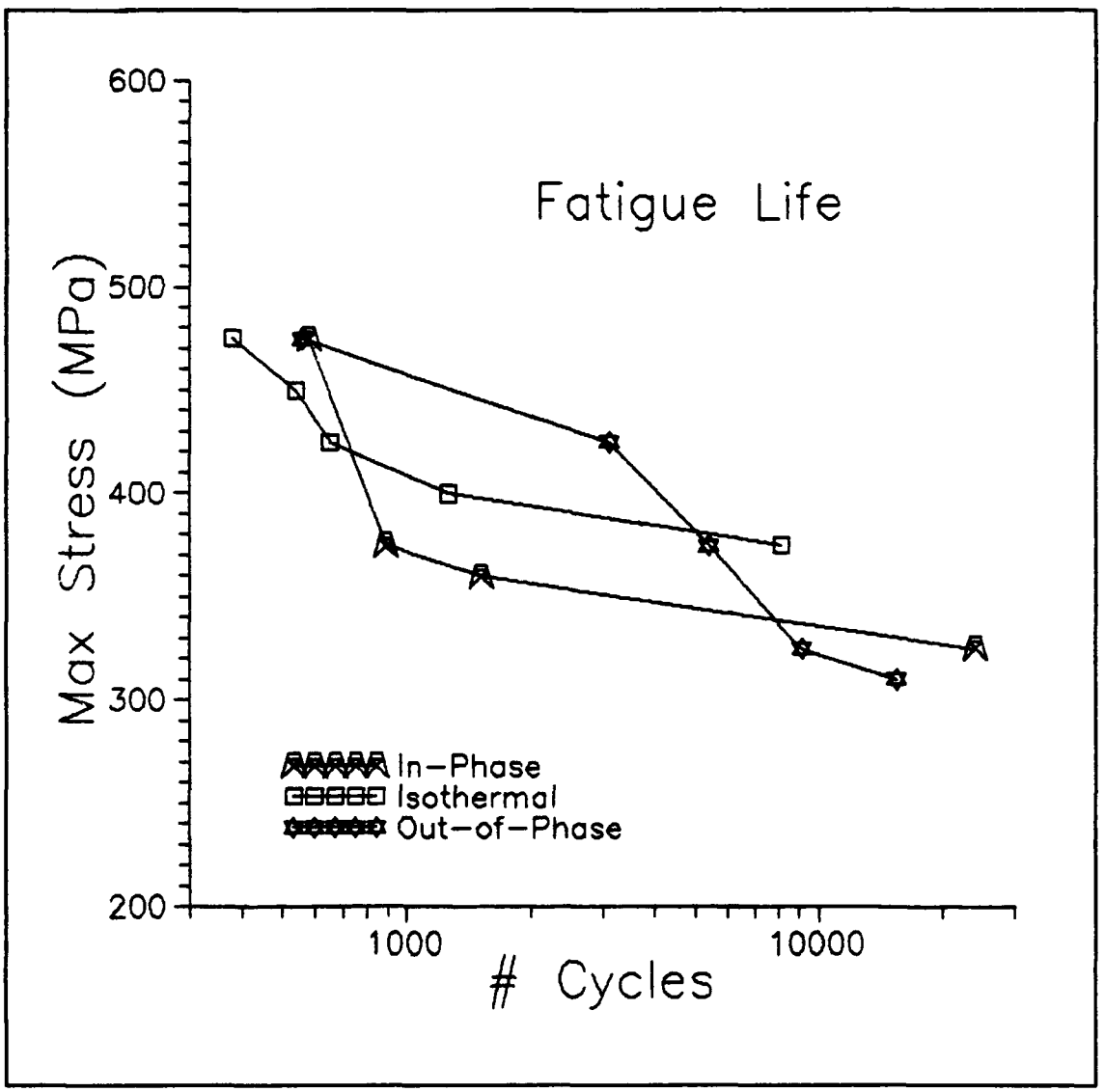

Figure 9. Fatigue Life, logarithmically scaled axis

cycling when compared to OP cycling. On the other hand, cycling increases the stresses both in range and maximum value in the matrix when compared to IP cycling.

Mall et al. (16:8) suggested and observed the IP/OP fatigue curve crossover point occurs at the second point of nonlinearity in the ultimate static test's stress-strain plot. However, in this study, no correlation was seen.

b. Between out-of-phase and isothermal cycling, the cross over occurred at 385 MPa and 5,000 cycles. At a lower maximum stress level, isothermal cycling will produce a longer life than out-of-phase cycling.

c. Between in-phase and isothermal cycling, the cross over occurred at 420 MPa and 750 cycles. Below 420 MPa, isothermal cycling will produce a longer life than in-phase cycling.

Thus, at higher maximum stress levels, out-of-phase cycling produces the longer composite life. At lower maximum stress levels, isothermal cycling produces the longer composite life followed by in-phase cycling. Therefore, one can deduce that the fatigue life of SCS6/Ti-15-3 depends on the test condition as well as the applied stress level. This same conclusion was drawn by Mall et al. in their investigation of a cross-ply SCS-6/Ti-15-3 MMC (16:8).

B. Strain Measurements

Stress-strain behavior and the maximum and minimum strains were recorded repeatedly throughout each test. These strains, measured by the high temperature extensometer, were total strains which are comprised of two components, mechanical and thermal. Since only the mechanical component is exhibited in all the figures of this study, the thermal component had to be derived and subtracted from the total strain readings.

1. Thermal Strain and Coefficient of Thermal Expansion.

The total strain data was reduced as follows (assuming a linear sum relationship between the total strain and the thermal and mechanical strains) :

$$\epsilon_T = \epsilon_m + \epsilon_t \tag{17}$$

or:

$$\epsilon_m = \epsilon_T - \epsilon_t \tag{18}$$

where "T" is total, "m" is mechanical, and "t" is thermal.

Before every fatigue test was initiated, the specimen's gage length was brought to a temperature of 427°C under a no load condition. Using room temperature (20°C) as the point where no thermal strain existed (and where the extensometer

output was zeroed), the average value for the thermal strain at 427°C was:

$$\epsilon_t \text{ (427°C)} = 0.00260 \text{ mm/mm} \qquad (19)$$

The thermal strain can also be derived through the following relationship:

$$\epsilon_t = \alpha * \delta\text{Temp} \qquad (20)$$

where α is the coefficient of thermal expansion and "δTemp" is the change in temperature in °C (from room temperature).

The average thermal strain at 427°C as determined above corresponds to a coefficient of thermal expansion of:

$$\alpha = 6.39 \times 10^{-6} \text{ mm/mm/°C} \qquad (21)$$

Using α, the thermal strain at the lower temperature of the TMF profile (149°C) is calculated to be:

$$\epsilon_t \text{ (149°C)} = 0.000824 \text{ mm/mm} \qquad (22)$$

2. Mechanical Strains.

a. Method of Calculation:

The mechanical strains for the in-phase cycling were handled as follows: the maximum mechanical strain is the maximum thermal strain subtracted from the maximum total strain; the minimum mechanical strain is the minimum thermal

strain subtracted from the minimum total strain.

The mechanical strains for the out-of-phase cycling were handled as follows: the maximum mechanical strain is the minimum thermal strain subtracted from the maximum total strain; the minimum mechanical strain is the maximum thermal strain subtracted from the minimum total strain. This was due to the out-of-phase profile: the maximum temperature occurs at the minimum mechanical load and the minimum temperature occurs at the maximum mechanical load.

For the isothermal cycling, the maximum thermal strain was subtracted from both the maximum and minimum total strains to obtain the maximum and minimum mechanical strains, respectively.

b. Strain Response:

The resulting maximum and minimum mechanical strains from the fatigue cycling discloses significant details about the composite's behavior and damage mechanisms. Figures 10, 11, and 12 exhibit typical strain responses of IP, OP, and isothermal cycling, respectively. (See Appendix D for plots of the other tests.) For example, the maximum and minimum strain rates as well as the difference between the two give an indication of how the composite's stiffness is being affected by the fatigue cycling.

According to Mall et al. (15), if the strain curves

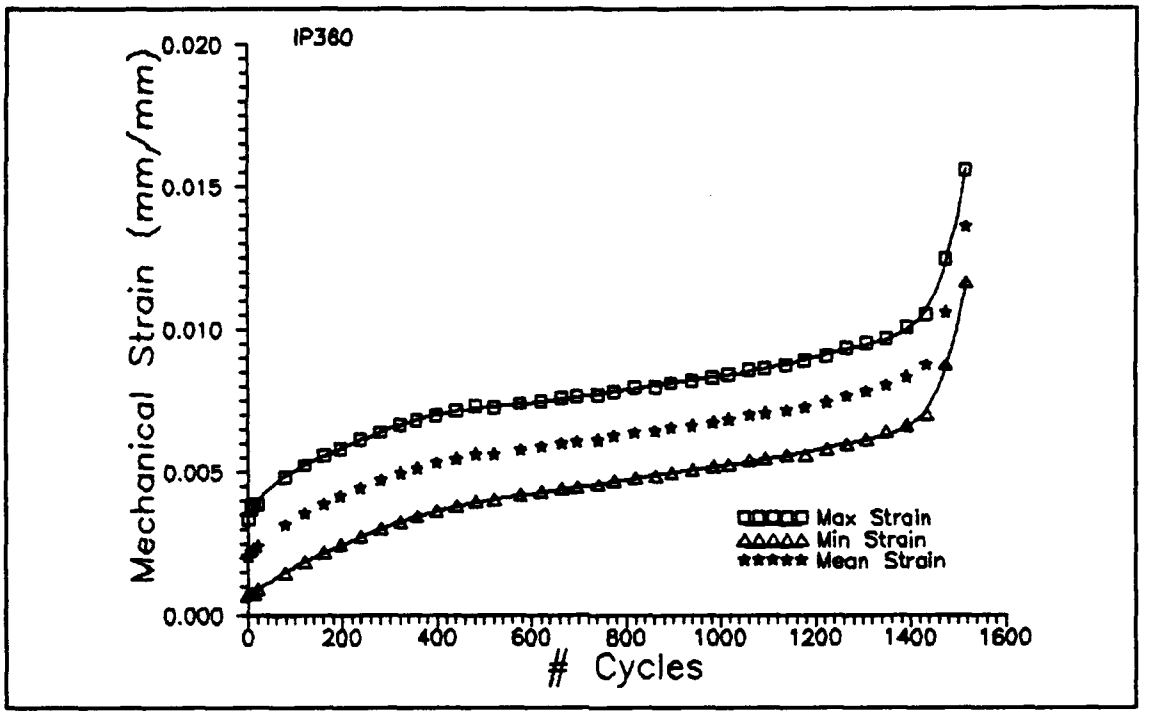

Figure 10. Mechanical Strain Data for 360 MPa IP Test

separate as the fatigue life of the composite progresses, as the OP strain figure shows, damage is accumulating from either fiber breakage, matrix cracking, or both. If the strain curves increase at the same rate, as both the IP and IF figures indicate, permanent damage is not developing. Rather, this increase is due to accumulated creep strains (creep ratchetting) in the matrix material, assuming fibers do not creep at these elevated temperatures (149°C to 427°C).

At all stress levels in the IP TMF cycling, an initial creep stage exists where creep in the matrix redistributes the applied stresses to the fibers. Next, strain accumu-

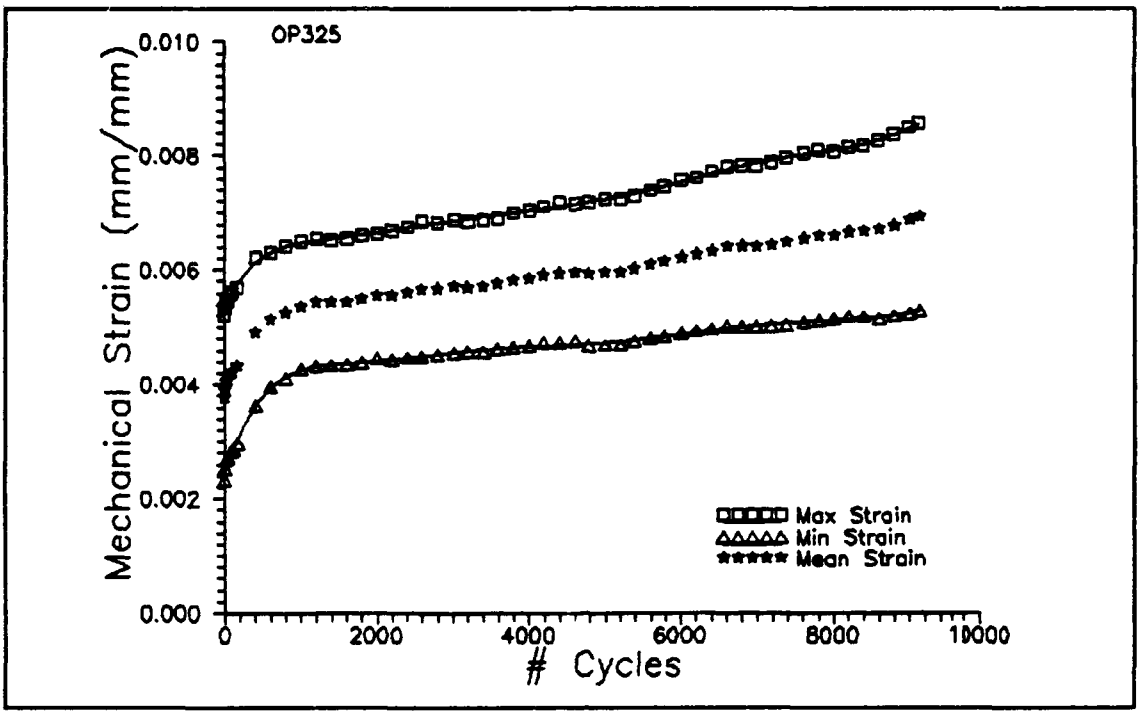

Figure 11. Mechanical Strain Data for 325 MPa OP Test

lates gradually due to the creep ratchetting just mentioned. This creep ratchetting can most likely be attributed to the matrix experiencing its maximum load at the same time the maximum temperature is applied. As the strain levels continued to rise, more and more of the load was transferred to the 0° fibers until the critical fiber stress was reached. Since the stiffness does not appear to be changing during this process, the fiber breakage is probably small. Just before failure, fiber failure initiated and accumulated ultimately inducing specimen failure.

As can be seen in the higher load IP strain plots, the load was transferred to the fibers until their failure

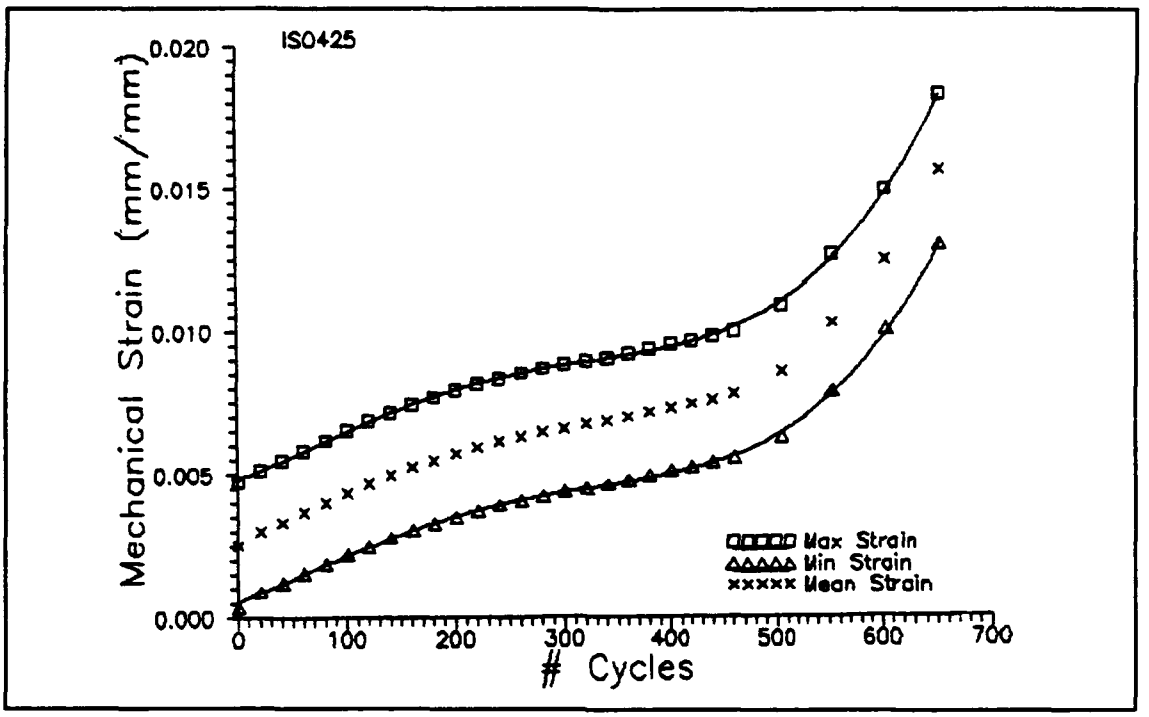

Figure 12. Mechanical Strain Data for 425 MPa IF Test

caused ultimate failure in the specimen. The load was sufficiently high enough to not allow enough time for any matrix fatigue cracking to occur and is evident by the very short rise in strain at the end of the specimens' lives. This will be reinforced through the fractographic results where it will be shown that ductility in the matrix of the 0° plies indicate a static versus fatigue type matrix failure.

Conversely, as shown in the lower load IP strain plots, when the maximum mechanical strains grew beyond approximately 0.009 mm/mm and most of the fiber failure had occurred, the load was transferred back to the matrix. However, the

maximum applied load was not strong enough to immediately induce static matrix failure. This, then, allowed time for matrix cracking which eventually led to ultimate failure. The matrix cracking is denoted by the dramatic increase in the strain rates near the end of the specimens' lives. As the fractographic results will show, more matrix cracking was evident in the 0° plies of the low load IP tests than the higher load tests further supporting this type of behavior.

Strain accumulation results for the isothermal cycling appear to indicate a similar pattern of creep ratchetting during the majority of specimen life as the IP strain results implied. However, two differences were noted. First, IF cycling only appeared to show initial matrix creep below the IP/IF crossover point versus the matrix creep appearance for all stress levels of IP cycling.

Secondly, the dramatic increase in strain rate at the end of specimen life occurred in the IF cycling above the IP/IF crossover stress of 420 MPa (where the IF life is shorter than the IP life) and in the IP cycling below the crossover point (where the IP life is shorter than the IF life). Again, this large strain increase appeared in the IF cycling when the maximum mechanical strains grew above approximately 0.009 mm/mm. These significant strain rates

may suggest that the fiber breakage occurs earlier in the life span of the higher stress IF and lower stress IP specimens due to a more severe localized fiber loading.

The creep ratchetting, present in the IP and IF strain responses, was not evident in the OP tests. As explained above, this can be attributed to the matrix experiencing its maximum applied load during maximum temperature (427°C) in IP and IF testing. On the other hand, the matrix saw the maximum load during minimum temperature (149°C) in OP testing. The OP strain histories show that there was a steady increase in the maximum strain while the minimum strain's progression rate was either flat or more gradual than the maximum component. The resulting "widening" of the minimum and maximum strain curves indicates a reduction in the longitudinal stiffness, most likely due to matrix cracking. This stiffness reduction is especially evident in the lower applied stress level specimens versus the higher stress specimens. One would expect to see more matrix cracking from these lower load specimens than the higher load specimens. This was later confirmed through the fractographic analysis.

Also, a dramatic strain increase near the end of each specimens' life was not seen. During this last stage of specimen life, the matrix had cracked almost completely. The load then transferred to the fibers resulting in rapid

failure. Thus, one would expect to see more matrix cracking in the OP specimens overall than the IP and IF specimens. Again, this was later confirmed from observations of the fractured specimens.

3. Failure Strain Summary.

Table 6 presents a summary of the maximum total failure strains for the fatigue tests. Table 7 presents a summary of the maximum mechanical failure strains for the fatigue tests. Due to the large slopes in some strain data, near

Table 6. Failure Strain Summary - Total Strain

Test:	Maximum Strain at Failure (mm/mm):
In-Phase:	
475 MPa	0.01076
375 MPa	0.00951
360 MPa	0.01570
325 MPa	0.01500
	Average = 0.01274
Out-of-Phase:	
475 MPa	0.00782
425 MPa	0.00791
375 MPa	0.00981
325 MPa	0.00930
310 MPa	0.00662
	Average = 0.00829
Isothermal:	
475 MPa	0.01812
450 MPa	0.02297
425 MPa	0.01960
400 MPa	0.01198
375 MPa	0.01090
	Average = 0.01671

and at failure, the failure strain is taken at 98% of the maximum fatigue life.

The failure maximum total strain for the IF tests averaged at 1.7% and the IP tests averaged at 1.3% while the OP tests averaged at 0.83%. On the average, this indicates that isothermal cycling is most susceptible to a ductile, or static, type of matrix failure, followed by IP cycling. Conversely, the out-of-phase cycling is most susceptible to a brittle, or fatigue, type of matrix failure. This same conclusion was drawn in the previous strain response sec-

Table 7. Failure Strain Summary - Mechanical Strain

Test:	Maximum Strain at Failure (mm/mm):
In-Phase:	
475 MPa	0.00816
375 MPa	0.00691
360 MPa	0.01310
325 MPa	0.01240
	Average = 0.01014
Out-of-Phase:	
475 MPa	0.00699
425 MPa	0.00708
375 MPa	0.00898
325 MPa	0.00848
310 MPa	0.00580
	Average = 0.00747
Isothermal:	
475 MPa	0.01552
450 MPa	0.02037
425 MPa	0.01700
400 MPa	0.00938
375 MPa	0.00830
	Average = 0.01411

tion as well as in the failure strain summary for Schubbe's (23:65-66) investigation of a cross ply layup SCS6/Ti-15-3 MMC under similar IP and OP fatigue loading conditions.

The failure maximum mechanical strain for the IF tests averaged at 1.4% and the IP tests averaged at 1.0% while the OP tests averaged at 0.75%. The 0.3% drop in the average failure strain for the IF and IP tests versus the 0.1% drop for OP tests implies that the thermal loading during maximum mechanical load contributed more significantly to failure during the in-phase and isothermal testing than out-of-phase testing. This same trend was again noticed in Schubbe's work (when comparing IP and OP cycling, 23:66-67).

C. Instantaneous Young's Modulus

Besides using the difference between the maximum and minimum strains as a measure of stiffness, the modulus was determined throughout the life of each specimen.

1. Method of Calculations:

The instantaneous longitudinal stiffness modulus was computed by calculating the change in the applied stress for each Data Acquisition Cycle (DAC) and dividing it by the change in mechanical strain for each DAC as follows:

$$E = \frac{\delta(\sigma_{applied})}{\delta(\epsilon_{mechanical})} \tag{23}$$

This method, in effect, assumes a linear relationship of stress and strain. The assumption is only legitimate if the actual applied stress to mechanical strain curve is linear itself. As can be seen from the representative applied stress/mechanical strain hysteresis loops in Appendix C, the linear assumption was true for many of the loops (if not linear, the loop was very narrow). For a few of the loops, the ends were either open ended or the loops were relatively wide and slightly nonlinear. In either of these cases, the maximum and minimum strains will give an effective modulus to be used for comparison purposes.

2. Modulus Behavior.

The resulting modulus plots for the IP, OP, and IF tests can be found in Figures 13, 14, and 15, respectively. The cycles axis for these plots are logarithmic.

The moduli for all but the lowest stressed IP and IF tests exhibit little or no change as was revealed by the strain response plots previously discussed. As before, this lack of significant change indicates that these specimens did not suffer fatigue damage accumulation. Instead, the failure involved matrix creep ratchetting and the small drops in the modulus near the end of specimen life most likely indicate small amounts of fiber breaking. Therefore, it can be concluded that the IP and IF specimens mostly suffered a fiber dominated failure. However, this was not

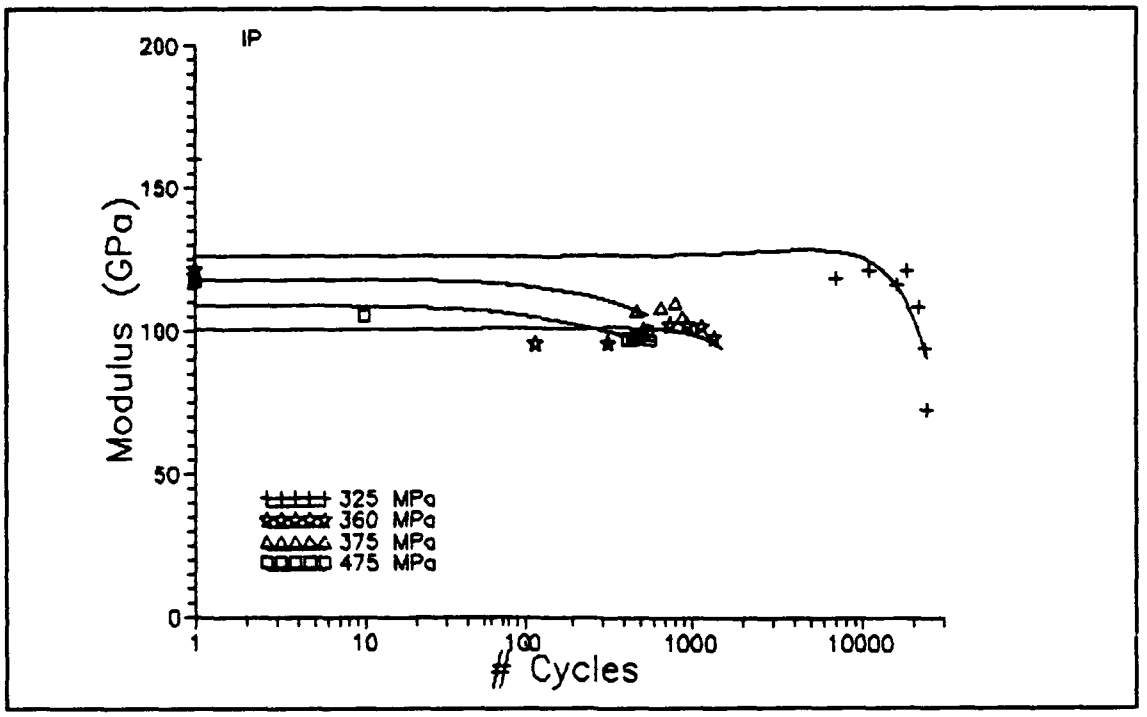

Figure 13. Modulus History for IP Tests

the case for the lowest stressed IP and IF specimens. The large drops of these specimens seem to exhibit the presence of damage accumulation toward the end of their lives thus indicating more of a matrix dominated failure.

On the other hand, the modulus for all but the highest stressed OP specimens disclose a similar failure mode as the lowest IP and IF specimens. The moduli are all constant during the initial stages of the tests followed by a significant decrease prior to failure. This effect was also shown by the "widening" of the maximum and minimum strain curves discussed earlier and is the result of matrix fatigue

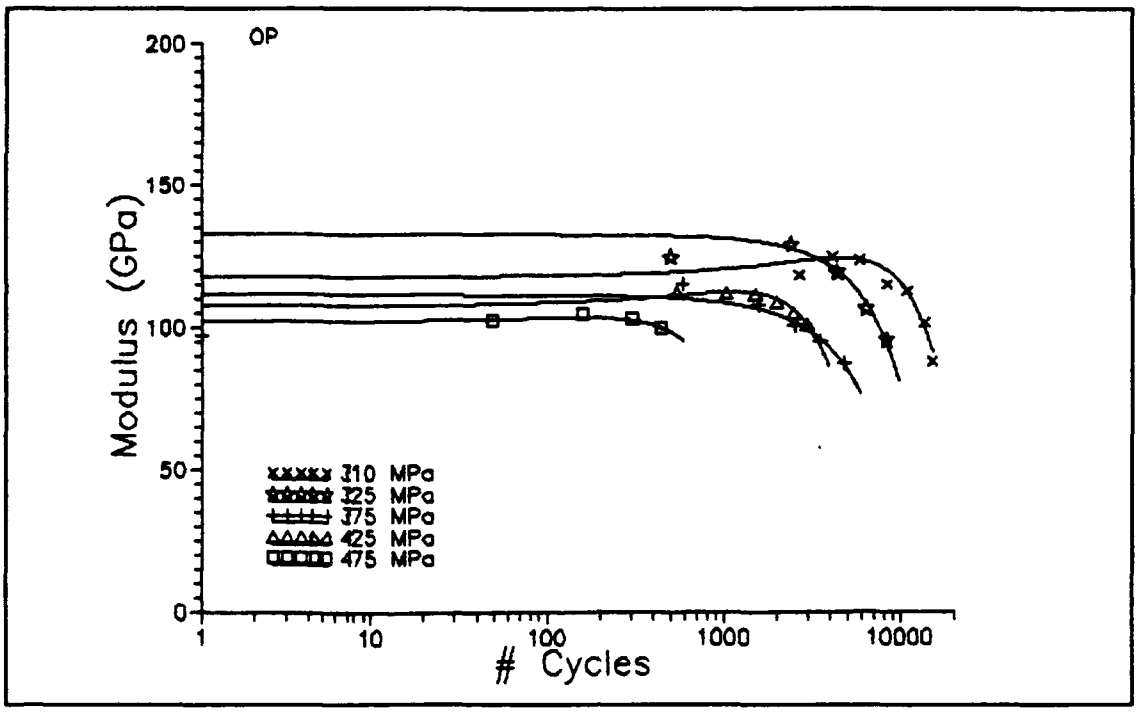

Figure 14. Modulus History for OP Tests

and damage accumulation. The damage progression is most likely due to the fiber/matrix debonding in the 90° plies and possibly the 45° plies due to a lack of strong interface bonds. Ultimately, the failure was matrix dominated. However, the small drop in modulus for the highest stressed OP specimen is attributed to the same failure mode as for most of the IP and IF specimens - fiber domination.

It must be noted that in all cases where a decrease in the modulus was detected, especially in the longer tests, it is assumed that environmental degradation of the interface is a factor in the specimens' ultimate failure.

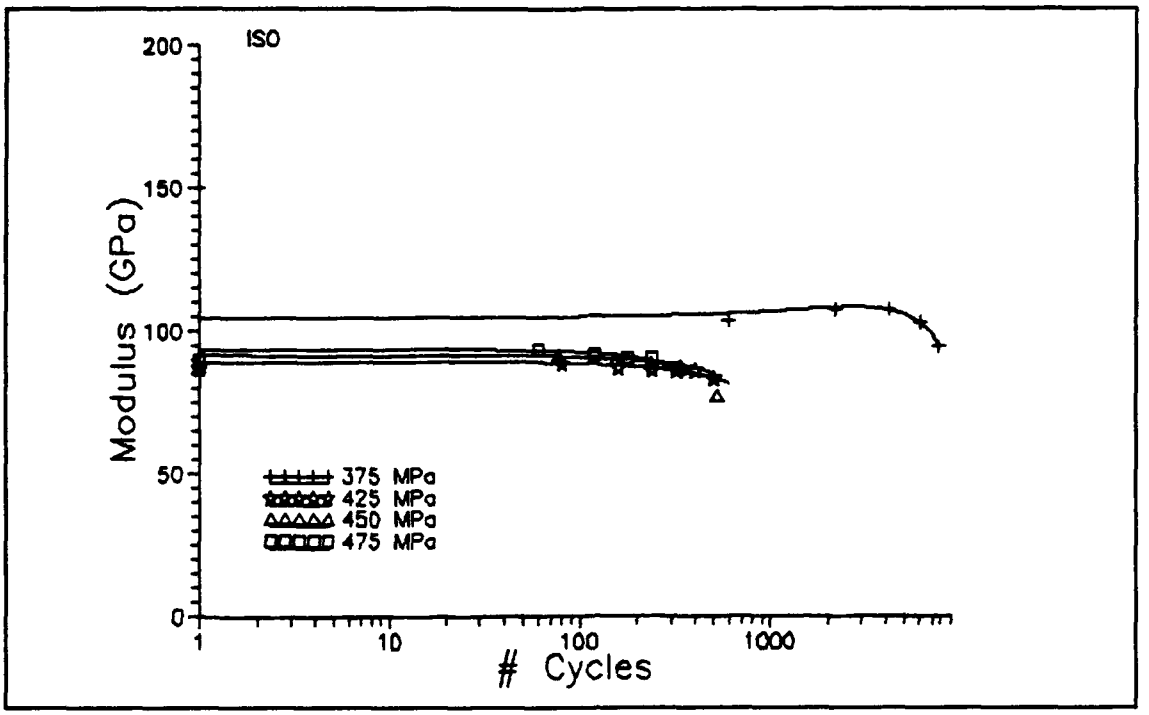

Figure 15. Modulus History for IF Tests

D. Fracture Analysis

Two different methods were employed for analysis of crack damage and specimen fracture. The first was the replication technique as described in Chapter III using an optical microscope. This method allows the examination of crack progression along the polished edge of each specimen in a real time fashion. The second was the sectioning technique also as described in Chapter III using an AMRAY scanning electron microscope (SEM). Here, one half of each fractured specimen was sectioned into three pieces: the fracture surface, a transverse edge from just below the

fracture surface, and a longitudinal edge from the center portion just below the fracture surface. Note: specimen failure is defined as the separation of each specimen into two complete sections. Also, the lines of sight for the following replica, fractography, and metallography figures are given in Figures 5a and 5b.

1. Replica Results.

Initial replicas with minimal load (from 10% to 50% of the static load that defined the first point of non-linearity) were taken on each specimen before any testing was accomplished to establish a specimen edge baseline (see Figure 16). Subsequent replicas were compared to these

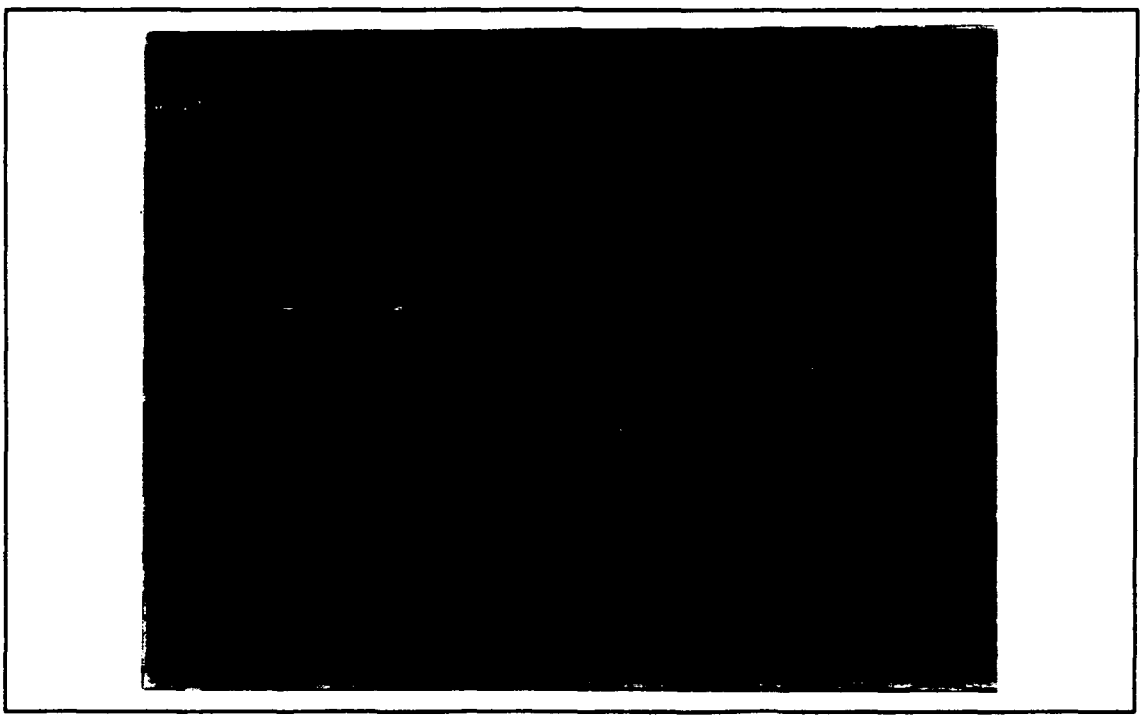

Figure 16. Baseline Replica Prior to Cycling

initial replicas to determine the fiber and matrix anomalies (cracks and debonds) that existed prior to testing. Four general trends were noted:

a. 0° fiber cracking. Cracking was present in the 0° fibers for all three cycling profiles throughout the entire range of maximum applied stresses. They usually appeared after only the first few cycles (less than 15). However, the cracks did not propagate through the fiber cores - the crack simply surrounded the core without affecting it (refer to Figure 17). As the number of cycles increased on each specimen, so did the number of cracked 0° fibers. Also, no indications were found of these fiber cracks progressing

Figure 17. 0° Fiber Crack

into the adjacent matrix. Since they were present in all cases and seemed to be unrelated to test conditions and applied stress levels, they were probably caused from edge effects. This same edge effect phenomenon was noted by Schubbe (23:88) and Ermer (5).

b. 45° and 90° fiber debonding. Fiber debonding was made apparent on the replicas by two obvious rings that surrounded the fiber impressions on the acetate - a thinner dark line surrounded by a wider grayish line (see Figures 18 and 19). In addition, fibers could be seen and felt with the finger extending beyond the specimens' edge surface (after the specimen had cooled down). Initial indications

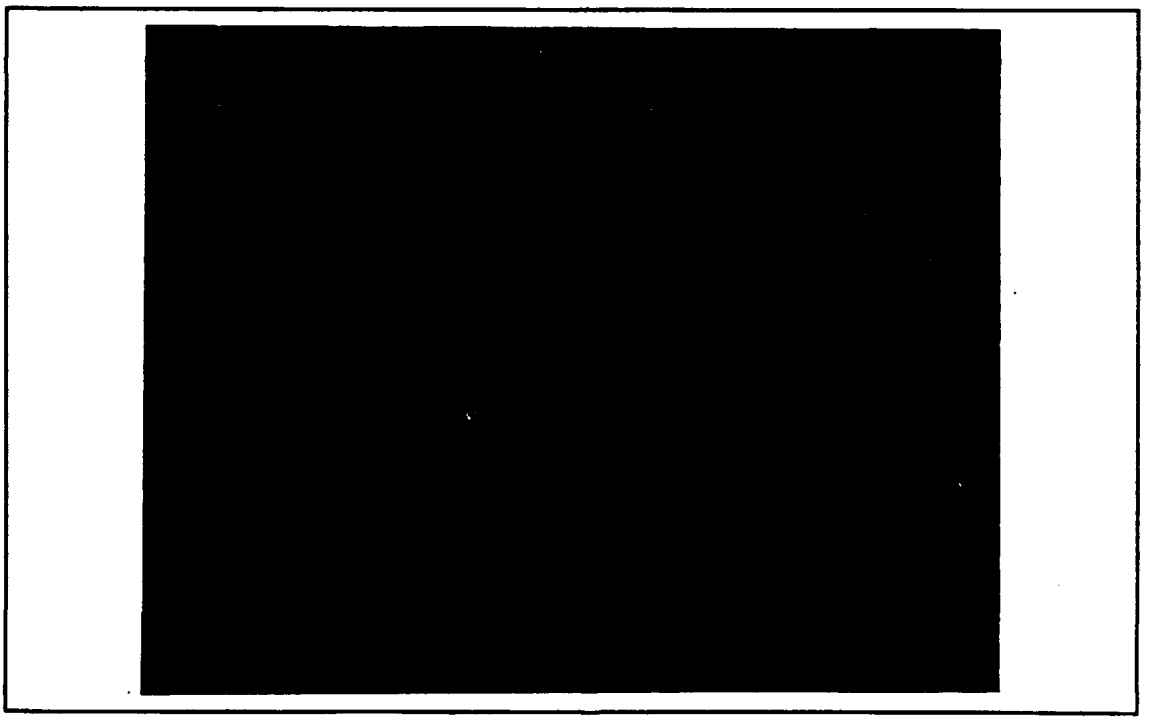

Figure 18. Debonded 90° Fiber

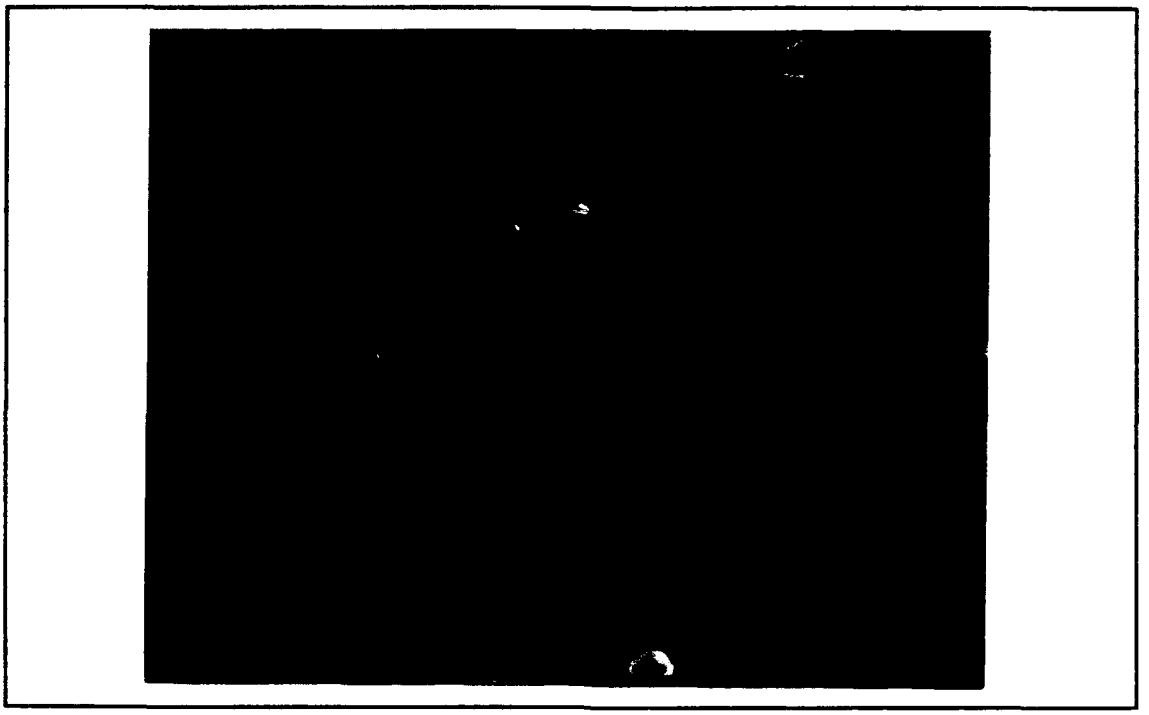

Figure 19. Debonded 45° Fiber

of the debonding were seen within the first 500 cycles of testing through the entire range of maximum applied stresses. In some instances, these indications appeared within the first 10 cycles, but no correlation of stress level or cycling profile could be made. One obvious trend did appear, though, in that both the 45° and 90° fiber debonding was only seen on the IP and IF cycling, while the OP cycling showed evidence of just 90° fiber debonding.

Reasons for fiber debonding can be explained as follows: The debonding of the 90° fibers most likely results from Poisson's effect in the matrix. As the mechanical load is applied, the transverse width of the specimen reduces. The

matrix/fiber interface strength cannot resist this shrinking resulting in interface shearing. As a consequence, the 90° fibers extend beyond the surface.

Debonding of the 45° fibers may result from the same Poisson's effect but to a lesser degree. Because the fibers lie at a 45 degree angle with the load and transverse material shrinkage, the effective fiber/matrix interface strength is higher. Also, the fibers may tend to be pulled in the direction of the load, in essence, moving with the matrix flow. The result may be a net consequence of fiber extension (fiber pullout), fiber retraction (fiber pull-in), or neither.

In addition to the Poisson's effect, debonding may also be a function of the difference in coefficients of thermal expansion between the fiber and matrix. However, this is probably not a large contributing factor as discovered by Schubbe (23:58-61). He cycled a cross-ply layup SCS6/Ti-15-3 MMC under thermal-only (no mechanical load) test conditions between 149°C and 427°C. Even after 10,000 cycles, he did not detect transverse matrix cracking (which would lead to a loss in specimen stiffness) or 0° fiber breakage. The conclusion that can be drawn is that there is relatively little damage due to thermal effects alone.

One way the scanning electron microscope was used was to

investigate the edges of failed specimens and determine if the replicas were indeed showing debonding indications. Figure 20 supports the replica debonding results - the 90° fibers are very evidently protruding beyond the specimen edge. The 45° fibers, on the other hand, have been pulled into the matrix. The other side of this specimen (not shown) indicated that the 45° fibers were slightly pulled out, though less than the 90° fibers.

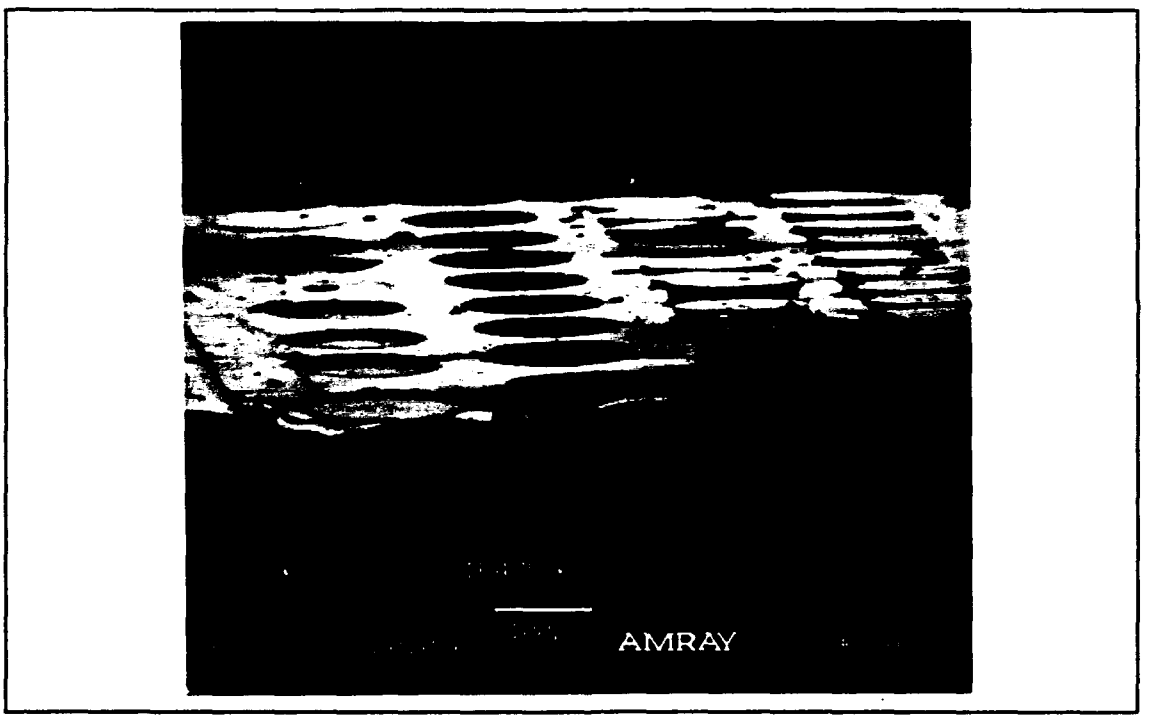

Figure 20. Specimen Edge Showing Fiber Pullout/Pullin

c. Matrix cracking. The presence of damage in the matrix followed two distinctly different trends between the IP and IF cycling and the OP cycling:

1) The higher maximum applied load IP and IF tests did not show any matrix cracking throughout their lives (under 900 cycles). On the other hand, the lower load IP and IF tests showed longitudinal matrix cracks (referred to as delamination cracks by Majumdar and Newaz, 13:11) initiating from the fibers and progressing toward the next fiber in the same ply. As can be seen in Figure 21, the 45° plies showed many more cracks than the 90° plies. The cracks were first detected in these longer life specimens during the initial 500 to 1,000 cycles. It can be surmised that the matrix cracking for both in-phase and isothermal loading is life

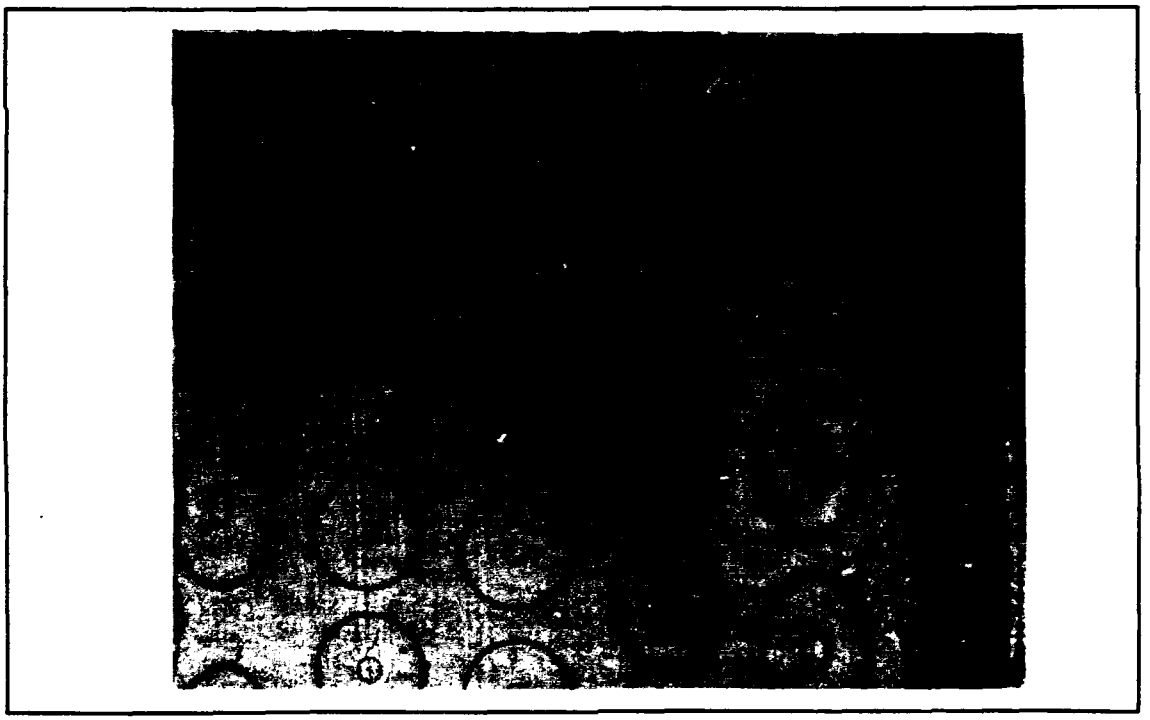

Figure 21. Longitudinal Matrix Cracking, 325 MPa, IP Test, 2,775 Cycles

dependent (over 1,000 cycles) rather than load dependent. Also, because the cracks did not grow to the extent as will be shown for the OP testing, they probably were not of a major consequence to specimen failure.

This cracking tendency correlates well with the modulus plots as discussed before. The trends for both higher load IP and IF specimens showed a small modulus decrease near failure, indicating little if any matrix cracking. Meanwhile, the lowest load IP and IF specimens exhibited a larger decrease in their moduli, thus indicating a larger presence of matrix cracking.

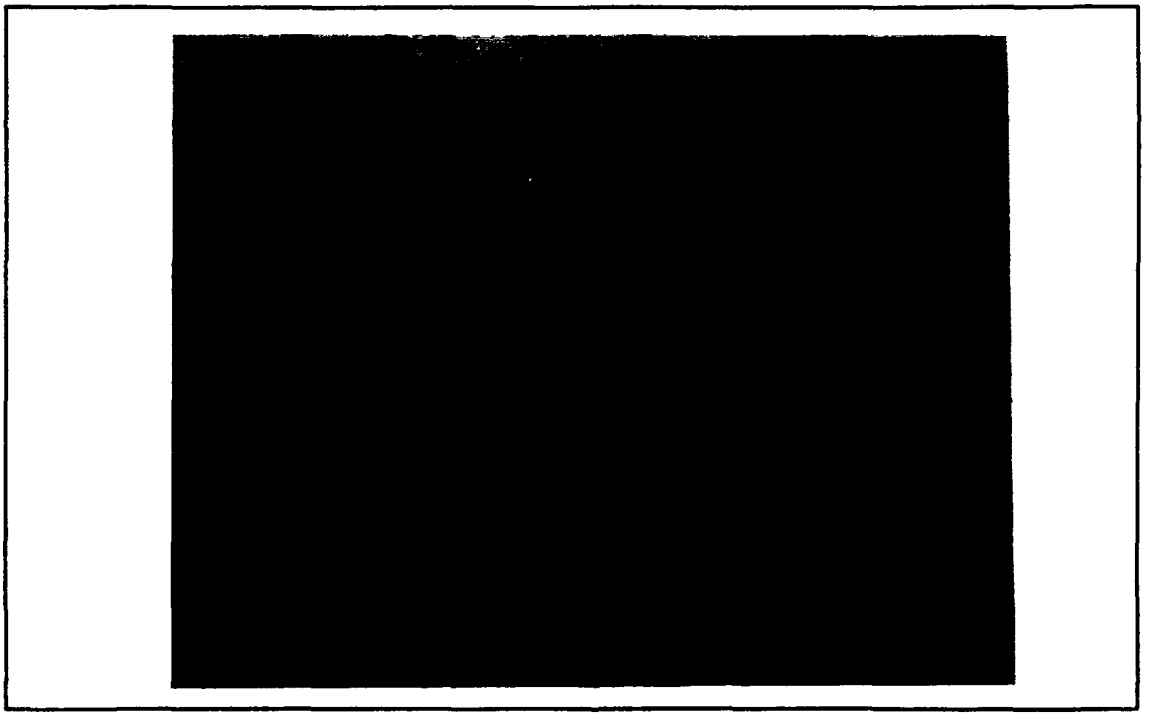

Figure 22. Transverse Matrix Cracking, 325 MPa, OP Test, 1,664 Cycles

2) The OP specimens showed transverse cracking in all tests also after the first 500 to 1,000 cycles of life (as was seen for the longitudinal cracking in the lower load IP and IF tests). Once these cracks had initiated, they both grew in length and in numbers throughout the specimens' lives as shown in Figures 22, 23, and 24. The cracks ran from edge to edge around fibers as well as emanated from the sides of fibers. The existence of the transverse cracks was definitely more prevalent than the longitudinal cracks in the lower stress IP tests which also correlates well with the modulus plots. As can be seen from Figure 14, except

Figure 23. Transverse Matrix Cracking, 325 MPa, OP Test, 2,906 cycles

for the highest load OP test (where cracking did not have much time to propagate), all the specimens' moduli saw dramatic decreases toward the last portion of their lives. Thus, both of these results leads to the same conclusion that OP TMF cycling produces matrix dominated failures. Additionally, short longitudinal delamination cracks were evident after 1,200 to 1,600 cycles in the lower load OP tests. As seen with the IP and IF testing, these cracks may have contributed to specimen failure but probably not to a serious degree.

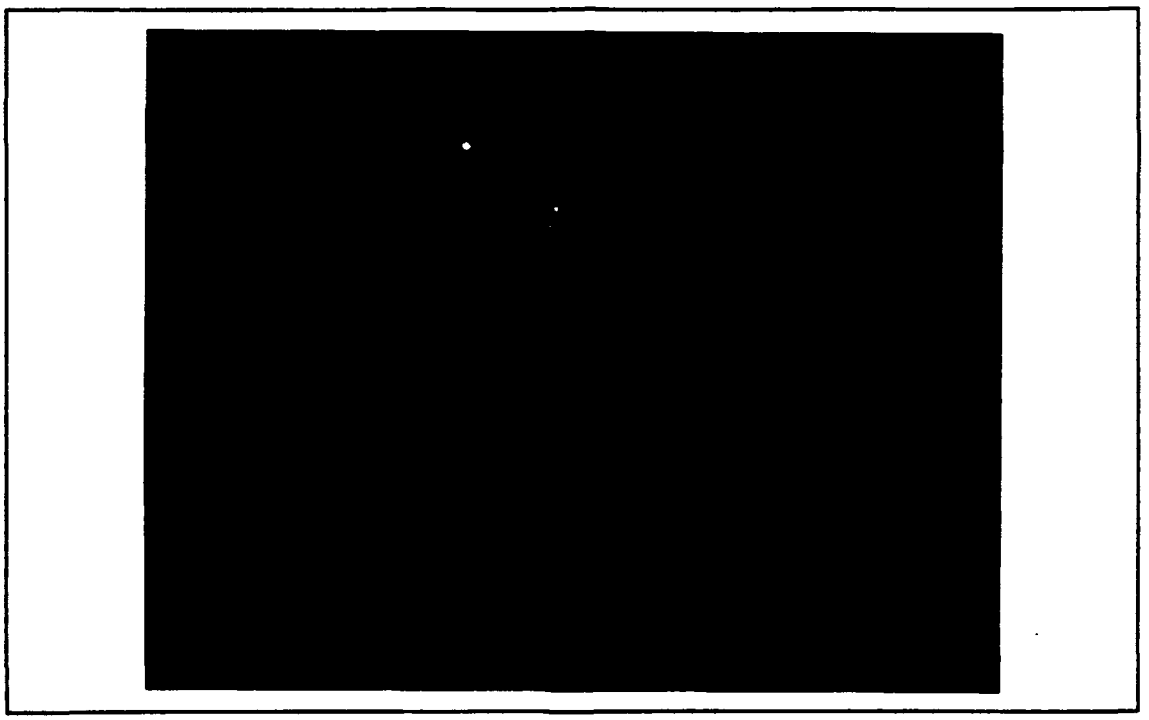

Figure 24. Transverse Matrix Cracking, 325 MPa, OP Test, 5,001 Cycles

d. Possible delamination indications. An interesting anomaly was detected within the first 500 cycles of each test (except for IP475 where it was not detected at all) which had the appearance of longitudinal "bubbles" (see Figure 25). These bubbles were relatively small in size, did not grow larger, were not concentrated in limited areas of the specimen edge, ran between 45° fibers and also between 90° fibers, and became more apparent throughout the lives of the specimens. One possibility is that they could be indications for ply delaminations or voids. As was described in Chapter III, the laminate was manufactured by pressing thin sheets of titanium foil around continuous

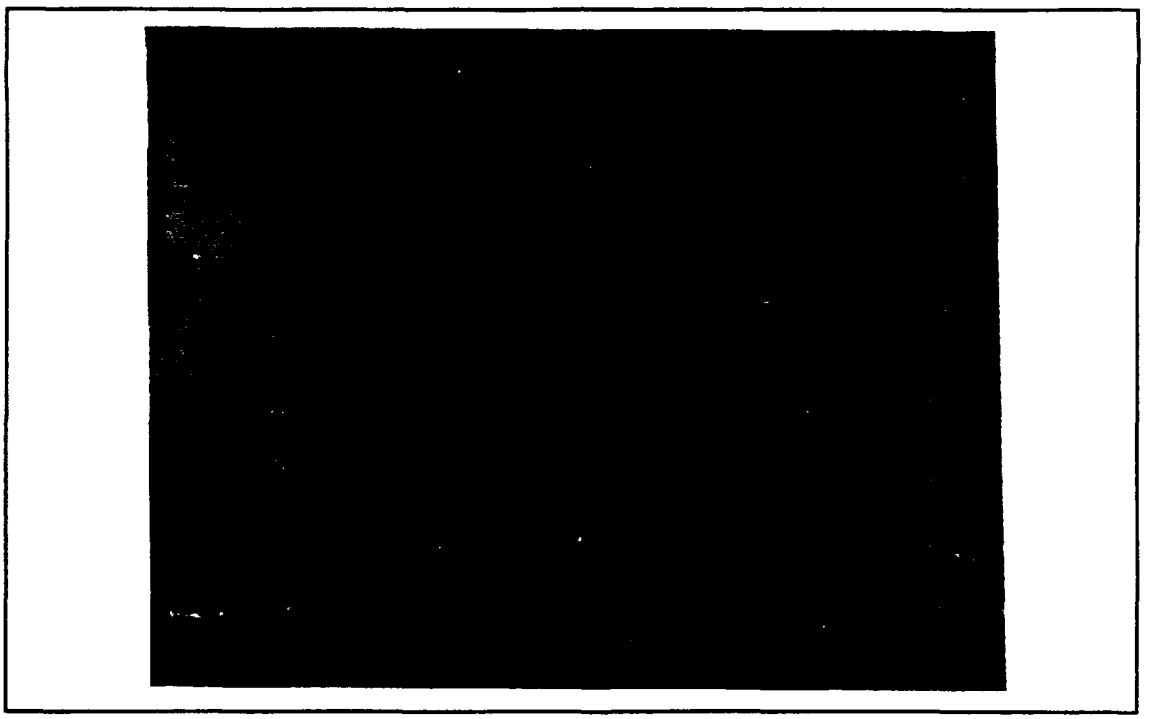

Figure 25. Bubble Anomaly

fibers. Ply boundaries would then naturally exist between the longitudinal fiber rows. Throughout the life of the specimens, no obvious delaminations were detected (other than the longitudinal cracking mentioned earlier) and no cracks were found to appear through the bubbles or emanate from the bubbles.

2. Fractography Results.

Upon examining all of the fracture surfaces, two main conclusions can be made: 1) the fibers did not fail from fatigue, they either failed from overload or from matrix cracks that first propagated around the fibers then through them; and, 2) the failure was both load dependent and profile dependent.

The IP and IF specimens exhibited very similar failure trends. The more highly stressed IP and IF specimens had fracture surfaces that were largely uneven with generally two different matrix type failure zones - one brittle and one ductile as shown in Figure 26. The matrices of the 90°, 45°, and portions of the 0° plies displayed a brittle matrix fatigue failure with a definitive plateauing effect (multiplanar) and fiber pullout. As many cracks initiated in the matrix, they propagated on different levels seemingly deflected from their original path directions. Schubbe's investigation attributed this phenomenon of crack tip de-

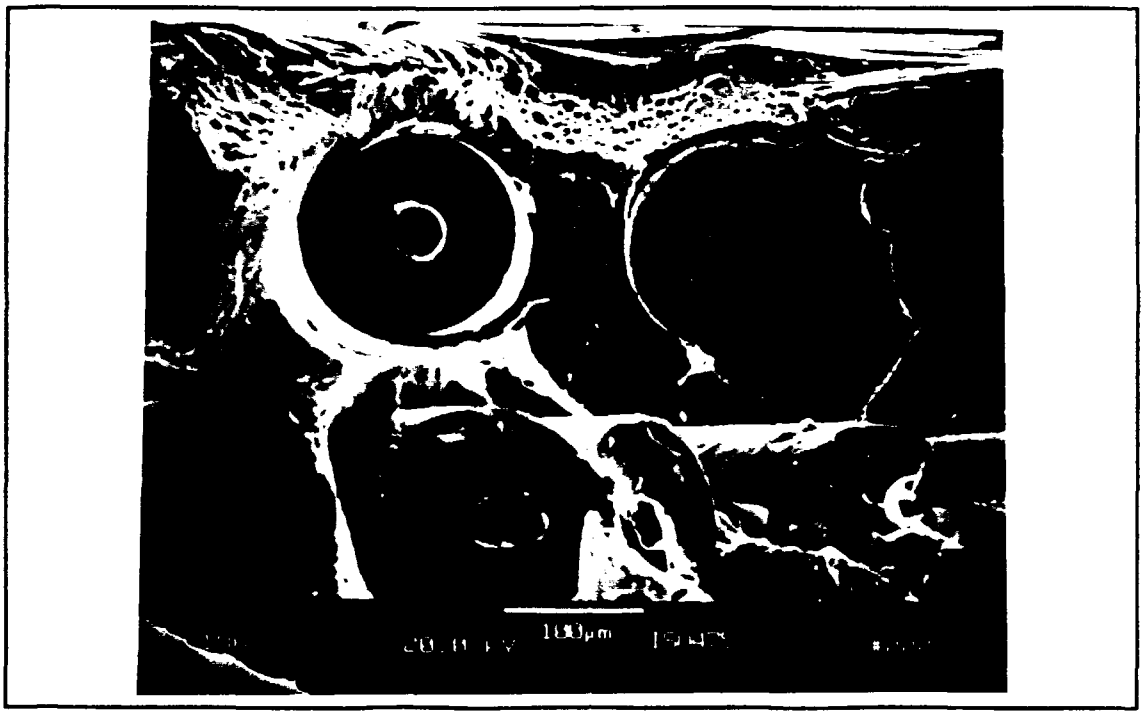

Figure 26. High Load IF Test Showing Both Ductile Matrix and Brittle Matrix Failures

flection to the high loading stresses. When the transverse loading stress σ_{22} reached a critical value relative to the applied longitudinal stress σ_{11}, the transverse crack is deflected 90° from the original direction. After the matrix cracks in the different planes grew and later coalesced, an uneven failure site resulted (23:83-85). The fracture surfaces of the IP and IF cycling, both at 475 MPa, are shown in Figures 27 and 28, respectively.

On the other hand, the corners of the fracture surface displayed distinct ductile matrix failure and ductile necking around the fibers as shown in Figure 29. The fibers and

Figure 27. Fracture Surface of High Load IP Test, 475 MPa

Figure 28. Fracture Surface of High Load IF Test, 475 MPa

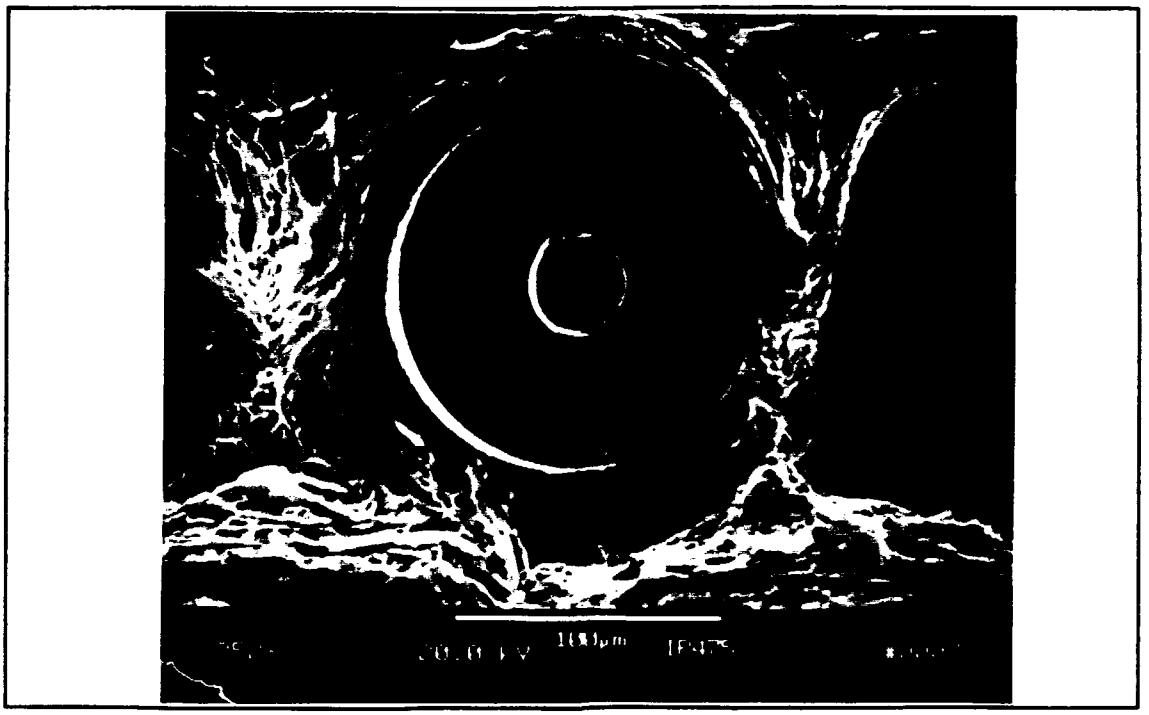

Figure 29. High Load IP Test With Ductile Matrix Failure and Ductile Necking around Fiber

the matrix in this region failed from simple static overload.

Thus, this fracture evidence indicates that cracks initiated in the 90° plies and propagated out toward the 45° and the 0° plies. As this was occurring, the applied loads were being transferred to the 0° fibers. As the fibers began to fail, the load was transferred back to the uncracked portions of the 0° ply matrix. Once all the fibers failed, the matrix soon statically failed leading to the appearance of ductile matrix dimpling. One can conclude then that fiber domination was more prevalent in the overall failure

while matrix damage contributed in part to the failure.

These results support the modulus behavior previously discussed. The higher load IP and IF specimens did not suffer a large decrease in their longitudinal stiffness near the end of life, again showing that fiber domination was more prevailing. Also, as will be seen in Chapter V, the Linear Life Fraction Model (LLFM) was another method in attempting to explain how the specimens failed throughout their lifetimes. The LLFM results indicated that overall failure of the more highly loaded IP and IF cycling contained a stronger tendency toward fiber domination but not totally - matrix failure played a minor role.

Examination of the low load IP and IF fracture surfaces revealed more of a mixed failure mode. See Figures 30 and 31 respectively. Absent was the definite ductile zone near the corners of the 0° plies. Present were randomly interspersed "pockets" of ductile matrix failure between pockets of brittle matrix fatigue failure. The overall failure surfaces were more planar with less fiber pullout - the fibers were broken closer to the surface. The maximum applied stresses were most likely lower to a point where the transverse matrix tensile stress, σ_{22}, may not have reached a critical point as often thus reducing the opportunity for matrix crack tip deflection. Hence, the fracture site was flatter. This stronger tendency toward a matrix failure

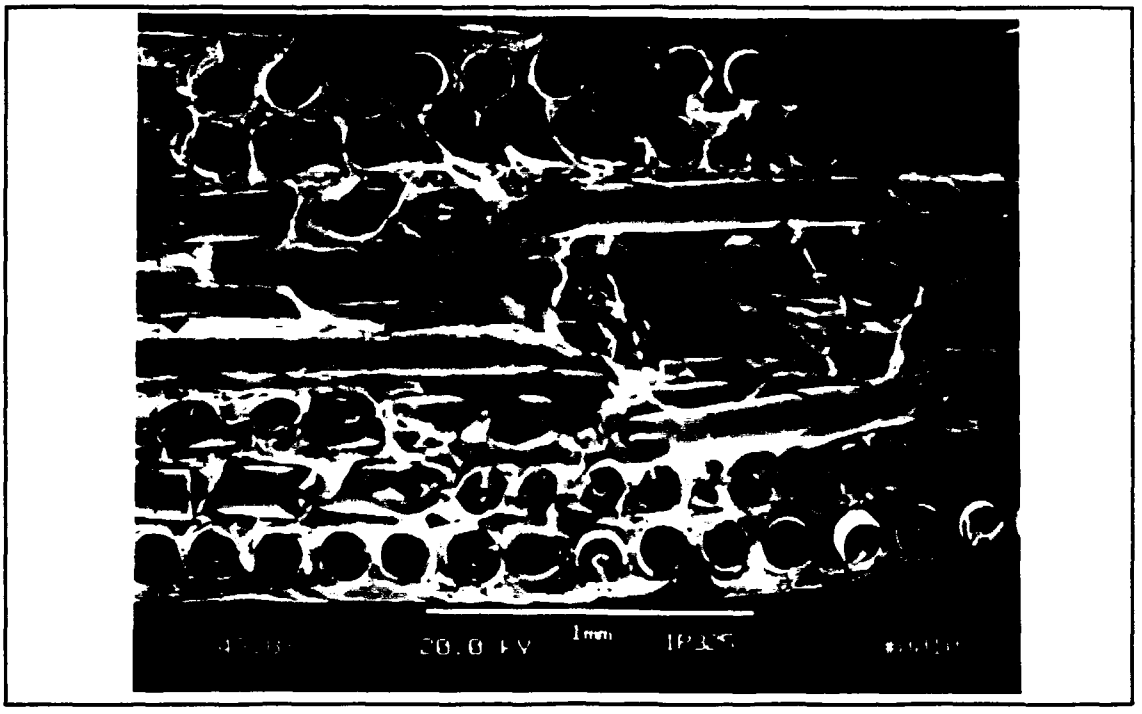

Figure 30. Fracture Surface of Low Load IP Test, 325 MPa

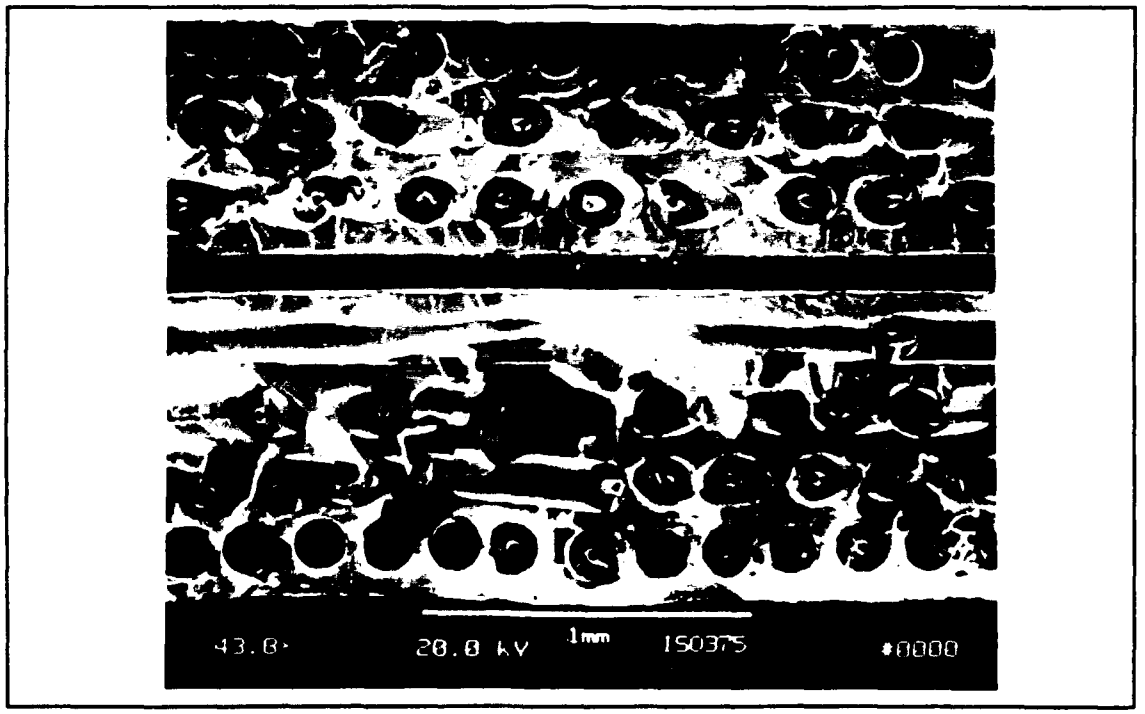

Figure 31. Fracture Surface of Low Load IF Test, 375 MPa

domination is further supported by the modulus behavior. The low load modulus plots for both the IP and IF specimens exhibited relatively larger declines (than the higher load plots) thus showing indications of matrix cracking and failure.

The conclusion can be drawn that, from the stronger indication of fiber domination at higher loads and the randomness of matrix ductility and brittleness at lower loads, 325 MPa and 375 MPa could be shifting points in the overall failure mode for IP cycling and IF cycling, respectively. Testing at even lower maximum applied loads could indicate a stronger matrix dominated failure mode.

Assessment of the OP specimen that had received the highest maximum applied load revealed very similar characteristics as its counterparts in the IP and IF cycling. The fracture surface was uneven, though to a lesser degree, and two different matrix type failure zones were present, as with the IP and IF specimens - a brittle matrix fatigue region and distinct ductile matrix failure regions limited to the corners at the 0° plies. As with the more highly loaded IP and IF cycling, this indicates more of a fiber dominated failure. Refer to Figure 32. Again, this behavior is in agreement with the modulus conclusion - the high load OP plot demonstrated little if any modulus decline near the end of specimen life indicating more of a fiber dominat-

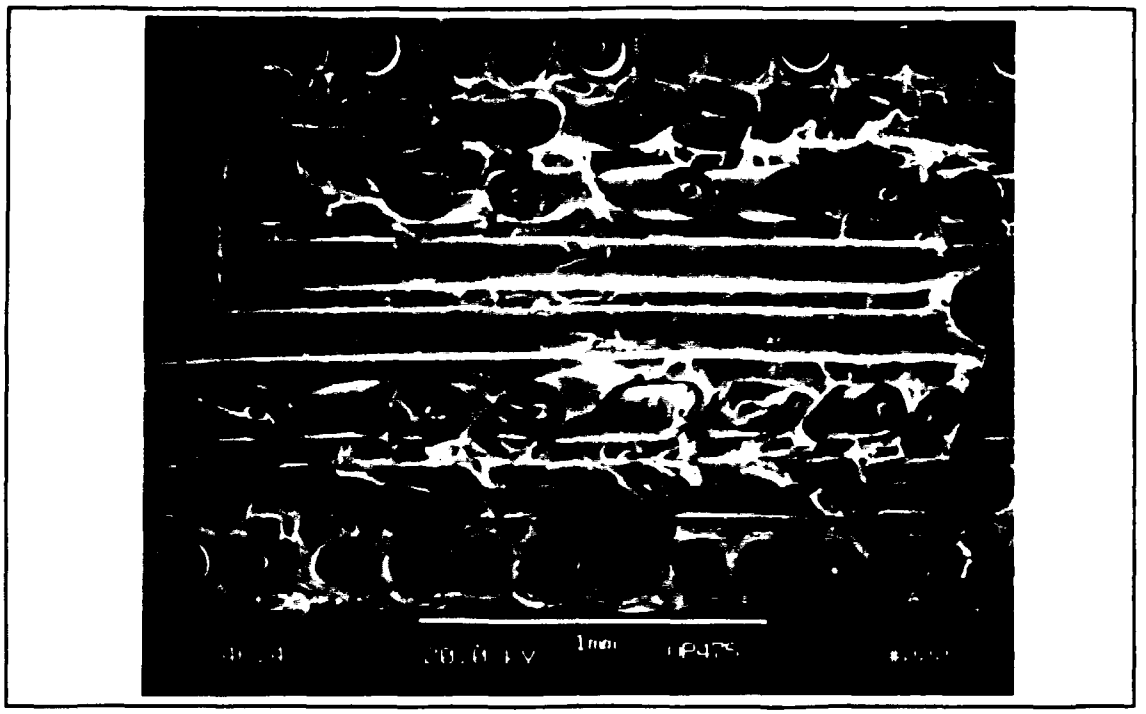

Figure 32. Fracture Surface of High Load OP Test, 475 MPa

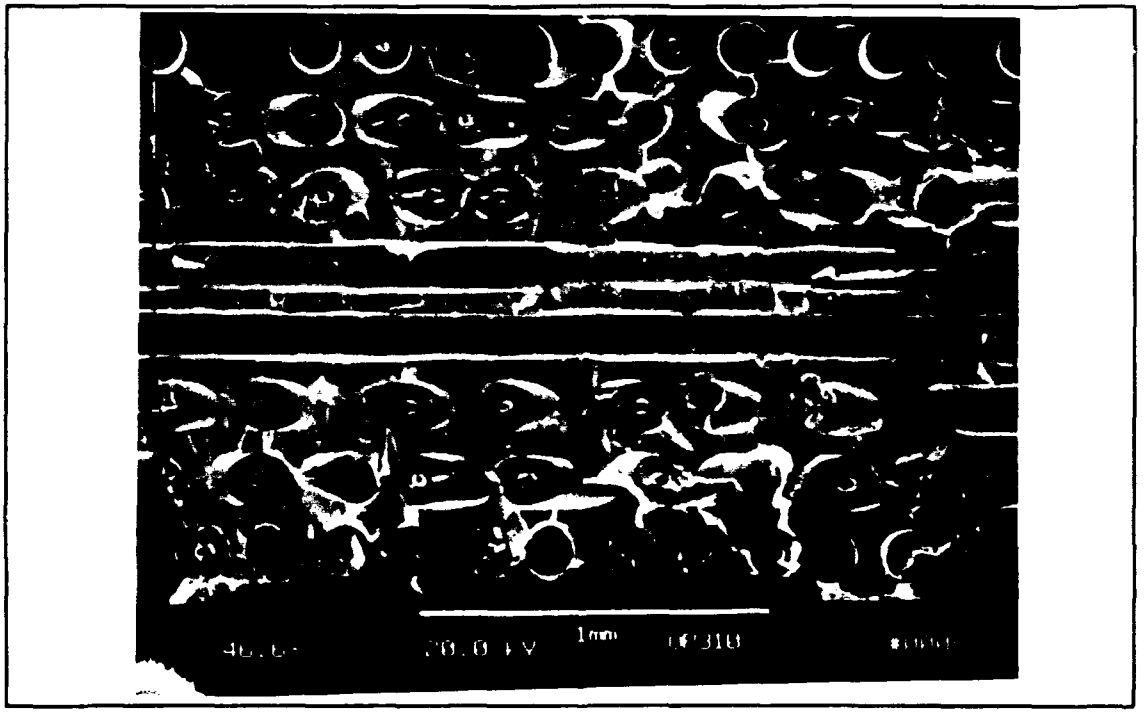

Figure 33. Fracture Surface of Low Load OP Test, 310 MPa

ed failure as with the high load IP and IF cycling.

The fracture surface of the OP specimen with the lowest maximum applied load, on the other hand, displayed brittle cleavage failure throughout the entire area as shown in Figure 33. It had a flat, even surface with little or no fiber pullout - the fibers fractured along the same plane as the matrix as shown in Figure 34.

Also apparent from evaluating the fracture surface was that crack initiation occurred in two locations: the specimen's 0° ply surface and the fiber/matrix reaction zones of the various plies, the two weakest sites in the matrix (refer to Figures 35 and 36). Bates attributed the crack

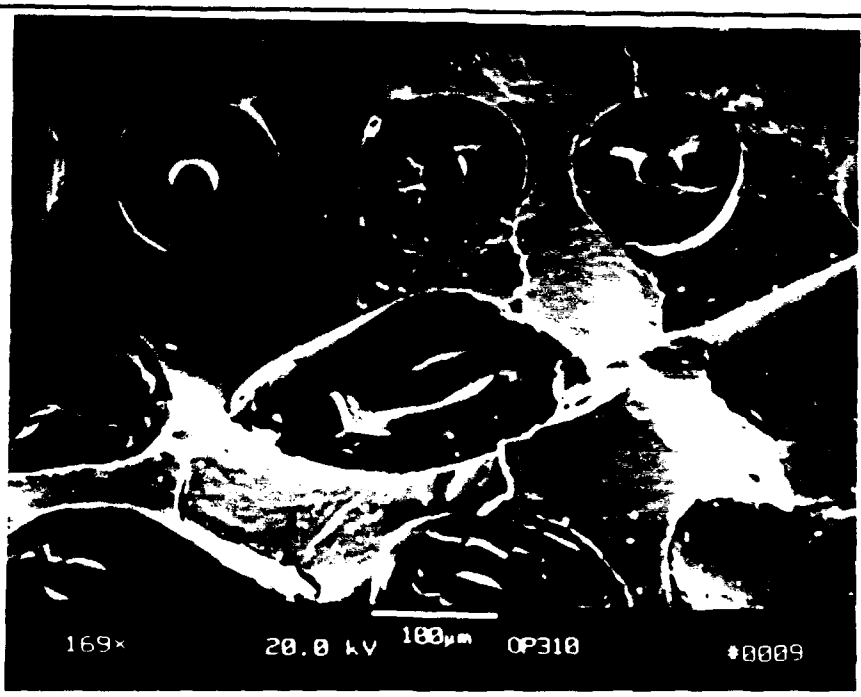

Figure 34. Flat, Even Fracture Surface of OP Test, 310 MPa

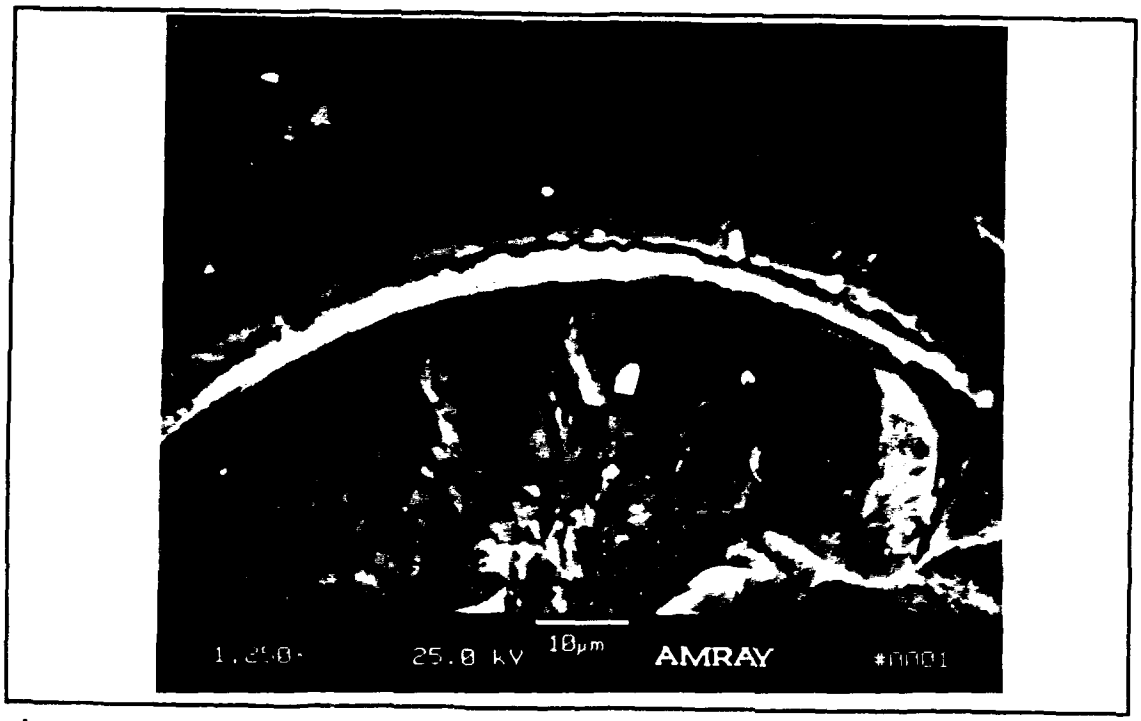

Figure 35. Separated and Weakened Reaction Zone, OP-310 MPa

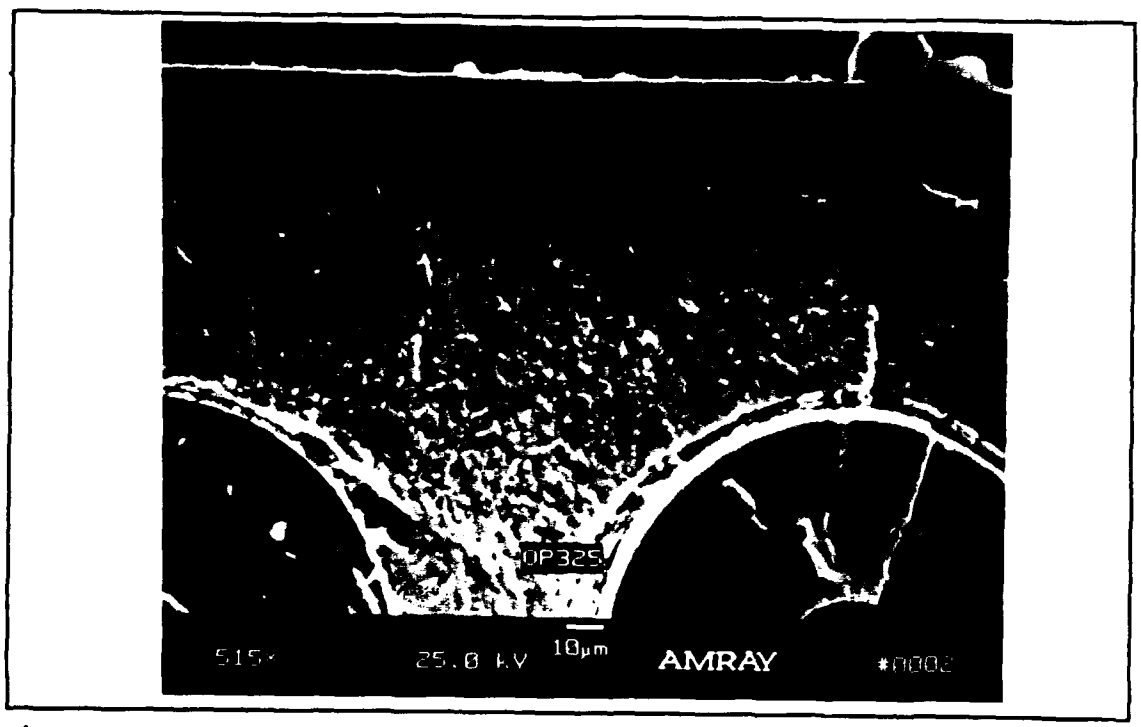

Figure 36. Striations in Matrix, OP Test, 325 MPa

initiation at these two sites to oxidation forming on the specimen's surface caused by the thermal cycling and to the strength degradation at the reaction zone caused by the manufacturing process of the composite (2:34). Majumdar and Newaz's investigation agreed - they disclosed the fiber/ matrix reaction zones are inclined to have lower fracture strength (13:12). Thus, cracks tend to start here sooner.

The fracture surface therefore indicated that the strain range was most likely below the fatigue limit of the fibers, but not of the matrix. Transverse cracks initiated and grew throughout the matrix in the same plane coalescing to form the fracture surface. The fibers failed early due to local stress concentrations in the fibers caused by the matrix cracking and/or local environmental attacks of the fibers (10:11). This evidence clearly indicates a strong matrix dominated failure and correlates well with the modulus results.

In light of the fractography results from IP, OP, and IF cycling, both high and low maximum applied loads, it can therefore be asserted that the failure modes of the specimens are dependent on both the applied stress levels and the loading profiles to which they are subjected to.

The fracture surface of the specimen that underwent static failure at an elevated temperature of 427°C was also examined. As expected from evaluating Figure 37, the entire

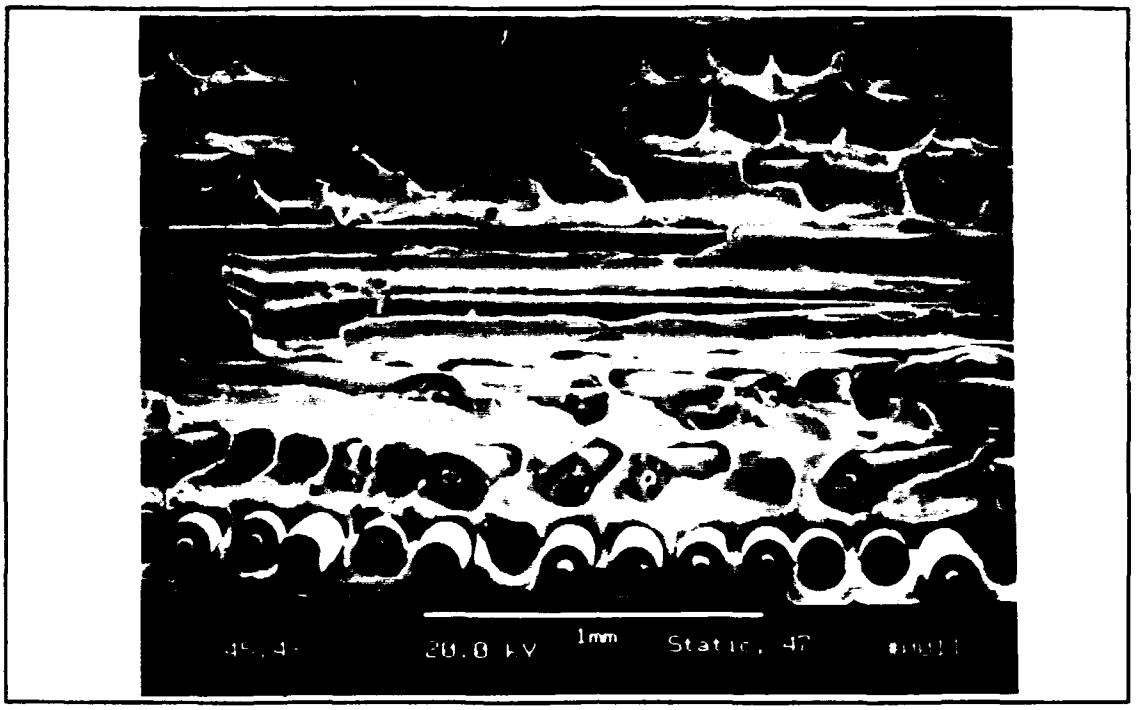

Figure 37. Fracture Surface of Static Test, 427°C

surface was highly irregular, there was a high degree of fiber pullout, and the matrix exhibited ductile dimpling and ductile necking around the fibers. The dimpling and necking was the same as shown in Figure 29 for the high load IP, IF, and OP tests. An interesting characteristic noted was, when viewing the specimen along its edge, the overall surface was at an approximately 45° angle - similar to what is expected from a static overload of a monolithic material.

These results clearly indicate a fiber dominated failure. As the 90° and 45 ° plies were failing the load was transferring to the 0° fibers. When their maximum stress limit was exceeded, the load transferred to the matrix of

the 0° ply which also failed soon after leading to the ductile dimpling effect in the matrix and the high degree of fiber pullout.

3. Metallography Results.

The sectioned failure regions of all specimens (transversely 1.5 mm to 2.5 mm below the fracture site and longitudinally as shown in Figure 5b in Chapter III) were examined to further evaluate the failure mechanisms.

All the test specimens, from the IP, OP, and IF profiles, revealed transverse cracks in the matrix (similar to what is shown in Figure 38) and broken fibers (similar to what is shown in Figure 39); however, and very importantly, the appearance of both were to varying degrees based on stress level which will be discussed shortly. Many 0°, 45°, and 90° fibers appeared debonded, usually closer to the fracture site or a crack, and was denoted by a rough black line between the fiber and the matrix or the fiber and the reaction zone (the latter can be seen in Figure 40). In many instances, the reaction zone itself was separated from the matrix (also as shown in figure 40 - the thin, uneven black line perpendicular to the matrix crack is the debonded area between the reaction zone and the light gray matrix below).

Additionally, in all specimens, a fiber/matrix reaction

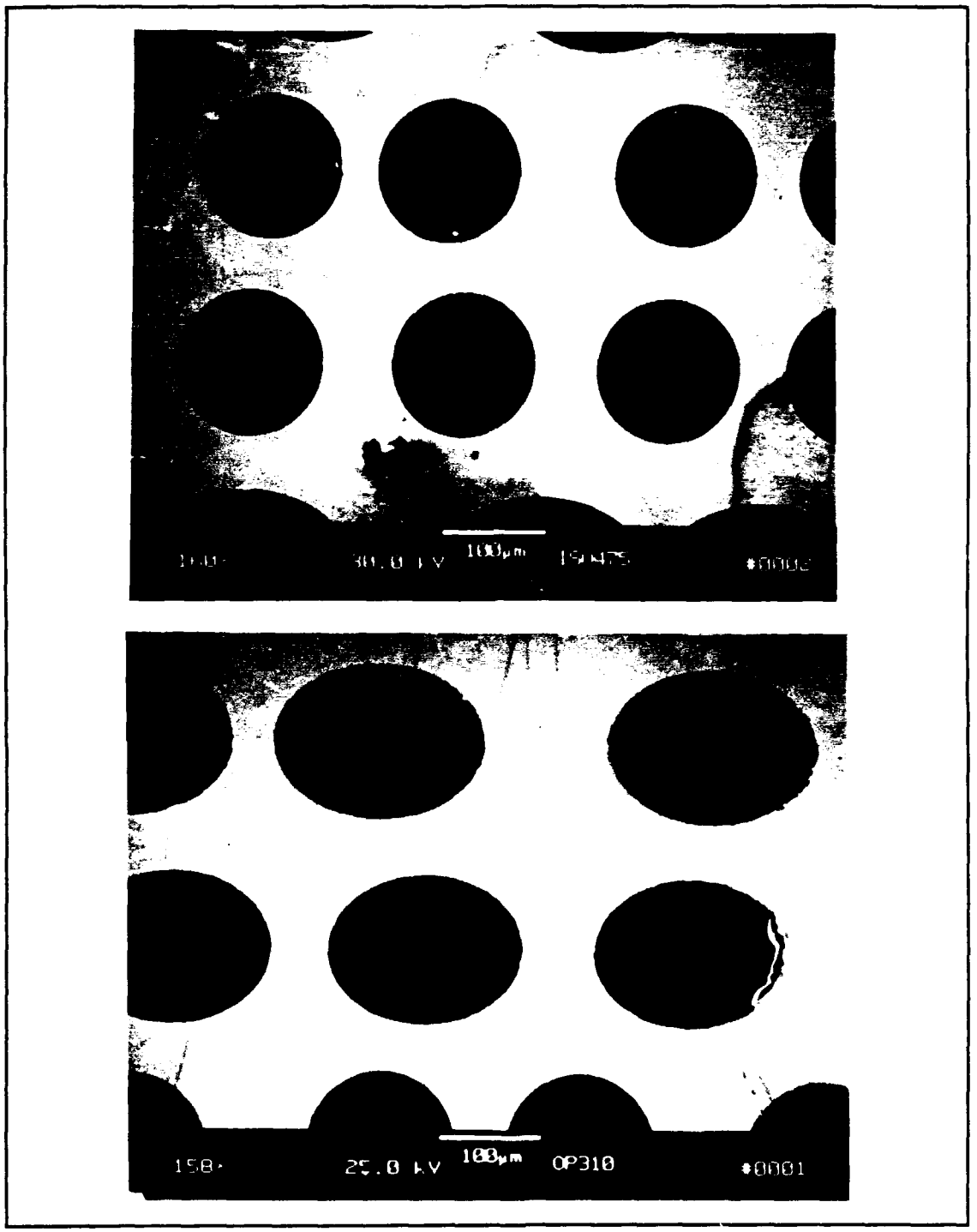

Figure 38. Transverse Matrix Cracks, IF Test, 475 MPa (TOP); OP Test, 310 MPa, (BOTTOM); Both are Longitudinal Sections

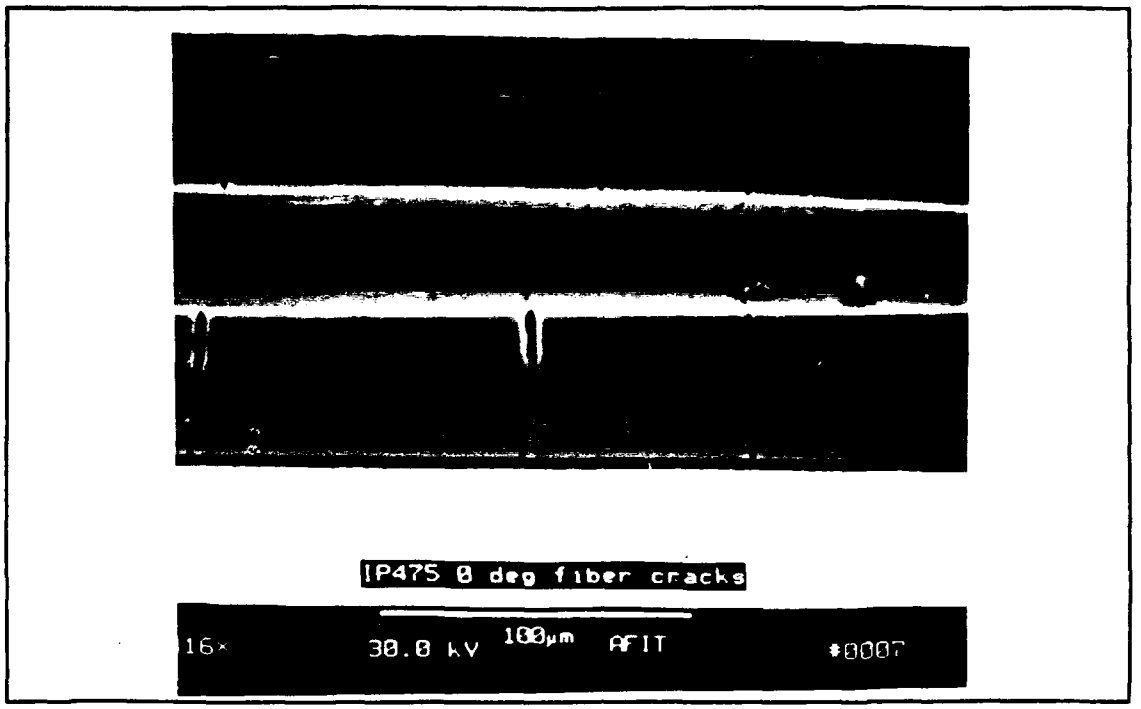

Figure 39. 0° Fiber Cracking, IP Test, 475 MPa, Longitudinal Section

zone usually appeared at the site of crack propagation around the fiber as shown by Figure 41. Note the adjacent 90° fiber without any noticeable reaction zone. As discussed earlier, Bates attributed the strength degradation of any reaction zone to the composite's manufacturing process. Once the zone thickened, according to Majumdar and Newaz, its fracture strength declined thus increasing the tendency for crack initiation.

As previously mentioned, two important trends were noted with respect to the degree of fiber and matrix cracking:

a. The high stress tests of all three profiles displayed

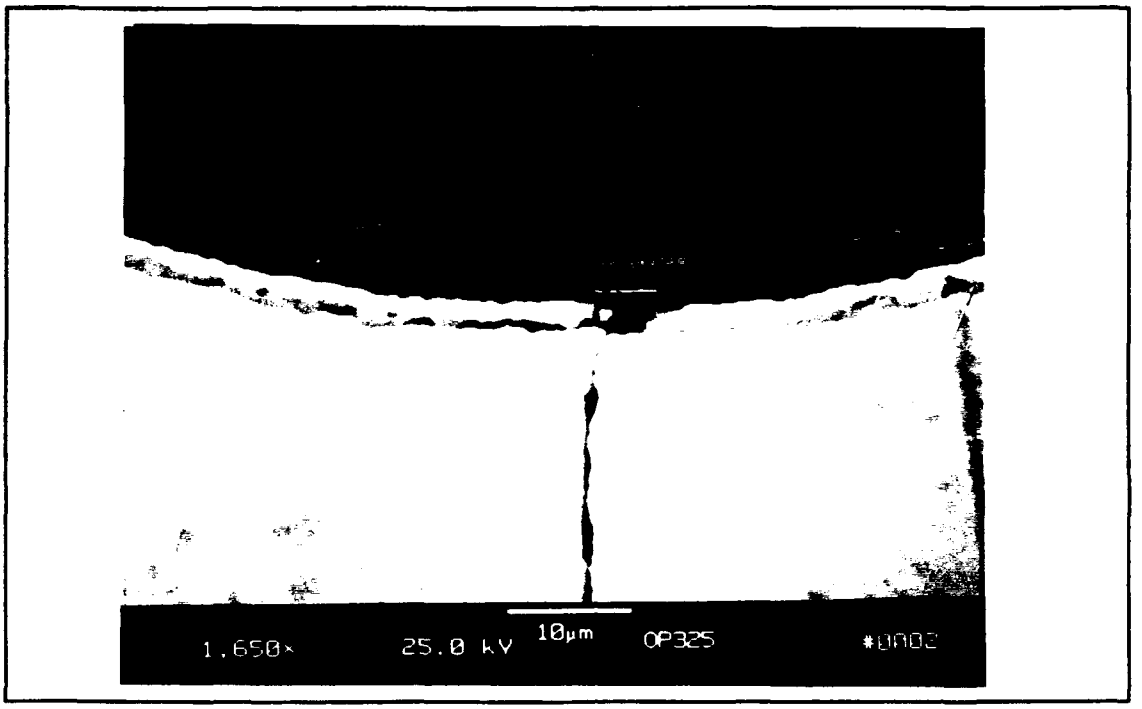

Figure 40. Debonding

more numerous cracks in the 0° fibers than the low stress tests. The presumption can be made that the fibers received most of the high stress loading. As they began to fail, their load was transferred to the matrix. It too failed rather quickly (hence the fewer matrix cracks and the ductile dimpling as shown by the fractography results) ultimately leading to specimen failure.

b. Conversely, as Figure 38 indicates, the lower stress tests displayed more numerous transverse matrix cracks than the high stress tests. The lower applied stress was not high enough to cause early fiber failure which allowed more time for matrix crack growth. These cracks propagated and

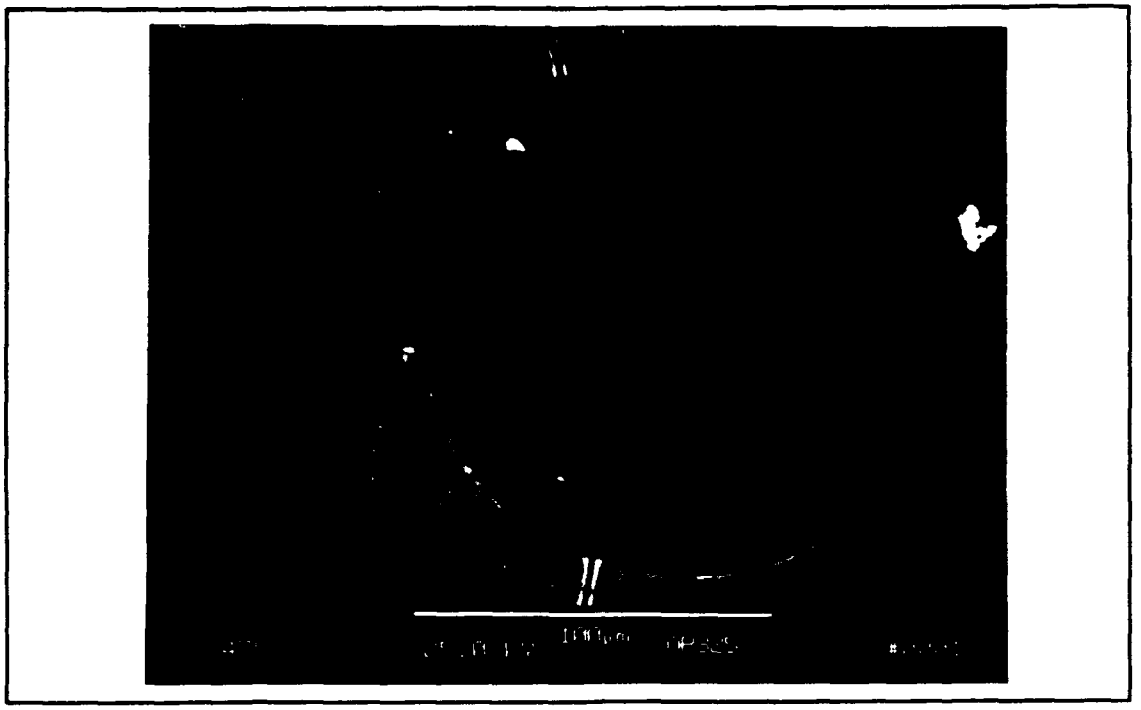

Figure 41. Thickened Reaction Zone Due to Matrix Cracking

coalesced until they transferred their load carrying capabilities to the fibers. The fibers accepted the additional stress until they too reached their limit ultimately resulting in specimen failure.

These two trends support the earlier reasoning from the fractography analysis that the failures from high stress tests tend to be more fiber dominated and the failures from the lower stress tests tend to be more matrix dominated.

Investigation of the static test specimen (tested at 427°C) revealed a broken 0° fiber but no matrix cracks as expected. Debonding was more prevalent on the 45° and 90° fibers with thinner indications of debonding being exhibited

by the 0° fibers. Well defined reaction zones were not detected. Even though the specimen was temperature soaked at 427°C to ensure proper heat distribution, environmental deterioration probably did not have sufficient time to take effect due to the relative shortness of this test compared to the fatigue tests.

The same conclusion can be drawn as with the fractography results - the specimen tested statically at 427°C suffered a fiber dominated failure.

V. Analysis

Several analyses were performed to obtain a better understanding of how SCS_6/Ti-15-3 behaves statically and during fatigue loading. These analyses include:

a. The calculation of ply and laminate engineering properties using classical laminated plate theory, basic strength of materials expressions, and Halpin Tsai equations.

b. The calculation of the fiber and matrix micromechanical stresses in the various plies of the laminate for the different loading profiles. METCAN, the METal matrix Composite ANalyzer computer program, was used as described in Chapter III. These stresses were then evaluated to determine if fiber domination and/or matrix domination failure mode trends could be made.

c. The calculation of a fatigue life predictor that is independent of the loading profile using the Linear Life Fraction Model.

A. Ply and Laminate Engineering Properties.

Classical laminated plate theory, Halpin-Tsai equations, and basic strength of materials expressions were used to determine the ply and laminate engineering properties both before and after debonding of the off-axis plies at ambient temperature. A second set of properties were calculated at

the maximum testing temperature - 427°C. Appendices A and B show these calculations for room temperature and elevated temperature, respectively.

Initially, the fiber and matrix properties from previous studies were used in the rule of mixtures and the Halpin Tsai equations; however, they produced ply stiffnesses (E_1 and E_2) higher than what this study had found experimentally. Since these equations assume perfect bonds between the fiber and matrix (and thus would give higher than real stiffnesses), it can be concluded that perfect bonds must not exist in the as-fabricated material. To adjust for the lack of perfect bonding, correction factors (called β and τ) were arbitrarily determined and satisfactorily incorporated into the matrix stiffnesses, thereby reducing the matrix stiffness, as follows:

1. Room Temperature Matrix Stiffness. A factor, β, was used equal to 0.664:

$$E_m^* = \beta E_m = 0.664 * 91.8 \text{ GPa} = 61.0 \text{ GPa} \quad (23)$$

2. Elevated Temperature (427°C) Matrix Stiffness. A factor, τ, was used equal to 0.697:

$$E_m^* = \tau E_m = 0.697 * 74.9 \text{ GPa} = 52.2 \text{ GPa} \quad (24)$$

These "effective" matrix stiffnesses were then used to

Table 8. Laminate Longitudinal Modulus

Temperature	Experimental (GPa)	Analytical (GPa)	% Difference
Room	140.5	140.4	.1%
Elevated	125.2	129.8	3.7%

determine the laminate stiffnesses. As Table 8 discloses, a very good correlation was achieved between this analysis and the experimental data. Note: the experimental results are the averages of the moduli prior to conducting the 14 fatigue tests and one static ultimate test.

This same analysis was then employed to determine which plies are debonding and when they occur as the applied laminate stress is increased. In attempting to properly model fiber debonding, one can consider the following four first ply failure conditions:

1. Interface failure of ±45° and 90° fibers (fibers become debonded from matrix), but matrix still contributes to stiffness.

2. Interface failure of 90° fibers only, but matrix still contributes to stiffness.

3. Total Discount Theory - interface failure of both ±45° and 90° fibers, i.e. neither the fibers nor the matrices of those plies have a contribution in the [A] matrix.

4. Total Discount Theory - interface failure of only 90°

fibers.

However, the total discount theories (#3 and #4 above) do not represent an accurate model of a debonded laminate because the matrices of debonded plies are still present and thus still add stiffness. Therefore, the matrices should not be totally discounted. The total discount calculations have been included in Appendices A and B for completeness only. Further discussion here will be limited to conditions #1 and #2 above.

According to Appendix B's calculations of the ply and laminate properties at 427°C, when only the fibers in the 90° plies are debonded, the laminate longitudinal stiffness is 107.5 GPa. When the fibers in both the 45° and 90° plies are debonded, the laminate longitudinal stiffness is 65.4 GPa. A comparison to the experimental data can now be made.

As the elevated temperature static ultimate test indicated, there were two points of non-linearity. The first occurred at an applied stress of 140 MPa and the second at an applied stress of 575 MPa. The resulting longitudinal moduli were 116.5 GPa for the first segment (where all fibers in all the plies are believed to be bonded to the matrix, except for the debonds due to the non-perfect manufacturing process), 74.5 GPa for the second segment, and 44.1 GPa for the third segment.

Thus, at the first point of non-linearity, it can be

surmised that all the fibers in the 90° plies and a percentage of the fibers in the 45° plies have become debonded. This agrees with the replica analysis in Chapter IV where debonding of the fibers in the 90° plies was readily seen, but indications of fiber debonding in the 45° plies varied from minor to blatant.

The second point of non-linearity seems to indicate that the fibers in both the 45° and 90° plies have become debonded and the matrix has yielded. This can be said because the laminate stiffness has reduced to only 44.1 GPa which is below the elastic matrix modulus of 52.2 GPa.

B. Fiber and Matrix Micromechanical Stresses.

METCAN, the METal matrix Composite ANalyzer, a FORTRAN language computer program developed by NASA Lewis Research Center, was utilized because of its outstanding ability to determine the localized microstresses of the fiber and matrix in all plies for any loading profile. A typical profile programmed into METCAN included a cooldown phase (from the 1000°C reached during the HIPing process) and two fatigue cycles (both being in-phase, out-of-phase, or isothermal). Stresses are assumed to be zero at the 1000°C temperature; and, residual stresses are assumed to appear when the composite cools down to room temperature. See Figure 42 for a typical graphic representation of the re-

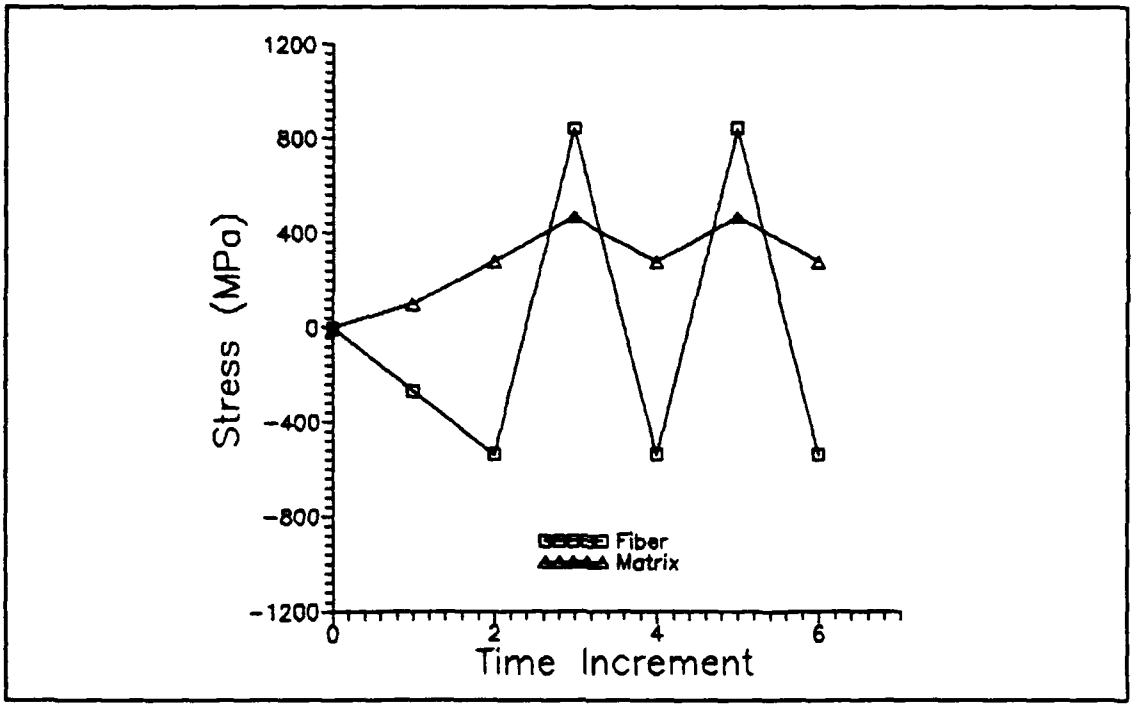

Figure 42. Fiber/Matrix Stresses During First Two Cycles

sulting maximum stresses in both the fiber and matrix of a 0° ply with a maximum applied load of 475 MPa.

Refer to Appendix E for graphs which give the resulting stresses from the in-phase, out-of-phase, and isothermal loading profiles for an applied stress of 100 MPa. Since the analysis is assumed to be linear, one can multiply the results of time increment 2 and onward by the ratio of the true applied stress over the 100 MPa given (i.e. for 475 MPa, multiply the results by 475 ÷ 100 or 4.75) to determine what the stresses would be for any applied stress level. The stresses at time increment 1 are the residual stresses and are independent of the applied load. The mechanical

load begins at time increment 2.

Furthermore, the graphs presented in Appendix E are from two different METCAN versions. The first version uses a THERM2 subroutine while the other ignores it. This subroutine allows METCAN to apply three dimensional effects in calculating the residual stresses (derived from the difference between the coefficients of thermal expansion of the fiber and matrix). When THERM2 is ignored, METCAN reverts to an ordinary strength of materials approach in determining these stresses. When comparing the two different outputs, one can see that, upon removal of THERM2, the fiber stresses appear to be smaller than when the subroutine is incorporated into the analysis. Also, the matrix stresses appear to be larger than with the subroutine. For discussion purposes hereafter, the results from the METCAN output that ignored THERM2 will be used.

The graphs indicate that the 0°, 45°, and 90° plies of the out-of-phase specimens should be seeing a matrix domination. The fractographic results agreed with this conclusion - brittle matrix fatigue failure was evident in the three different plies for both higher and lower maximum applied load levels.

For the IP and IF cycling, the graphs indicate that the 0° plies do not have a clear domination of either matrix or

fiber maximum stresses. On the other hand, both the 45° and 90° plies undergoing these loading profiles do show a definite matrix stress domination. This outcome correlates well with the fractographic results of both the higher stressed and lower stressed specimens. The 0° plies displayed both failure modes - areas of fiber domination with ductile matrix failure (matrix underwent static overload) and areas of matrix domination (matrix contained cleavage cracking implying fatigue failure). The 45° and 90° plies both showed matrix dominated failure.

C. Failure Parametrization.

In attempting to investigate the causes of fatigue failure, one usually searches for a single parameter that will allow the collapse of the measured fatigue data to show just how the material failed or which is the controlling parameter. The parameters used in this numerical analysis include the cycling profiles, the cycles to failure, the maximum and minimum fiber axial stress, the maximum and minimum matrix axial stress, the fiber axial stress range, and the matrix axial stress range. See Table 9 for the maximum and minimum fiber and matrix stress results from METCAN. The maximum and minimum fiber stresses occurred in the 0° plies while the maximum and minimum matrix stresses occurred in the 90° plies.

Table 9. Maximum and Minimum Constituent Stresses

Max Applied Stress (MPa)	Max Fiber Stress (MPa)	Min Fiber Stress (MPa)	Max Matrix Stress (MPa)	Min Matrix Stress (MPa)
In-Phase:				
475	580	-1400	989	795
375	458	-1105	781	627
360	440	-1061	749	602
325	397	-958	677	544
Out-of-Phase:				
475	72	-820	1031	570
425	64	-734	922	510
375	57	-648	814	450
325	49	-561	705	390
310	47	-535	673	372
Isothermal:				
475	559	-821	807	628
450	530	-777	765	595
425	500	-734	722	562
400	471	-691	680	529
375	441	-648	637	496

The fiber and matrix stress ranges for the three profiles are plotted in Figure 43 and 44, respectively, for a maximum applied stress of 100 MPa. The maximum fiber and matrix stresses versus cycles to failure are plotted in Figure 45 and 46, respectively, for the maximum applied stresses used experimentally. The change (maximum minus minimum) in fiber and matrix stresses versus cycles to failure are plotted in Figure 47 and 48, respectively, also for the maximum applied stresses used experimentally.

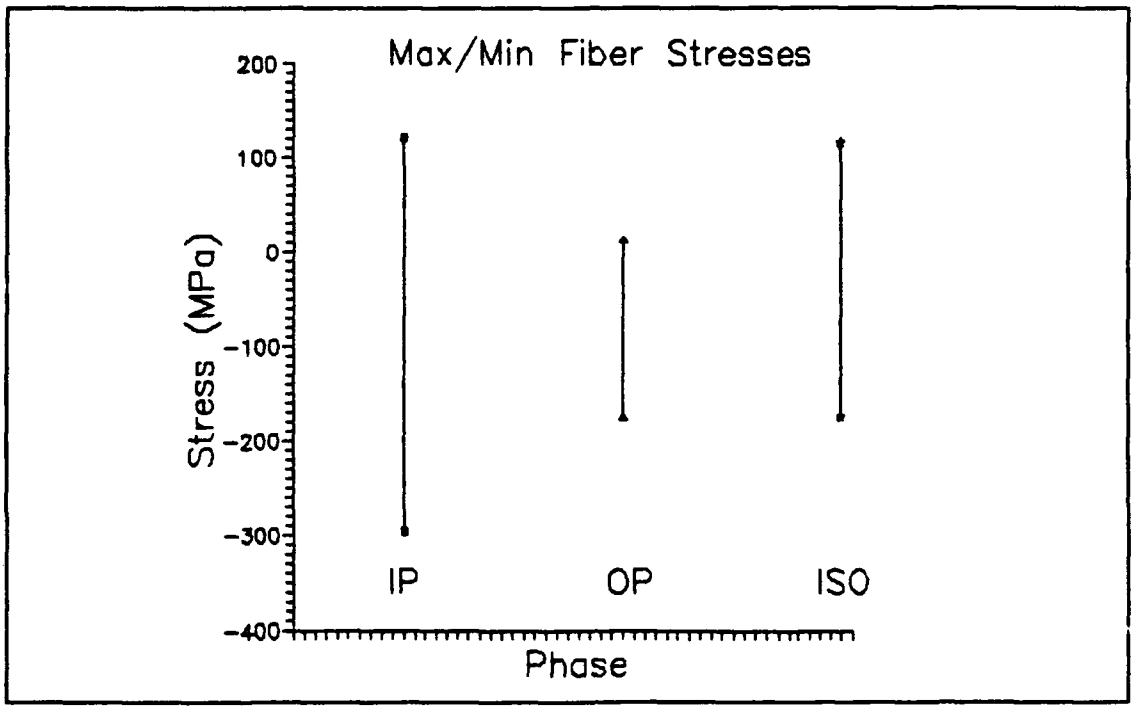

Figure 43. Maximum/Minimum Fiber Stresses, 0° Ply

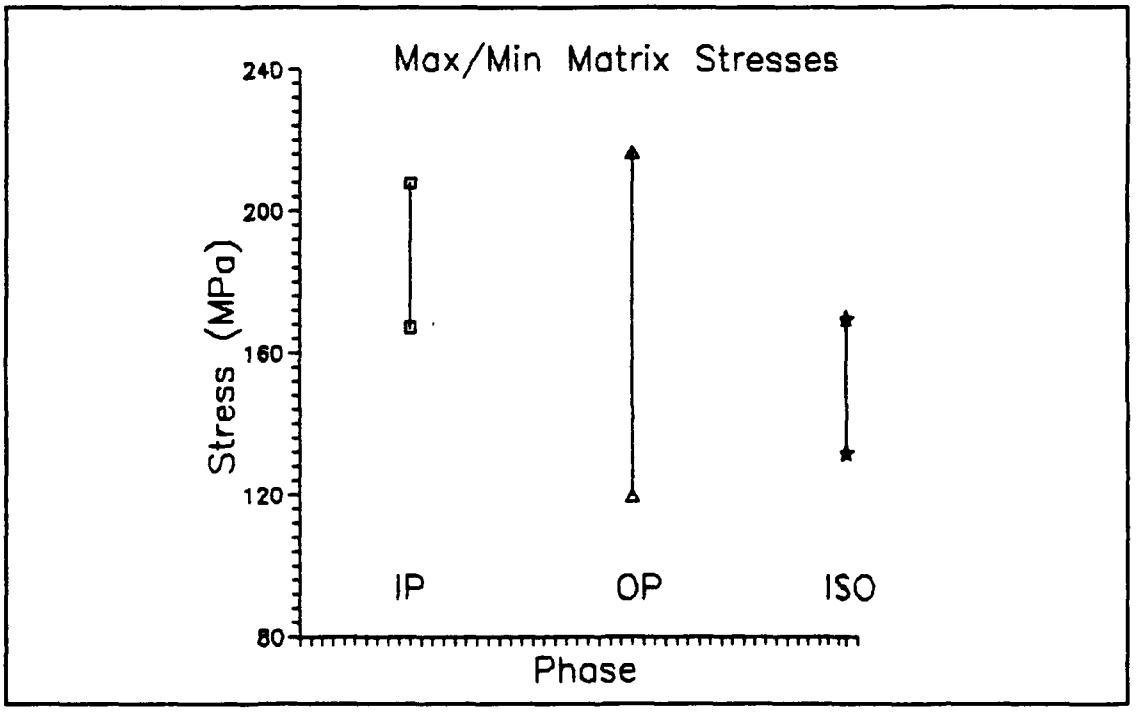

Figure 44. Maximum/Minimum Matrix Stresses, 90° Ply

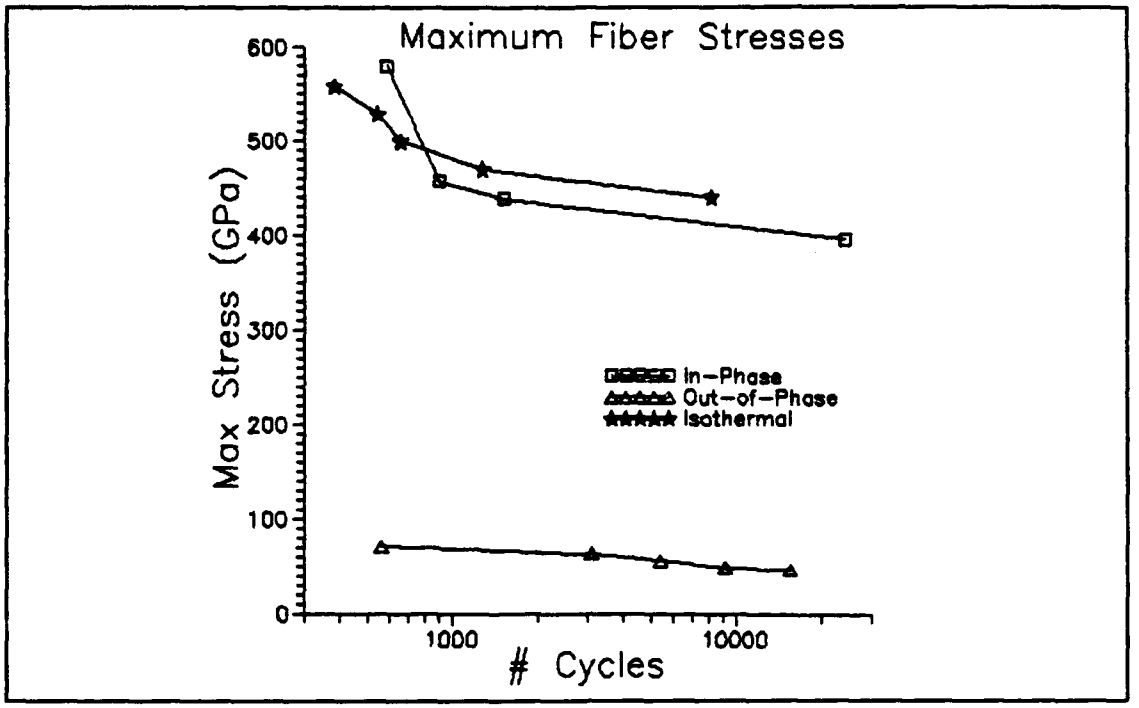

Figure 45. Maximum Fiber Stresses vs. Cycles to Failure

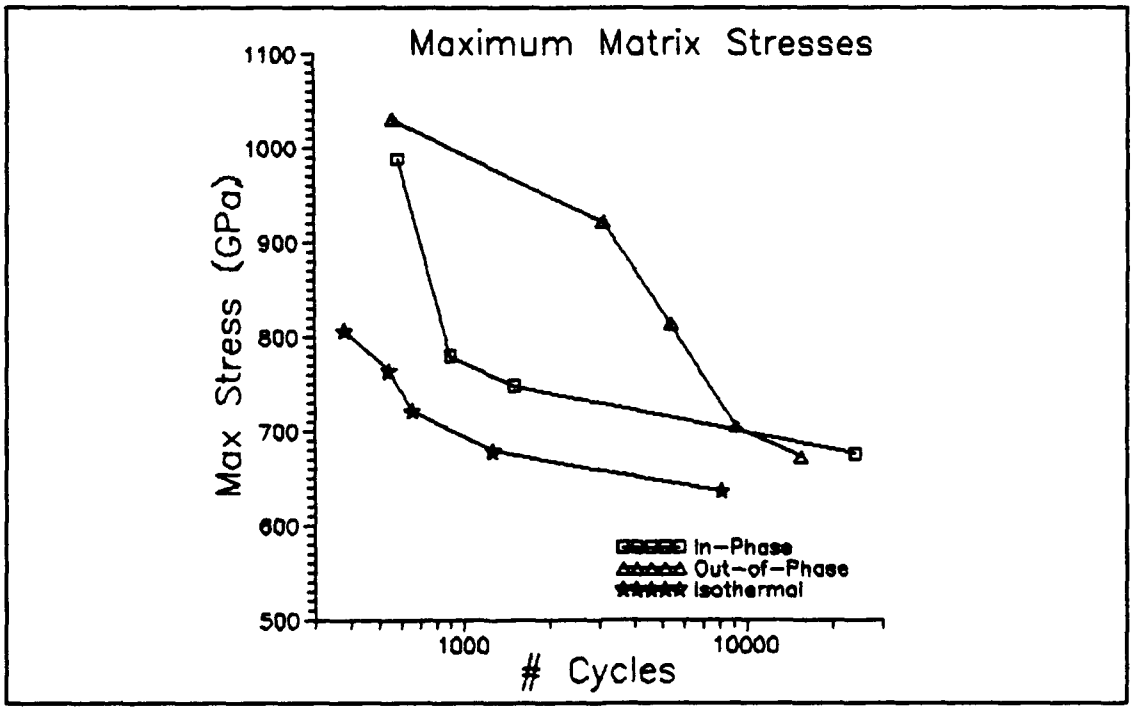

Figure 46. Maximum Matrix Stresses vs. Cycles to Failure

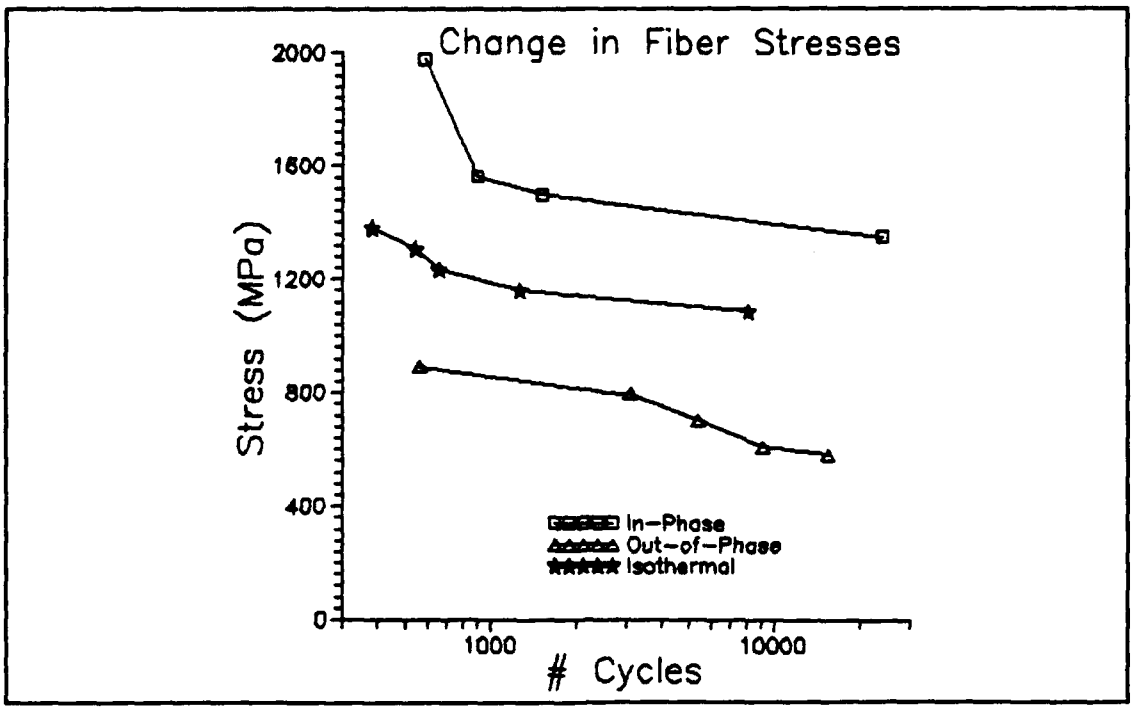

Figure 47. Change in Fiber Stresses vs. Cycles to Failure

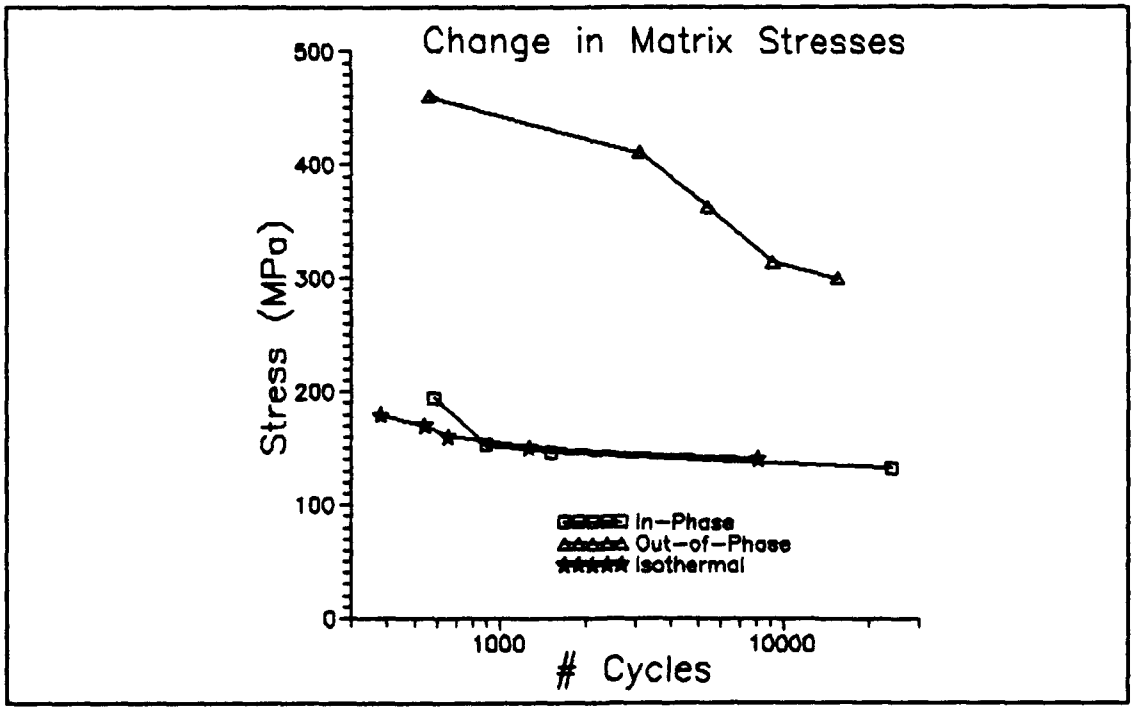

Figure 48. Change in Matrix Stresses vs. Cycles to Failure

The trends from these plots imply that a single parameter cannot be used to collapse all data as a unique predictor of fatigue behavior. This finding is similar to that of Russ et al. during their investigation of SCS-6/Ti-24-11 (22) and that of Mall et al. (15) during their investigation of SCS-6/β21-S. Consequently, they both turned to the Linear Life Fraction Model (LLFM) as described in Chapter II. The LLFM is based on the assumption that the composite's fatigue life is contingent upon two different failure modes: a fiber dominant mode and a matrix dominant mode. The equation for fatigue life is:

$$N = \frac{1}{1/N_f + 1/N_m} \tag{14}$$

where N is cycles to failure of the laminate, N_f is the cycles to failure due only to the fiber dominated mode, and N_m is the cycles to failure due only to the matrix dominated mode. N_f and N_m are as follows:

$$N_f = 10^{\{N_o(1 - \sigma_{max}/\sigma^*)\}} \tag{15}$$

$$N_m = B(\delta\sigma_m)^{-n} \tag{16}$$

N_o, B, and n are empirical constants, σ^* is the maximum fiber stress at tension failure under static load at 427°C as calculated from METCAN, σ_{max} is the maximum axial stress in the 0° fibers for a given maximum applied stress level, and $\delta\sigma_m$ is the axial stress range in the matrix for a given maximum applied stress level. All stresses are in units of MPa.

Mall et al. (15) found better correlation when they modified the N_f equation by substituting $\sigma_{max}(1-R)^m$ for σ_{max} where m is an empirically chosen constant ranging between 0 and 1 and R is the minimum to maximum applied stress ratio.

For this analysis, the best results were found by using the following constants in the model: $N_o = 7.0$, $\sigma^* = 918$ MPa, $B = 10^{19}$, $n = 6.0$, $m = 0.0$. The experimental data from the OP cycling was very well predicted while the IP and isothermal cycling were only fairly well predicted (the predictor curves could not match the large arcs of the IP and IF experimental curves). Also, the modification to the N_f equation used by Mall et al. did not give better correlation for all predictors (for m ranging from 0 to 1). It too could not predict the large arcs of the IP and IF experimental curves. The OP predictor curve was unaffected by the change to the equations. The experimental data and the LLFM's predictions are given in Figure 49.

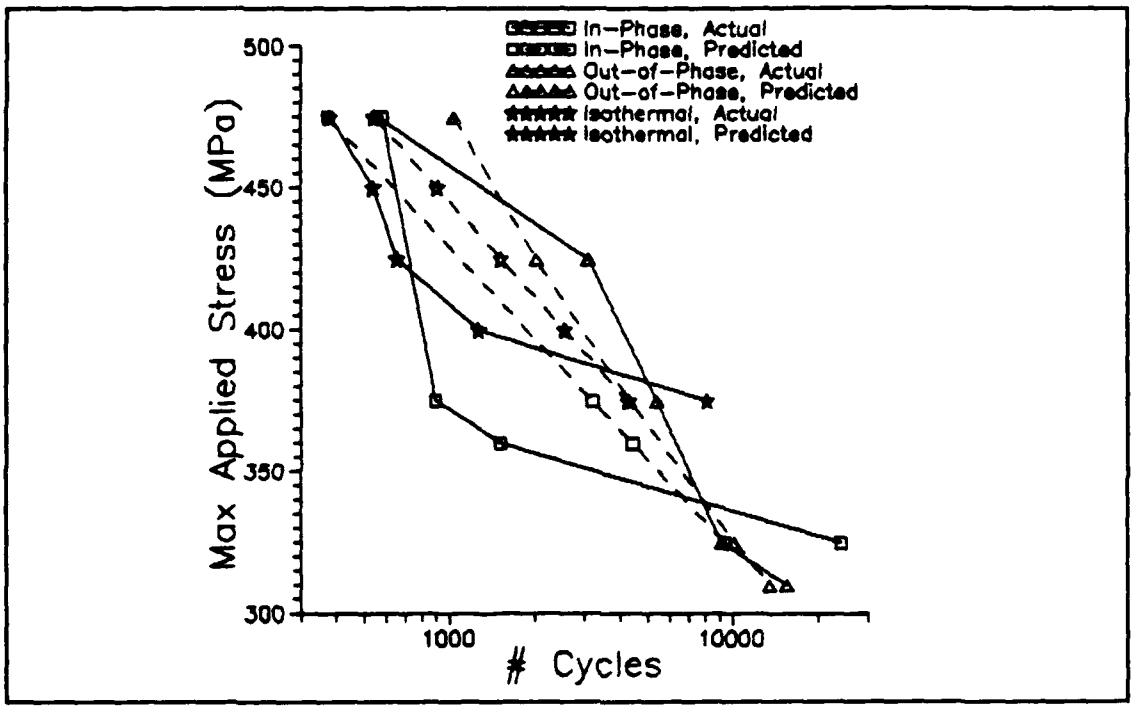

Figure 49. Linear Life Fraction Model Predictions

Another means to determine the correlation of the predicted cycles to failure to the experimental data of cycles to failure is to plot one versus the other as shown in Figure 50. An ideal prediction is exhibited by the straight solid line on the plot.

The very good correlation of the LLFM with the OP experimental data indicates that the OP fatigue failure is strongly matrix dominated. This conclusion agrees well with the METCAN results (fiber and matrix micromechanical stress plots in Appendix E) and the fractographic results. The correlation of the LLFM with the IP and IF experimental data indicates that their failures may be the result of a non-

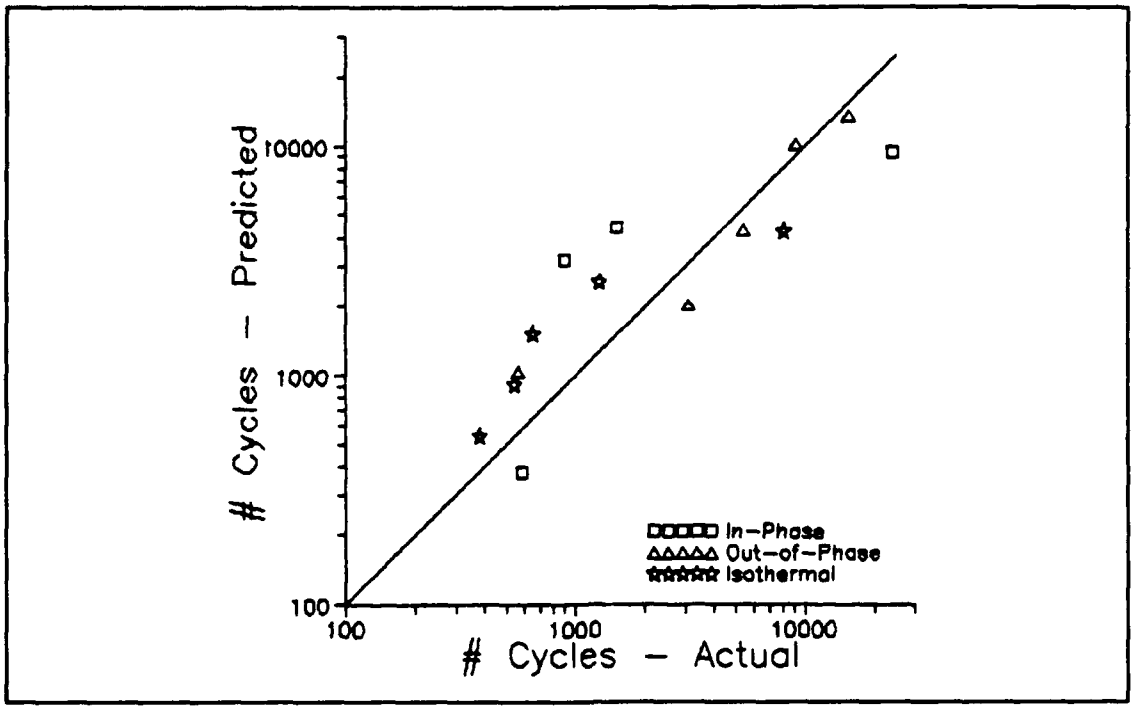

Figure 50. Predicted vs. Actual Cycles to Failure

linear combination of a fiber dominated failure mode and a matrix dominated failure mode.

VI. Conclusions and Recommendations

This investigation discussed in detail the results of a systematic study on the behavior of SCS6/Ti-15-3, quasi-isotropic layup, when subjected to a static load and fatigue cycling. The load, temperature, and strain data were measured by a computer controlled test system as the specimens were subjected to the static load and to the in-phase TMF, out-of-phase TMF, and isothermal fatigue. From this data, the fatigue life curves were established, the mechanical strain response was determined, and the instantaneous modulus was calculated. Additionally, fractography, metallography, and analyses were performed to further define the damage mechanisms and failure modes of the material.

A. Conclusions: The conclusions of this study are summarized as follows:

1) The first point of non-linearity, first ply failure, of the elevated temperature (427°C) static test occurred at 140 MPa. At this point, all of the fibers in the 90° plies are debonded while a percentage of the fibers in the 45° plies are debonded. The second point of non-linearity, the matrix yielding point, occurred at 575 MPa.

2) The cross over point between IP and OP cycling occurred at 340 MPa and 8,000 cycles. Above this stress level, OP cycling produced a longer fatigue life than IP

cycling. Between OP and IF cycling, the cross over was at 385 MPa and 5,000 cycles. Above this stress level, OP cycling also produced a longer fatigue life than IF cycling. For IP and IF cycling, the cross over point was 420 MPa and 750 cycles. Above this stress level, IP cycling produced longer fatigue life than IF cycling. No correlation could be made between the IP/OP cross over point and the second point of non-linearity.

3) The maximum and minimum strain plots of IP and IF cycling indicated a creep ratchetting response - as the strain levels increased, more of the load was being transferred to the 0° fibers until the critical fiber stress was reached. Fiber failure was probably small until near the end of life where their ultimate failure led to a static matrix failure then specimen failure. The instantaneous modulus plots supported this failure mode showing constancy for most of the specimens' lives until near failure.

4) The maximum and minimum strain plots of OP cycling did not indicate this same creep ratchetting response. Rather, they exhibited matrix damage. The instantaneous modulus plots also supported this failure mode with larger decreases occurring early in the specimens' lives.

5) Replica results showed no matrix cracking for high load IP and IF tests and only relatively minor longitudinal

matrix cracking in the lower load IP and IF tests. These cracks may have contributed to specimen failure but probably not to a serious degree. Conversely, the OP tests produced widespread transverse matrix cracking.

6) Fractography results indicated fiber pullout and ductile matrix failure in the IP and IF tests, especially with the higher loaded specimens. On the other hand, the OP cycling produced flatter fracture surfaces, brittle matrix cracking, and little or no fiber pullout, especially with the lower loaded specimens.

Besides the above stated trends distinguishing IP and IF cycling with OP cycling, the trends, for all three profiles, also disclosed a stronger tendency of a fiber dominated failure mode with the higher maximum applied stresses and a stronger tendency of a matrix dominated failure mode with the lower maximum applied stresses.

7) Metallography results exhibited more 0° fiber cracks and little matrix cracking in higher stressed specimens (versus the lower stressed specimens). In contrast, the lower stressed specimens revealed larger scale matrix cracking with less fiber cracking.

8) Investigation through METCAN into the micromechanical fiber and matrix stresses of OP cycling showed a clear matrix domination when comparing the maximum matrix and fiber stresses. However, for IP and IF cycling, METCAN

failed to show a clear domination - its results indicated the maximum matrix and fiber stresses were equivalent.

9) The Linear Life Fraction Model demonstrated a matrix dominated failure mode in OP cycling and a possible non-linear combination of a fiber dominated and a matrix dominated failure in IP and IF cycling.

10) In light of the above stated conclusions, failure is both profile dependent and load dependent.

B. Recommendations:

1) Additional tests should be performed for all three profiles above 475 MPa to determine if fiber domination is even more prevalent in the higher stress levels.

2) Additional tests should be performed for IP cycling below 325 MPa and IF cycling below 375 MPa to determine if matrix domination is more prevalent in their lower stress levels.

3) The possibility of a non-linear life fraction model should be examined to improve the fatigue life prediction capability for IP and IF fatigue cycling.

4) Additional static tests should be performed at ambient conditions and 149°C to improve the understanding of the MMC's static behavior.

APPENDIX A

Ply and Laminate Properties of a Quasi-Isotropic SCS6/Ti-15-3 Composite at Room Temperature (25°C)

Classical laminated plate theory, Halpin-Tsai equations, and basic strength of materials expressions are used to calculate the ply and laminate engineering properties both before and after debonding at ambient temperature. NOTE: Equations are only shown the first time when they are used. The results will be given every time thereafter.

I. CONSTITUENT, PLY, AND LAMINATE DATA:

Matrix Modulus Data (17:15):

T (°C)	E_m (GPa)
25	91.8
316	80.4
482	72.2
566	64.4

Volume Ratios:

$V_f = 0.392$
$V_m = 0.608$

Laminate Thickness = 1.692 mm

Ply Thickness = 0.2115 mm

Fiber Modulus (17:14):

E_f = 400.0 GPa (independent of temperature)

II. ROOM TEMPERATURE MODULI:

A. <u>Moduli for laminate with bonded plies</u>:

1) Constituent Moduli (linear interpolation was used for the matrix using above matrix modulus data):

E_f = 400 GPa
E_m = 91.8 GPa

2) Longitudinal Ply Modulus, first assuming perfect bonding between fiber and matrix, using the Rule of Mixtures:

$$E_1 = E_f V_f + E_m V_m = \underline{212.6 \text{ GPa}}$$

3) Ply Transverse Modulus, also assuming perfect bonding, using the Halpin-Tsai equations:

$$E_2 = E_m * \frac{1+ZETA*\eta*V_f}{1-\eta*V_f} \qquad \eta = \frac{(E_f/E_m) - 1}{(E_f/E_m) + ZETA}$$

ZETA = 2 $\qquad \eta = 0.53$

E2 = 163.7 GPa

According to Table Y of Chapter III, these values for E_1 and E_2 are too high. This is due to the equations assuming perfect bonds. More than likely, the metal matrix composite does not have perfect bonds between the fibers and matrix as received from the manufacturer. This can be accounted for by utilizing a correction factor in determining the modulus of the matrix. A factor called β will be used to allow for non-perfect bonds. This factor was determined empirically equal to 0.664 by trial and error to match theoretical and experimental values. Hereafter, "bonded" will refer to plies which contain some of these fibers with non-perfect bonds, and "debonded" will refer to plies where all fibers are completely debonded.

$$E_m^* = \beta * E_m = 0.664 * 91.8 \text{ GPa} = 61.0 \text{ GPa}$$

E_1 and E_2 are recalculated:

E_1 = 193.9 GPa

E_2 = 123.5 GPa

4) Poisson Ratio, using Rule of Mixtures:

$$v_f = 0.25 \qquad v_m = 0.36$$

$$v_{12} = v_f V_f + v_m V_m = 0.317$$

$$\frac{v_{12}}{E_1} = \frac{v_{21}}{E_2} \quad \Rightarrow \quad v_{21} = \frac{E_2 * v_{12}}{E_1} = 0.24$$

5) Shear Modulus of Bonded Ply:

$$G_i = \frac{E_i}{2*(1 + v_i)}$$

G_f = 160.0 GPa (13:32)
G_m = 22.4 GPa

$$G_{12} = G_m * \frac{1+ZETA*\eta*Vf}{1-\eta*V_f} \qquad \eta = \frac{(G_f/G_m) - 1}{(G_f/G_m) + ZETA}$$

ZETA = 1 $\qquad \eta = 0.75$

G_{12} = 41.3 GPa

6) Laminate Moduli (fibers are bonded in all plies):

Stiffness Matrix:

$$Q_{11} = \frac{E_1}{1-v_{12}*v_{21}} = 207.1 \text{ GPa} \qquad Q_{12} = \frac{v_{12}*E_2}{1-v_{12}*v_{21}} = 41.8 \text{ GPa}$$

$$Q_{22} = \frac{E_2}{1-v_{12}*v_{21}} = 131.9 \text{ GPa} \qquad Q_{66} = G_{12} = 41.3 \text{ GPa}$$

Qbar Matrix:

θ	RADIAN	$\bar{Q}_{11}$	$\bar{Q}_{22}$	$\bar{Q}_{12}$	$\bar{Q}_{66}$	$\bar{Q}_{16}$	$\bar{Q}_{26}$
0	0.0	207.1	131.9	41.8	41.3	0.0	0.0
45	0.785	146.9	146.9	64.4	63.9	18.8	18.8
-45	-0.785	146.9	146.9	64.4	63.9	-18.8	-18.8
90	1.571	131.9	207.1	41.8	41.3	0.0	0.0

$$[A] = \begin{bmatrix} 267.7 & 89.9 & 0.0 \\ 89.9 & 267.7 & 0.0 \\ 0.0 & 0.0 & 88.9 \end{bmatrix}$$

$E_x = \underline{140.4}$ GPa $\quad \nu_{xy} = 0.336$

$G_{xy} = 65.4$ GPa

B. Moduli for debonded plies: (this is for reference only, actual debonding occurred at elevated temperature). Note: It is assumed that both E_f and ν_m are equal to 0 for a debonded ply.

1) Constituent Moduli:

$E_f =$ 0 GPa

$E_m^* =$ 61.0 GPa

2) Longitudinal Modulus for Debonded Ply:

$E_1 = \underline{37.1}$ GPa

3) Transverse Modulus for Debonded Ply:

ZETA = 2

$\eta =$ -0.50

$E_2 = \underline{31.0}$ GPa

4) Poisson Ratio:

$\nu_f = 0 \quad \nu_m = 0.36$

$\nu_{12} = 0.219 \quad \nu_{21} = 0.183$

5) Shear Modulus for Debonded Ply:

G_f = 0.0 GPa
G_m = 22.4 GPa

ZETA = 1
η = -1.00

G_{12} = 9.8 GPa

C. Moduli for laminate with failed plies (this is for reference only, actual debonding occurred at elevated temperature). Four possibilities exist:

1) Interface failure of ±45° and 90° fibers (fibers become debonded from matrix), but these plies' matrices still contribute to stiffness.

Stiffness Matrix of Debonded Plies:

Q_{11} = 38.6 GPa

Q_{22} = 32.3 GPa

Q_{12} = 7.1 GPa

$Q_{66} = G_{12}$ = 9.8 GPa

Qbar Matrix (0° plies are still bonded, all others are debonded):

θ	RADIAN	$\bar{Q}_{11}$	$\bar{Q}_{22}$	$\bar{Q}_{12}$	$\bar{Q}_{66}$	$\bar{Q}_{16}$	$\bar{Q}_{26}$
0	0.000	207.1	131.9	41.8	41.3	0.0	0.0
45	0.785	31.1	31.1	11.5	14.2	1.6	1.6
-45	-0.785	31.1	31.1	11.5	14.2	-1.6	-1.6
90	1.571	32.3	38.6	7.1	9.8	0.0	0.0

$$[A] = \begin{bmatrix} 127.6 & 30.4 & 0.0 \\ 30.4 & 98.4 & 0.0 \\ 0.0 & 0.0 & 33.6 \end{bmatrix}$$

$E_x = 69.9$ GPa $\qquad \nu_{xy} = 0.309$

$G_{xy} = 19.9$ GPa

2) Interface failure of 90° fibers only, but its matrix still contributes to stiffness.

Qbar Matrix (0° and ±45° plies are still bonded, 90° plies are debonded):

θ	RADIAN	$\bar{Q}_{11}$	$\bar{Q}_{22}$	$\bar{Q}_{12}$	$\bar{Q}_{66}$	$\bar{Q}_{16}$	$\bar{Q}_{26}$
0	0.000	207.1	131.9	41.8	41.3	0.0	0.0
45	0.785	146.9	146.9	64.4	64.4	18.8	18.8
-45	-0.785	146.9	146.9	64.4	64.4	-18.8	-18.8
90	1.571	32.3	38.6	7.1	9.8	0.0	0.0

$$[A] = \begin{bmatrix} 225.6 & 75.2 & 0.0 \\ 75.2 & 196.4 & 0.0 \\ 0.0 & 0.0 & 75.6 \end{bmatrix}$$

$E_x = 116.3$ GPa $\qquad \nu_{xy} = 0.383$

$G_{xy} = 44.7$ GPa

For completeness, the following Total Discount Theories are included, even though they do not represent an accurate model of a debonded laminate. The matrices of debonded plies still add stiffness and therefore should not be totally discounted.

3) Total Discount Theory - interface failure of both ±45° and 90° plies, i.e. the fibers and matrices of these plies have no contribution to the [A] matrix:

$$[A] = \begin{bmatrix} 87.6 & 17.7 & 0.0 \\ 17.7 & 55.8 & 0.0 \\ 0.0 & 0.0 & 17.4 \end{bmatrix}$$

$E_x = 48.5$ GPa $\qquad \nu_{xy} = 0.317$

$G_{xy} = 10.3$ GPa

4) Total Discount Theory - interface failure of only 90° plies:

$$[A] = \begin{bmatrix} 211.9 & 72.2 & 0.0 \\ 72.2 & 211.9 & 0.0 \\ 0.0 & 0.0 & 71.5 \end{bmatrix}$$

$E_x = 110.7$ GPa $\qquad \nu_{xy} = 0.341$

$G_{xy} = 42.2$ GPa

APPENDIX B

Ply and Laminate Properties of a Quasi-Isotropic SCS6/Ti-15-3 Composite at Elevated Temperature (427°C)

Classical laminated plate theory, Halpin-Tsai equations, and basic strength of materials expressions are used to calculate the ply and laminate engineering properties both before and after debonding at elevated temperature. NOTE: Equations are only shown the first time when they are used. The results will be given every time thereafter.

I. CONSTITUENT, PLY, AND LAMINATE DATA:

Matrix Modulus Data (17:15):

T (°C)	E_m
25	91.8
316	80.4
482	72.2
566	64.4

Volume Ratios:

V_f = 0.392
V_m = 0.608

Laminate Thickness = 1.692 mm

Ply Thickness = 0.2115 mm

Fiber Modulus (17:14):

E_f = 400.0 GPa (independent of temperature)

II. ELEVATED TEMPERATURE (427°C) MODULI:

A. <u>Moduli for laminate with bonded plies</u>:

1) Constituent Moduli (linear interpolation was used for the matrix using above matrix modulus data):

E_f = 400 GPa
E_m = 74.9 GPa

2) Longitudinal Ply Modulus, first assuming perfect bonding between fiber and matrix, using the Rule of Mixtures:

$$E_1 = E_f V_f + E_m V_m = \underline{202.3 \text{ GPa}}$$

3) Ply Transverse Modulus, also assuming perfect bonding, using the Halpin-Tsai equations:

$$E_2 = E_m * \frac{1+ZETA*\eta*V_f}{1-\eta*V_f} \qquad \eta = \frac{(E_f/E_m) - 1}{(E_f/E_m) + ZETA}$$

ZETA = 2 $\qquad \eta = 0.59$

E2 = 142.7 GPa

According to Table Y of Chapter III, these values for E_1 and E_2 are too high for the same reasons stated in Appendix A. Again, this can be accounted for by utilizing a correction factor in determining the modulus of the matrix. A high temperature debond factor called τ will be used equal to 0.697 to allow for non-perfect bonds. Hereafter, "bonded" will refer to plies which contain some of these fibers with non-perfect bonds, and "debonded" will refer to plies where all fibers are completely debonded.

$$E_m^* = \tau * E_m = 0.697 * 74.9 \text{ GPa} = 52.2 \text{ GPa}$$

E_1 and E_2 are recalculated:

$E_1 = 188.5$ GPa

$E_2 = 110.2$ GPa

4) Poisson Ratio, using Rule of Mixtures:

$$v_f = 0.25 \qquad v_m = 0.36$$

$$v_{12} = v_f V_f + v_m V_m = 0.317$$

$$\frac{v_{12}}{E_1} = \frac{v_{21}}{E_2} \quad \Rightarrow \quad v_{21} = \frac{E_2 * v_{12}}{E_1} = 0.19$$

5) Shear Modulus of Bonded Ply:

$$G_i = \frac{E_i}{2*(1 + v_i)}$$

G_f = 160.0 GPa (13:32)
G_m = 19.2 GPa

$$G_{12} = G_m * \frac{1+ZETA*\eta*Vf}{1-\eta*V_f} \qquad \eta = \frac{(G_f/G_m) - 1}{(G_f/G_m) + ZETA}$$

ZETA = 1 $\qquad \eta = 0.79$

G_{12} = 36.3 GPa

6) Laminate Moduli (fibers are bonded in all plies):

Stiffness Matrix:

$$Q_{11} = \frac{E_1}{1-v_{12}*v_{21}} = 200.3 \text{ GPa} \qquad Q_{12} = \frac{v_{12}*E_2}{1-v_{12}*v_{21}} = 37.1 \text{ GPa}$$

$$Q_{22} = \frac{E_2}{1-v_{12}*v_{21}} = 117.1 \text{ GPa} \qquad Q_{66} = G_{12} = 36.3 \text{ GPa}$$

Qbar Matrix:

θ	RADIAN	$\bar{Q}_{11}$	$\bar{Q}_{22}$	$\bar{Q}_{12}$	$\bar{Q}_{66}$	$\bar{Q}_{16}$	$\bar{Q}_{26}$
0	0.0	200.3	117.1	37.1	36.3	0.0	0.0
45	0.785	134.2	134.2	61.6	60.8	20.8	20.8
-45	-0.785	134.2	134.2	61.6	60.8	-20.8	-20.8
90	1.571	117.1	200.3	37.1	36.3	0.0	0.0

$$[A] = \begin{bmatrix} 247.8 & 83.5 & 0.0 \\ 83.5 & 247.8 & 0.0 \\ 0.0 & 0.0 & 82.1 \end{bmatrix}$$

$E_x = 129.8$ GPa $\quad \nu_{xy} = 0.337$

$G_{xy} = 48.5$ GPa

B. Moduli for debonded plies: Note: It is assumed that both E_f and ν_m are equal to 0 for a debonded ply.

1) Constituent Moduli:

$E_f = 0$ GPa

$E_m^* = 52.2$ GPa

2) Debonded Ply Longitudinal Modulus:

$E_1 = 31.7$ GPa

3) Transverse Modulus for Debonded Ply:

ZETA = 2

$\eta = -0.50$

$E_2 = 26.5$ GPa

4) Poisson Ratio:

$\nu_f = 0 \quad \nu_m = 0.36$

$\nu_{12} = 0.219 \quad \nu_{21} = 0.183$

5) Shear Modulus for Debonded Ply:

G_f = 0.0 GPa
G_m = 19.2 GPa

ZETA = 1
ν = -1.00

G_{12} = 8.4 GPa

C. Moduli for laminate with failed plies (this is for reference only, actual debonding occurred at elevated temperature). Four possibilities exist:

1) Interface failure of ±45° and 90° fibers (fibers become debonded from matrix), but these plies' matrices still contribute to stiffness.

Stiffness Matrix of Debonded Plies:

Q_{11} = 33.1 GPa

Q_{22} = 27.6 GPa

Q_{12} = 6.1 GPa

$Q_{66} = G_{12}$ = 8.4 GPa

Qbar Matrix (0° plies are still bonded, all others are debonded):

θ	RADIAN	$\bar{Q}_{11}$	$\bar{Q}_{22}$	$\bar{Q}_{12}$	$\bar{Q}_{66}$	$\bar{Q}_{16}$	$\bar{Q}_{26}$
0	0.000	200.3	117.1	37.1	36.3	0.0	0.0
45	0.785	26.6	26.6	9.8	12.2	1.4	1.4
-45	-0.785	26.6	26.6	9.8	12.2	-1.4	-1.4
90	1.571	27.6	33.1	6.1	8.4	0.0	0.0

$$[A] = \begin{bmatrix} 118.9 & 26.6 & 0.0 \\ 26.6 & 86.0 & 0.0 \\ 0.0 & 0.0 & 29.2 \end{bmatrix}$$

$E_x = 65.4$ GPa $\qquad \nu_{xy} = 0.309$

$G_{xy} = 17.2$ GPa

2) Interface failure of 90° fibers only, but its matrix still contributes to stiffness.

Qbar Matrix (0° and ±45° plies are still bonded, 90° plies are debonded):

θ	RADIAN	$\bar{Q}_{11}$	$\bar{Q}_{22}$	$\bar{Q}_{12}$	$\bar{Q}_{66}$	$\bar{Q}_{16}$	$\bar{Q}_{26}$
0	0.000	200.3	117.1	37.1	36.3	0.0	0.0
45	0.785	134.2	134.2	61.6	60.8	20.8	20.8
-45	-0.785	134.2	134.2	61.6	60.8	-20.8	-20.8
90	1.571	27.6	33.1	6.1	8.4	0.0	0.0

$$[A] = \begin{bmatrix} 209.9 & 70.4 & 0.0 \\ 70.4 & 177.0 & 0.0 \\ 0.0 & 0.0 & 70.3 \end{bmatrix}$$

$E_x = 107.5$ GPa $\qquad \nu_{xy} = 0.398$

$G_{xy} = 41.6$ GPa

For completeness, the following Total Discount Theories are included, even though they do not represent an accurate model of a debonded laminate. The matrices of debonded plies still add stiffness and therefore should not be totally discounted.

3) Total Discount Theory – interface failure of both ±45° and 90° plies, i.e. the fibers and matrices of these plies have no contribution to the [A] matrix:

$$[A] = \begin{bmatrix} 84.7 & 15.7 & 0.0 \\ 15.7 & 49.5 & 0.0 \\ 0.0 & 0.0 & 15.3 \end{bmatrix}$$

$E_x = 47.1$ GPa $\qquad \nu_{xy} = 0.317$

$G_{xy} = 9.1$ GPa

4) Total Discount Theory – interface failure of only 90° plies:

$$[A] = \begin{bmatrix} 198.2 & 67.8 & 0.0 \\ 67.8 & 198.2 & 0.0 \\ 0.0 & 0.0 & 66.8 \end{bmatrix}$$

$E_x = 103.4$ GPa $\qquad \nu_{xy} = 0.342$

$G_{xy} = 39.5$ GPa

APPENDIX C

Strain Hysteresis Loops

The figures of this appendix show the progression of the mechanical strain hysteresis loops for a few fatigue tests. The cycle numbers that correspond to each loop are as follows:

a. IP test, 475 MPa: cycles 1, 148, and 581.

b. IP test, 325 MPa: cycles 1, 12026, and 24121.

c. OP test, 475 MPa: cycles 1, 50, and 563.

d. OP test, 325 MPa: cycles 1, 2511, 5003, and 9169.

e. IF test, 475 MPa: cycles 1, 201, 374.

f. IF test, 375 MPa: cycles 1, 4190, 8094.

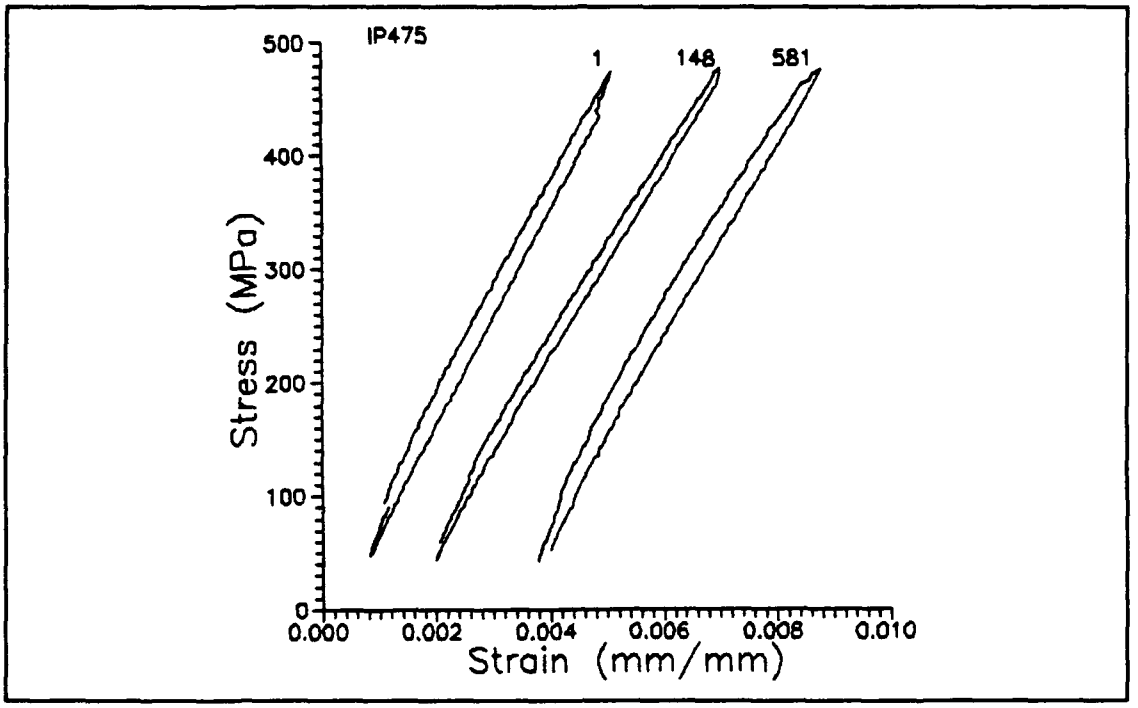

Figure 51. Sample Stress-Strain Data for 475 MPa IP Test

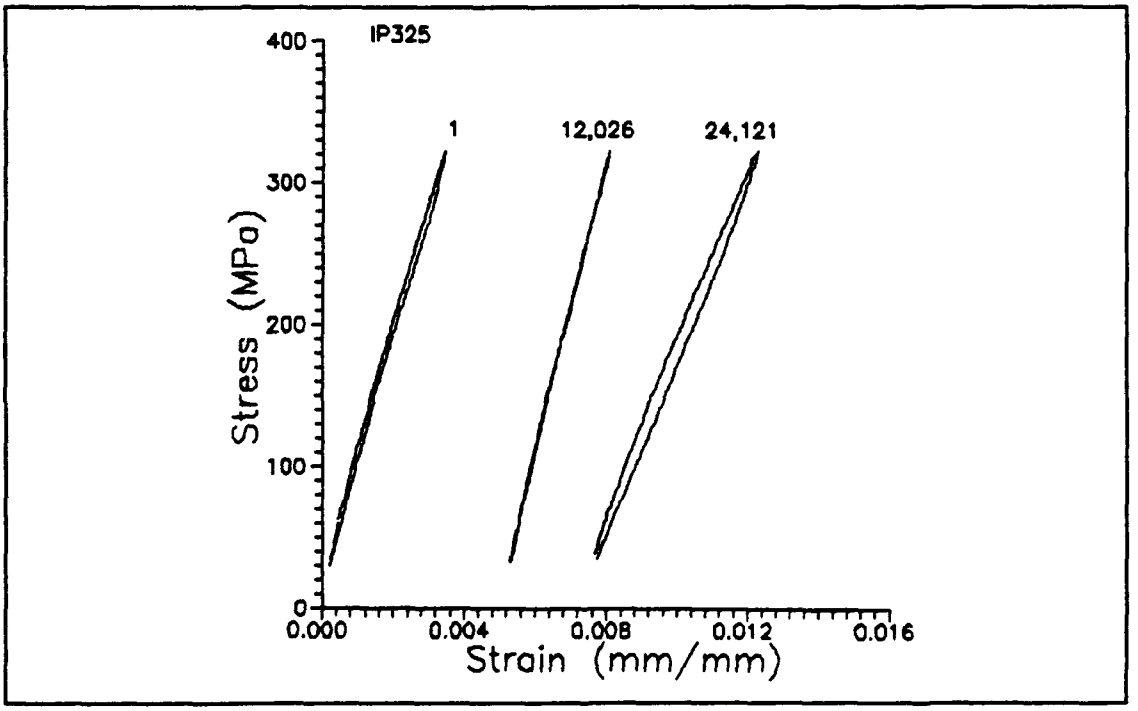

Figure 52. Sample Stress-Strain Data for 325 MPa IP Test

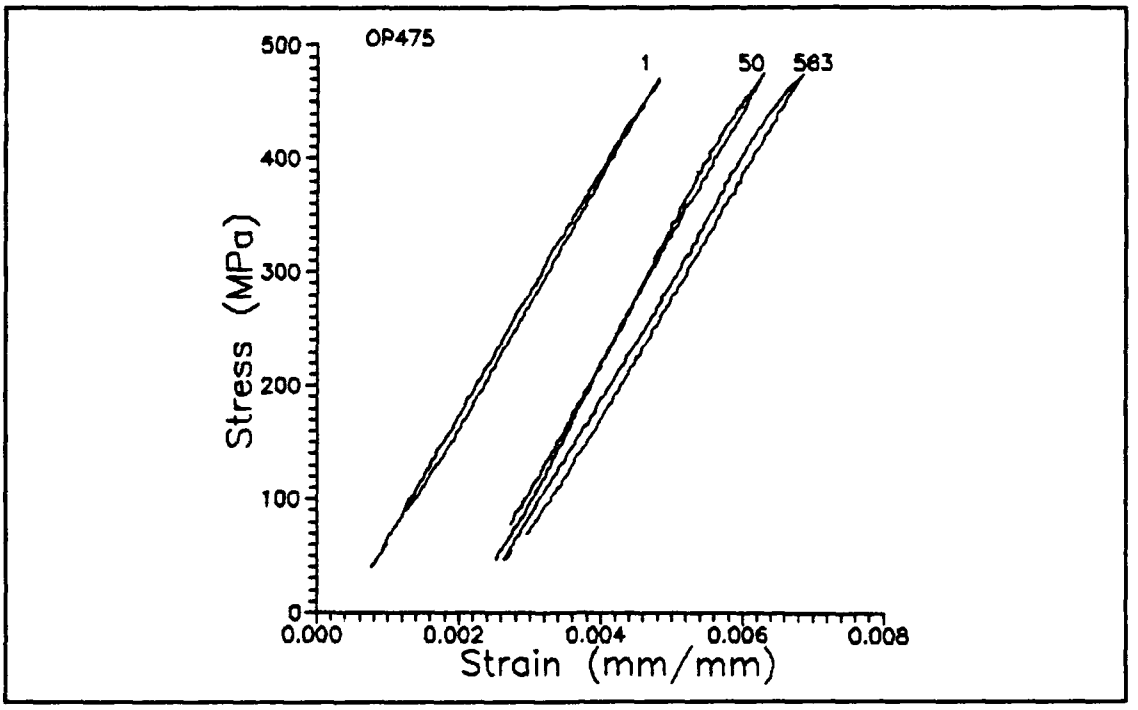

Figure 53. Sample Stress-Strain Data for 475 MPa OP Test

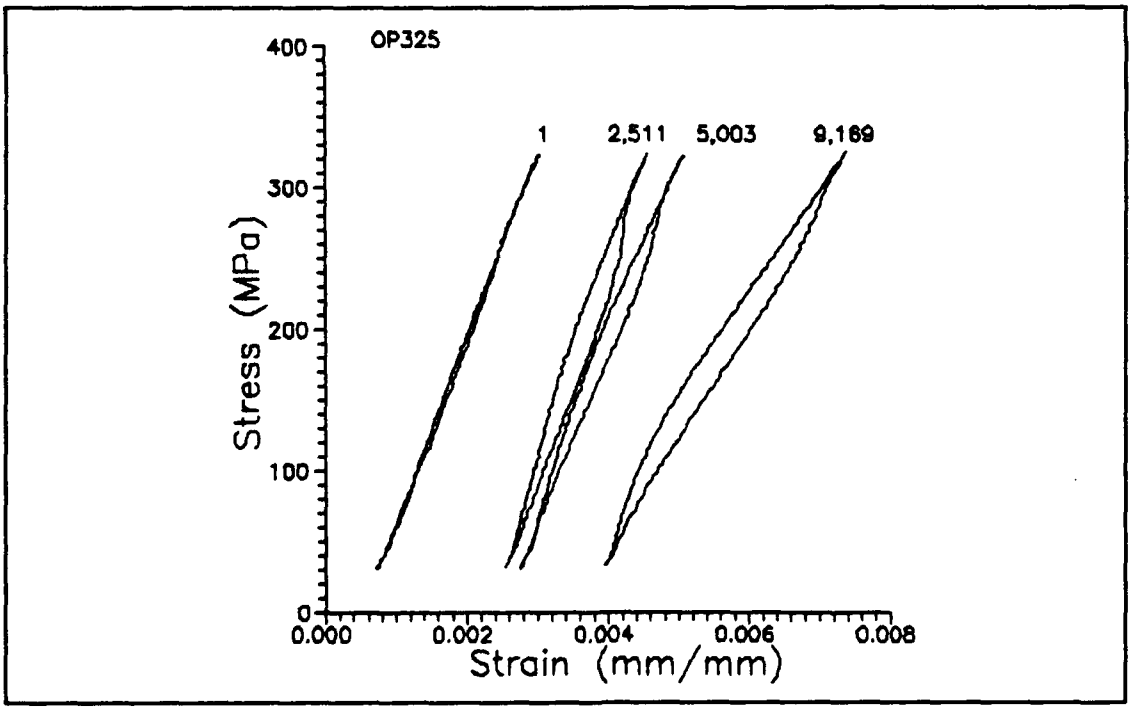

Figure 54. Sample Stress-Strain Data for 325 MPa OP Test

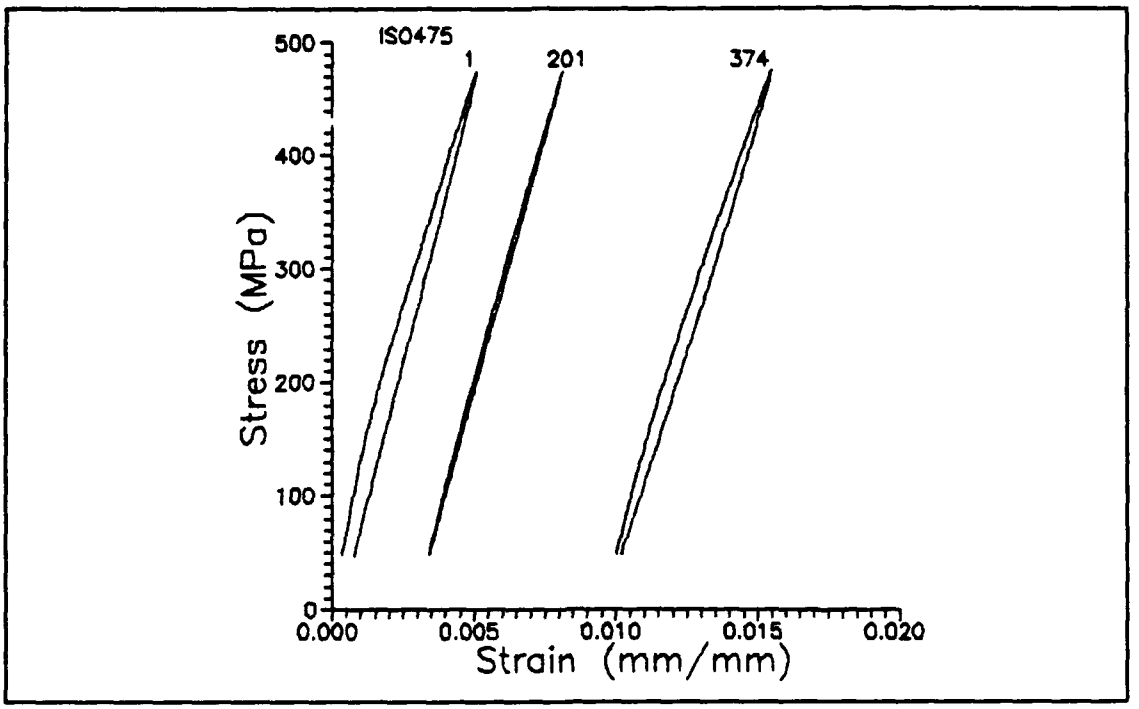

Figure 55. Sample Stress-Strain Data for 475 MPa IF Test

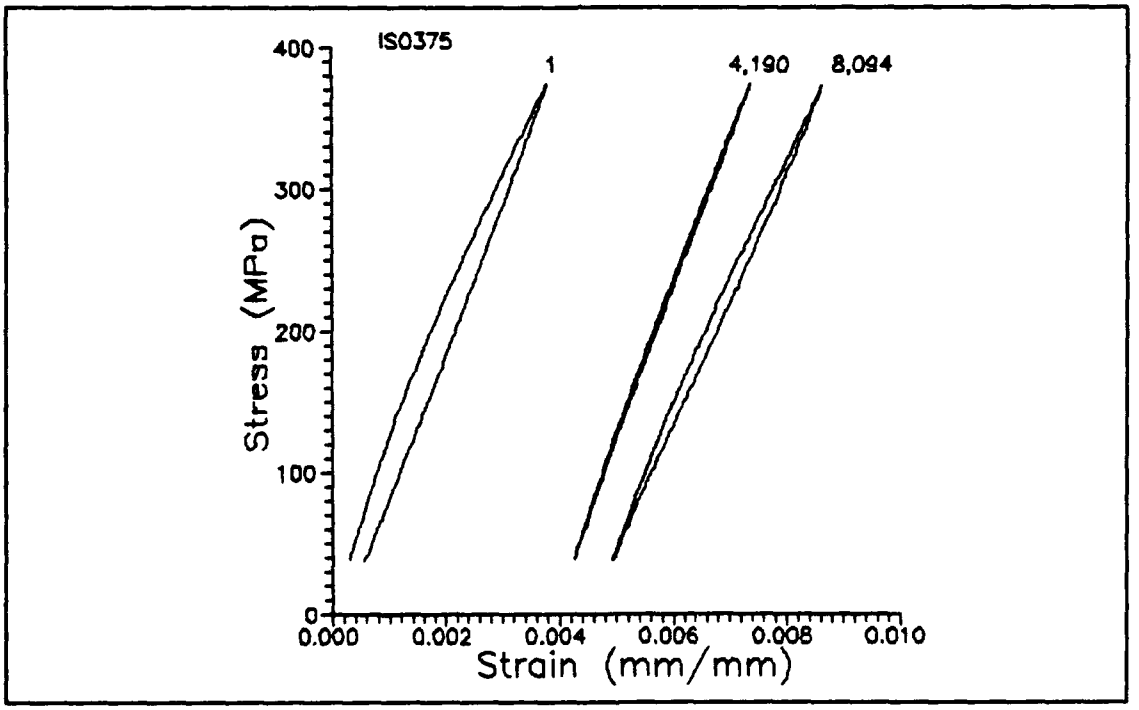

Figure 56. Sample Stress-Strain Data for 375 MPa IF Test

APPENDIX D

Mechanical Strain Data

The figures of this appendix show the progression of the mechanical strain versus specimen life for the fatigue tests not shown in Chapter IV.

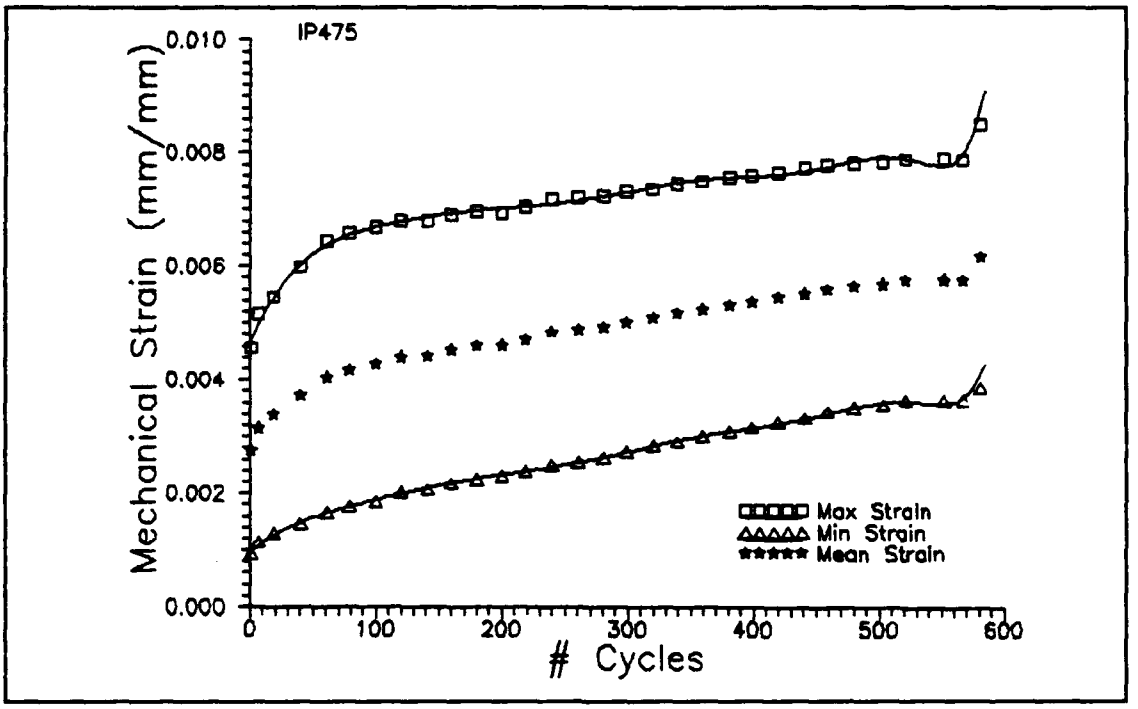

Figure 57. Mechanical Strain Data for 475 MPa IP Test

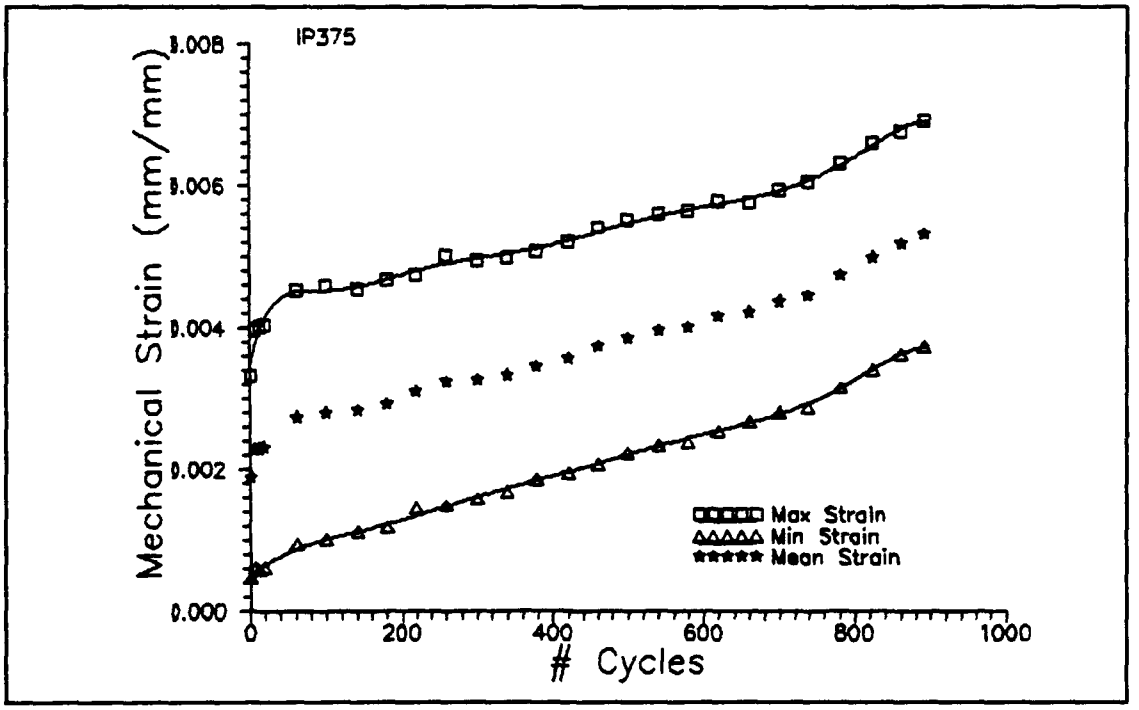

Figure 58. Mechanical Strain Data for 375 MPa IP Test

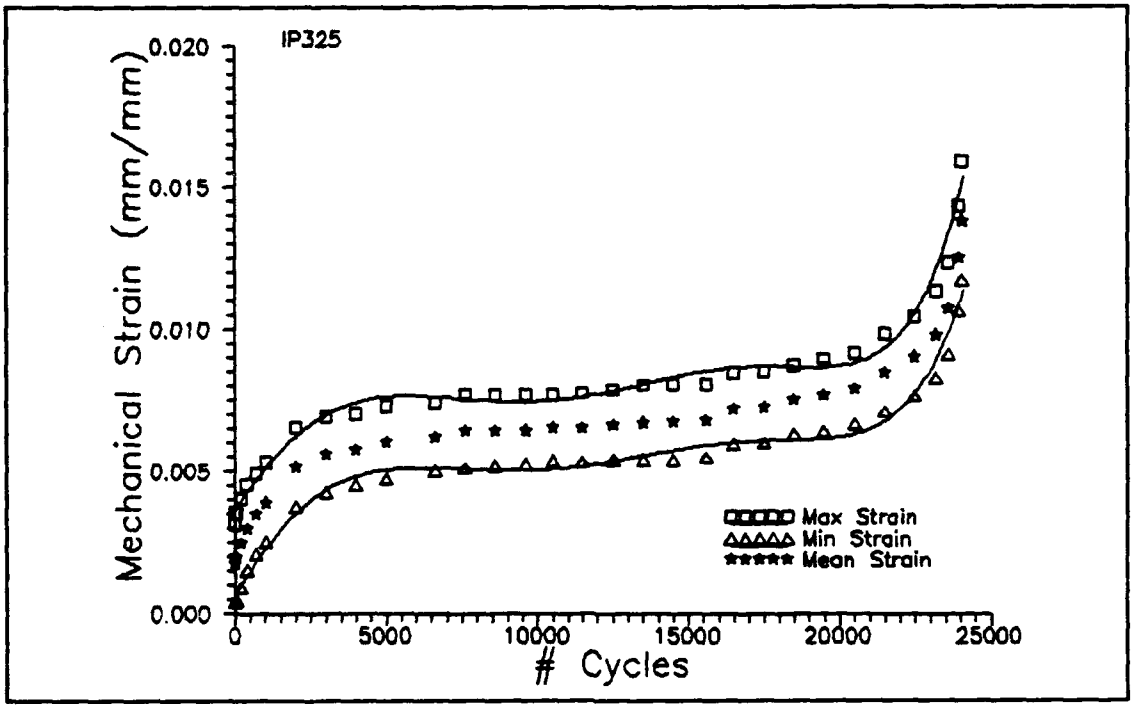

Figure 59. Mechanical Strain Data for 325 MPa IP Test

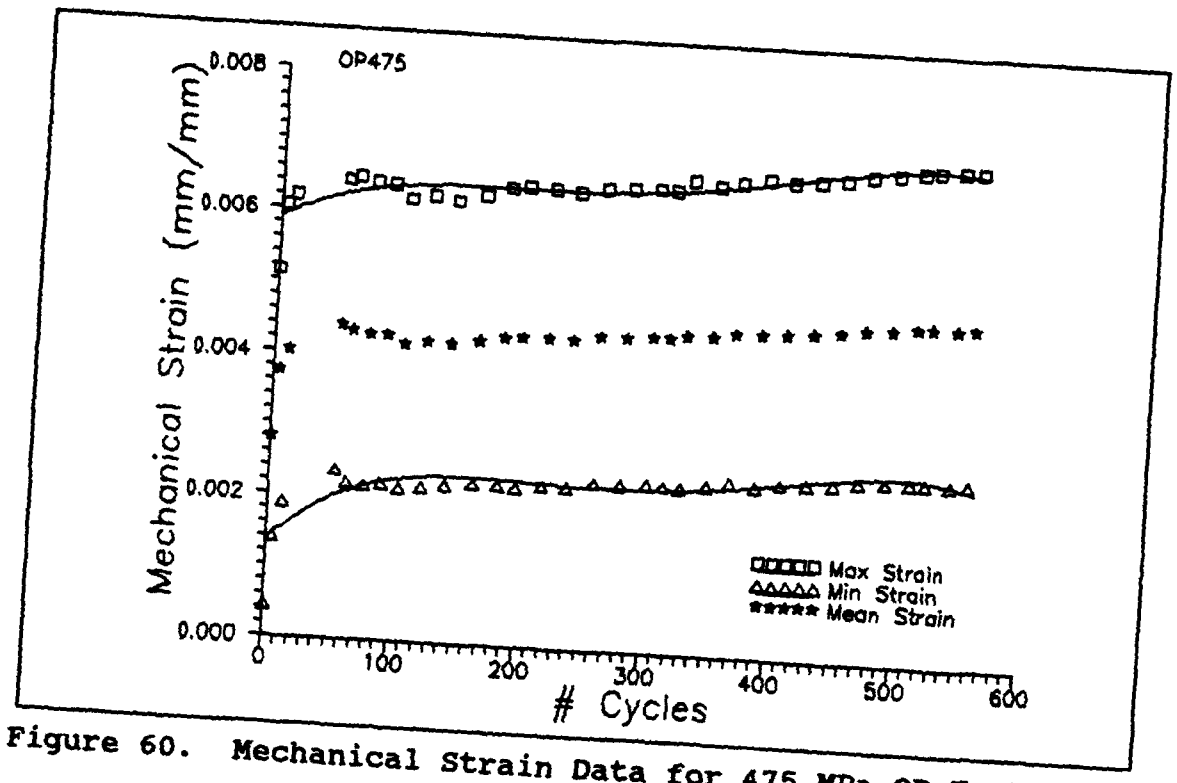

Figure 60. Mechanical Strain Data for 475 MPa OP Test

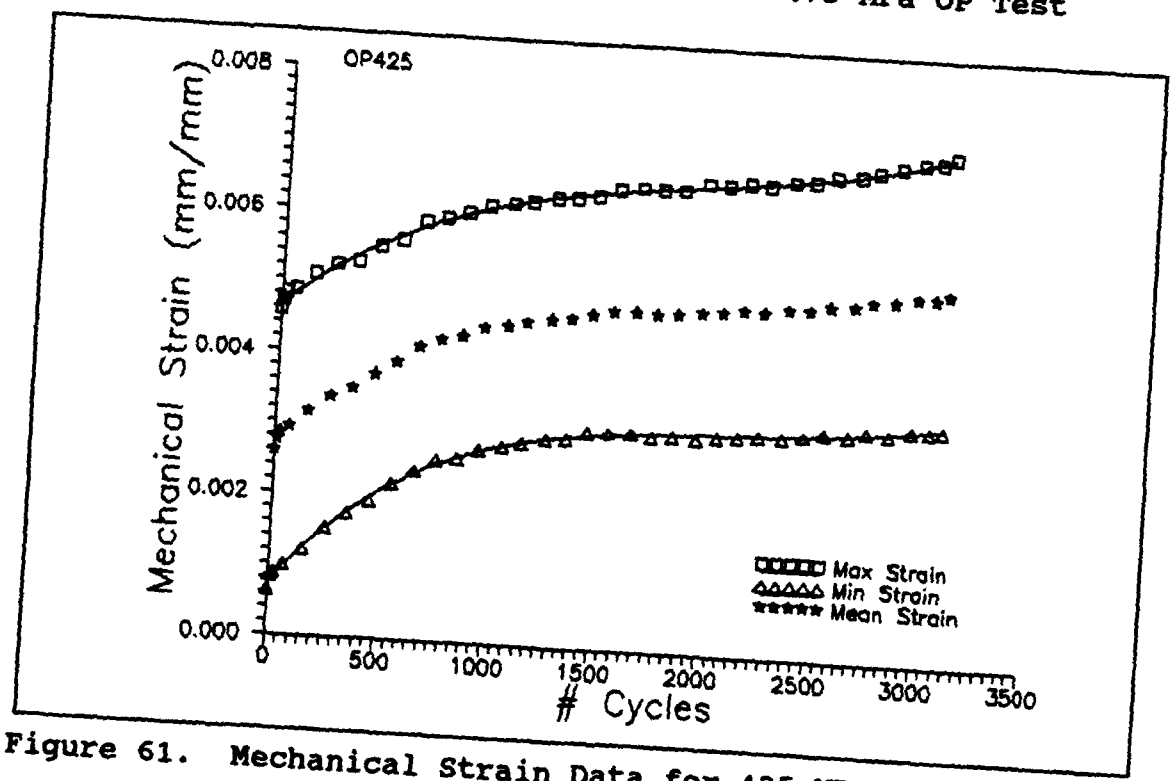

Figure 61. Mechanical Strain Data for 425 MPa OP Test

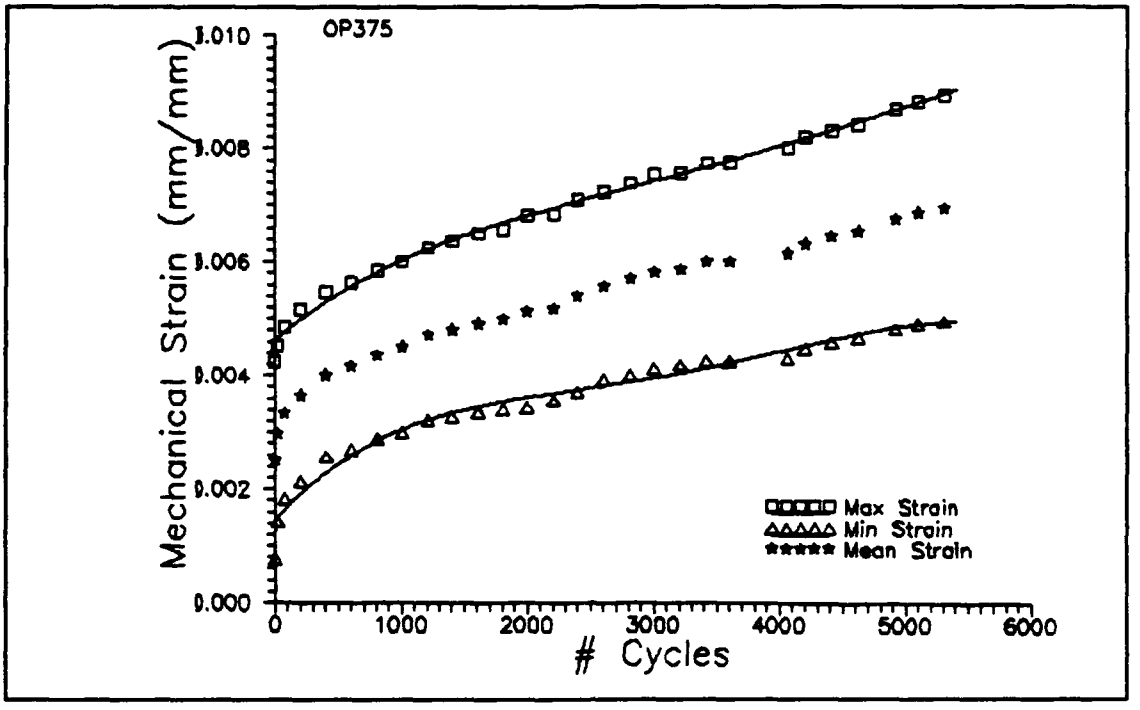

Figure 62. Mechanical Strain Data for 375 MPa OP Test

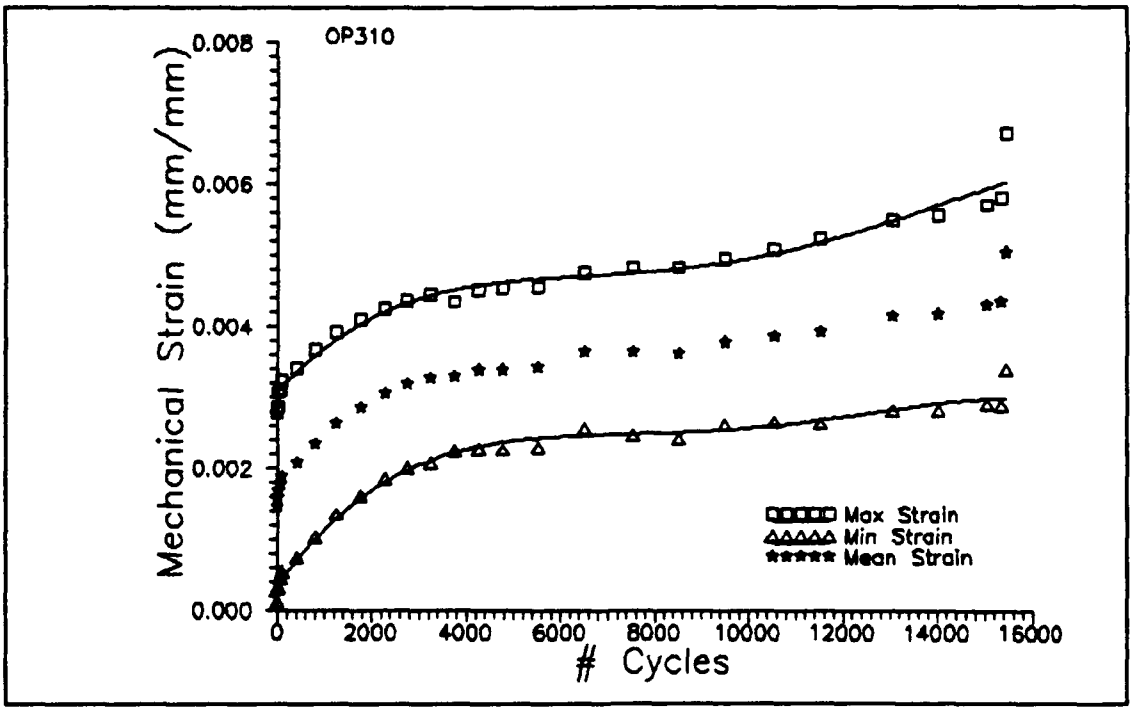

Figure 63. Mechanical Strain Data for 310 MPa OP Test

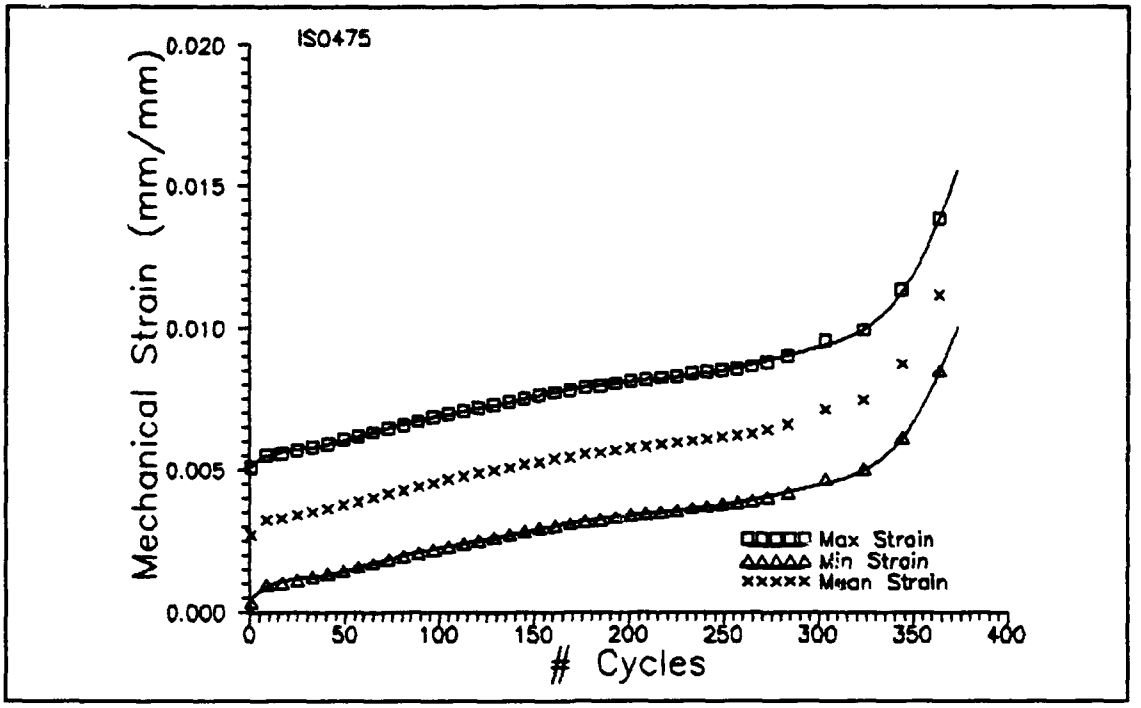

Figure 64. Mechanical Strain Data for 475 MPa IF Test

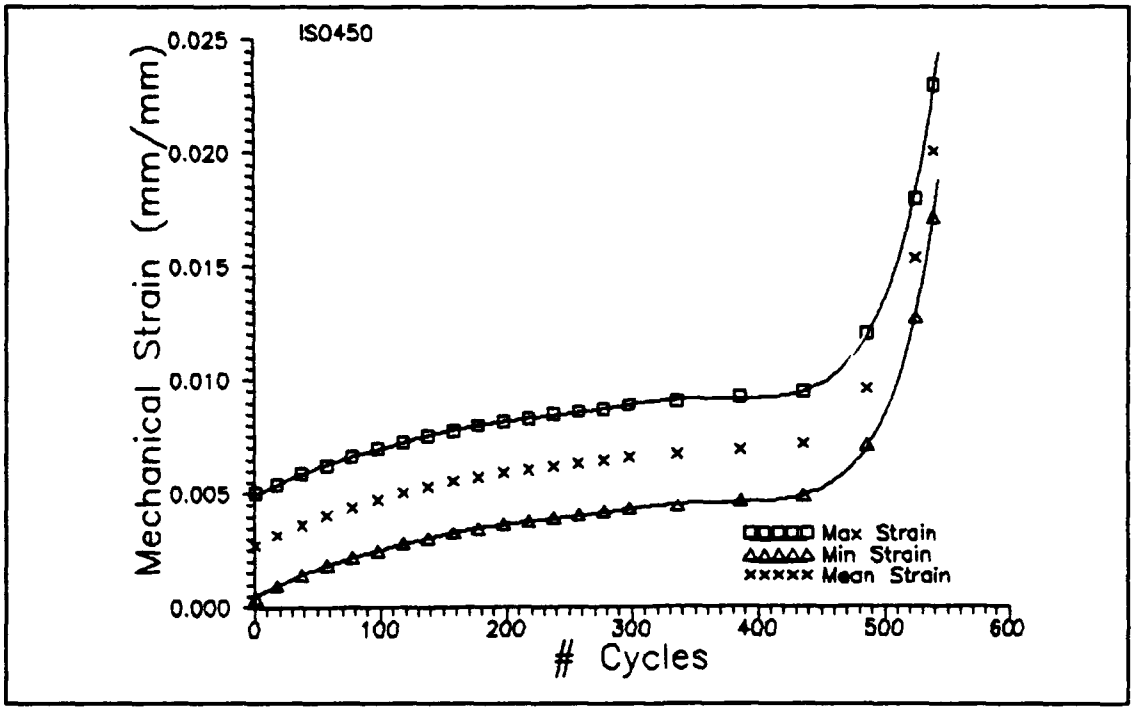

Figure 65. Mechanical Strain Data for 450 MPa IF Test

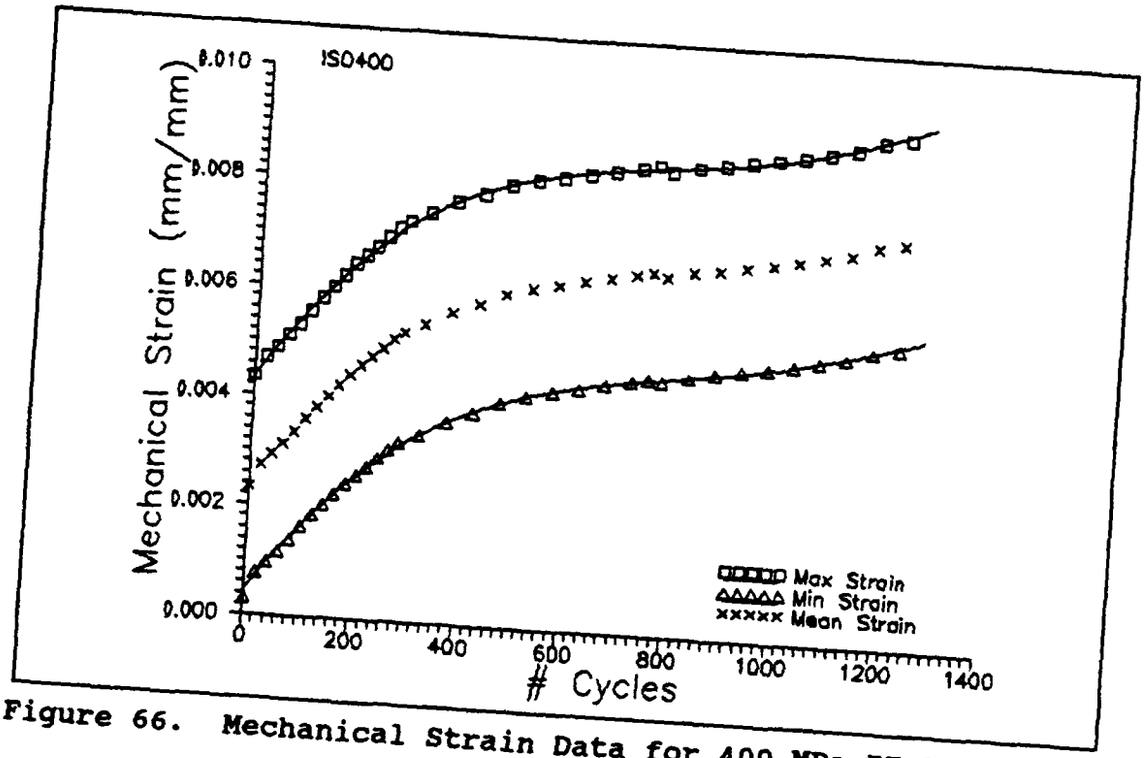

Figure 66. Mechanical Strain Data for 400 MPa IF Test

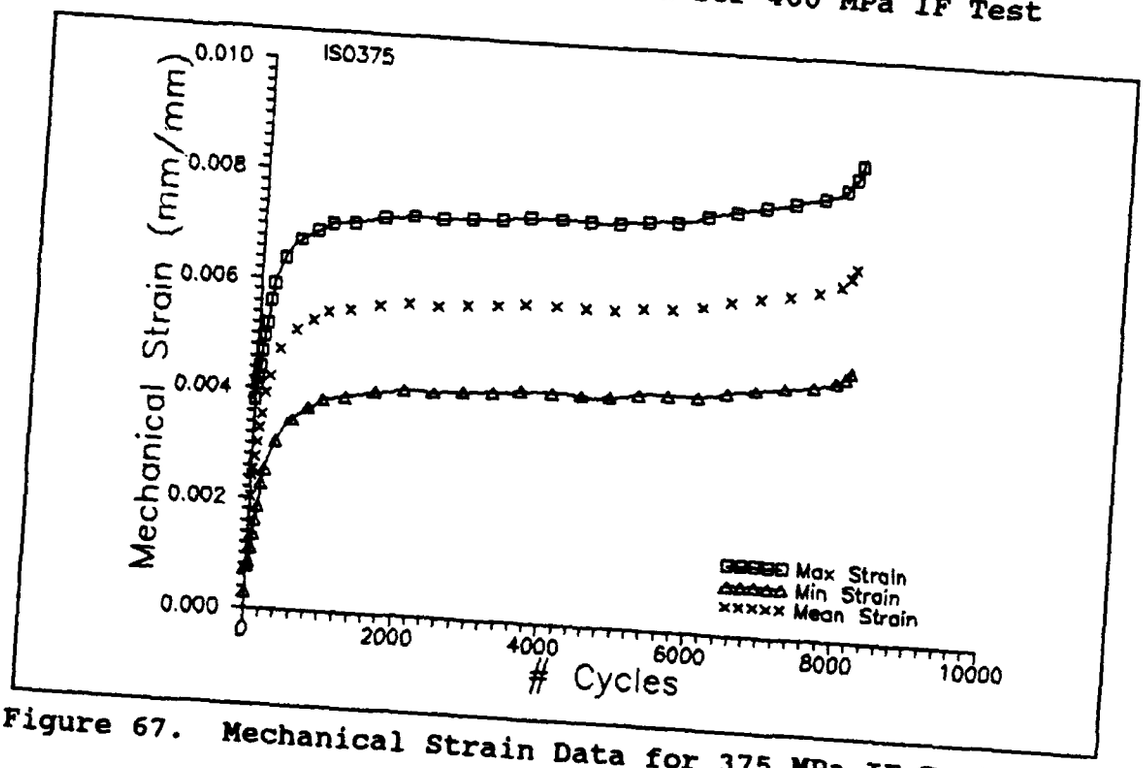

Figure 67. Mechanical Strain Data for 375 MPa IF Test

APPENDIX E

Constituent Micromechanical Stresses from METCAN

This appendix contains data used in the METal matrix Composite ANalyzer (METCAN) FORTRAN program developed by NASA Lewis Research Center. The program was developed to analyze fiber-reinforced metal matrix composites both in a linear mode and a nonlinear mode. For the purposes of this investigation, only the linear mode was implemented. METCAN works by utilizing unique equations that function as models of the constituents and the overall laminate (as discussed in Chapter II). Then, by properly orienting the plies, it estimates the engineering properties, stresses, and strains of the composite and plies for any loading profile established by the user.

The plots which follow are from two different METCAN versions. The first version uses a THERM2 subroutine while the other ignores it. This subroutine allows METCAN to apply three dimensional effects in calculating the residual stresses (derived from the difference between the coefficients of thermal expansion of the fiber and matrix). When THERM2 is ignored, METCAN reverts to ordinary strength of materials in determining these stresses.

The METCAN results have been plotted as Stress vs. Time Increment. The following describes the event during each increment for the three profiles used in this investigation:

A. In-Phase.

Time Increment	Event
0 - 1	Manufacturing cool down from 1000°C to 21°C
1 - 2	Applied load from 0 to R = 0.1 (minimum test level), increased temperature from 21°C to 149°C (minimum test level)
2 - 3	Increased load to maximum, R = 1.0, increased temperature to maximum, 427°C
3 - 4	Decreased load to minimum, decreased temperature to minimum
4 - 5	Increased load to maximum, increased temperature to maximum
5 - 6	Decreased load to minimum, decreased temperature to minimum

B. Out-of-Phase.

Time Increment	Event
0 - 1	Manufacturing cool down from 1000°C to 21°C
1 - 2	Applied load from 0 to R = 0.1 (minimum test level), increased temperature from 21°C to 427°C (maximum test level)
2 - 3	Increased load to maximum, R = 1.0, decreased temperature to minimum, 149°C
3 - 4	Decreased load to minimum, increased temperature to maximum
4 - 5	Increased load to maximum, decreased temperature to minimum
5 - 6	Decreased load to minimum, increased temperature to maximum

C. Isothermal

Time Increment	Event
0 - 1	Manufacturing cool down from 1000°C to 21°C
1 - 2	Applied load from 0 to R = 0.1 (minimum test level), increased temperature from 21°C to 427°C (maximum, constant test level)
2 - 3	Increased load to maximum, R = 1.0
3 - 4	Decreased load to minimum
4 - 5	Increased load to maximum
5 - 6	Decreased load to minimum

The next page contains all the fiber and matrix properties used in the DATABANK.DAT file. METCAN uses this data file as a library to hold engineering properties of various fibers like P100, SICA, SCS9 and SCS6, and of various matrices like ALT6, COPR, B21S, and TI15. Note that all the units are English. Also, the matrix modulus used in DATABANK.DAT was derived from the classical laminated plate theory as explained in Appendices A and B. All other properties were from previous studies.

METCAN Fiber Properties

Property	Units (METCAN)	SCS6
Df	mils	5.350
Rhof	lb/in**3	0.110
Tempmf	Deg. F	4780.
Ef11	Mpsi	57.30
Ef22	Mpsi	57.30
Nuf12	in/in	0.250
Nuf23	in/in	0.250
Gf12	Mpsi	22.90
Gf23	Mpsi	22.90
Alfaf11	Ppm/F	2.290
Alfaf22	Ppm/F	2.290
Kf11	Btu/hr/in/F	0.750
Kf22	Btu/hr/in/F	0.750
Cf	Btu/lb	0.290
Sf11T	Ksi	500.0
Sf11C	Ksi	650.0
Sf22T	Ksi	500.0
Sf22C	Ksi	650.0
Sf12S	Ksi	300.0
Sf23S	Ksi	300.0

METCAN Matrix Properties

Property	Units (METCAN)	TI15
Rhom	Lb/in**3	0.172
Em	Mpsi	8.100
Num	in/in	0.360
Alfam	Ppm/F	4.290
Km	Btu/hr/in/F	0.390
Cm	Btu/lb	0.120
SmT	Ksi	125.0
SmC	Ksi	125.0
SmS	Ksi	90.00
EpsmT	%	12.00
EpsmC	%	12.00
EpsmS	%	12.00
EpsmTOR	%	12.00
Kvoid	BTU/hr/in/F	0.019
Tempmm	Deg. F	3000.

The following plots give the resulting stresses from the in-phase, out-of-phase, and isothermal loading profiles for a maximum applied stress of 100 MPa. Since the analysis was run in the linear mode, one can multiply the results of time increment 2 and onward by the ratio of the true applied stress over the 100 MPa given (i.e. for 475 MPa, multiply the results by the ratio 475/100 or 4.75) to determine what the stresses would be for any applied stress level. The stresses at time increment 0 are considered to be zero (the composite is at an elevated temperature and in a stress free state). Also, the stresses at time increment 1 are the residual stresses and are independent of the applied load.

The first set of graphs are for METCAN with THERM2, the second set are for METCAN without THERM2.

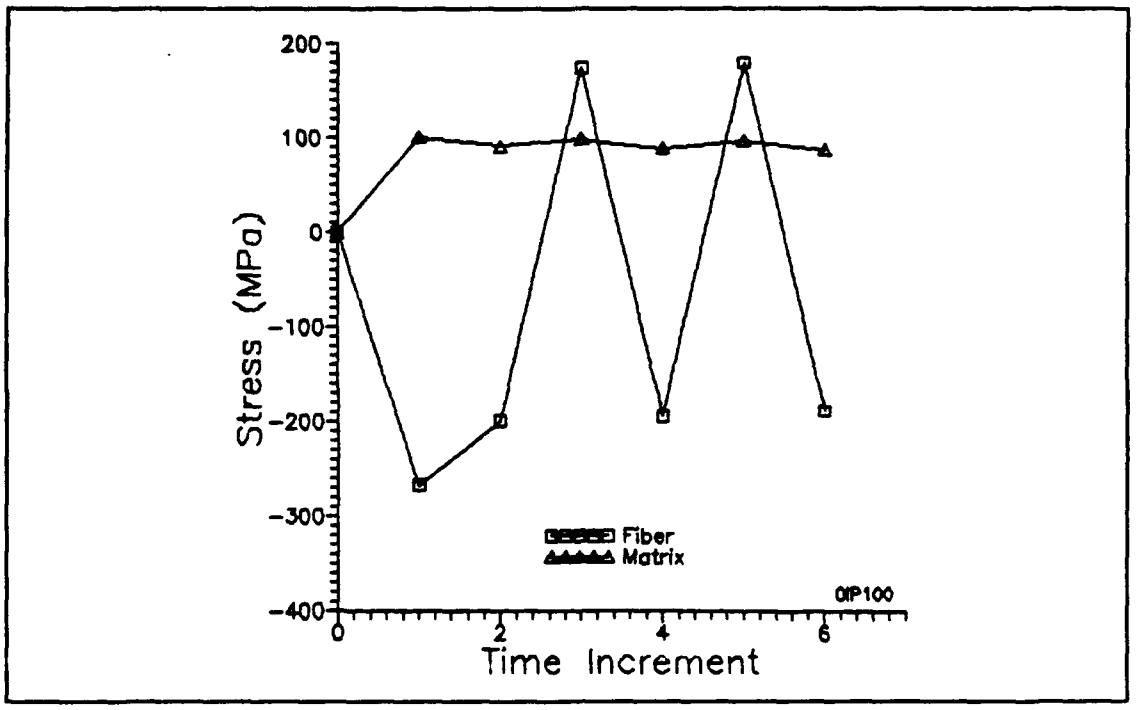

Figure 68. Maximum Stress, 100 MPa, IP, 0° Ply, w/THERM2

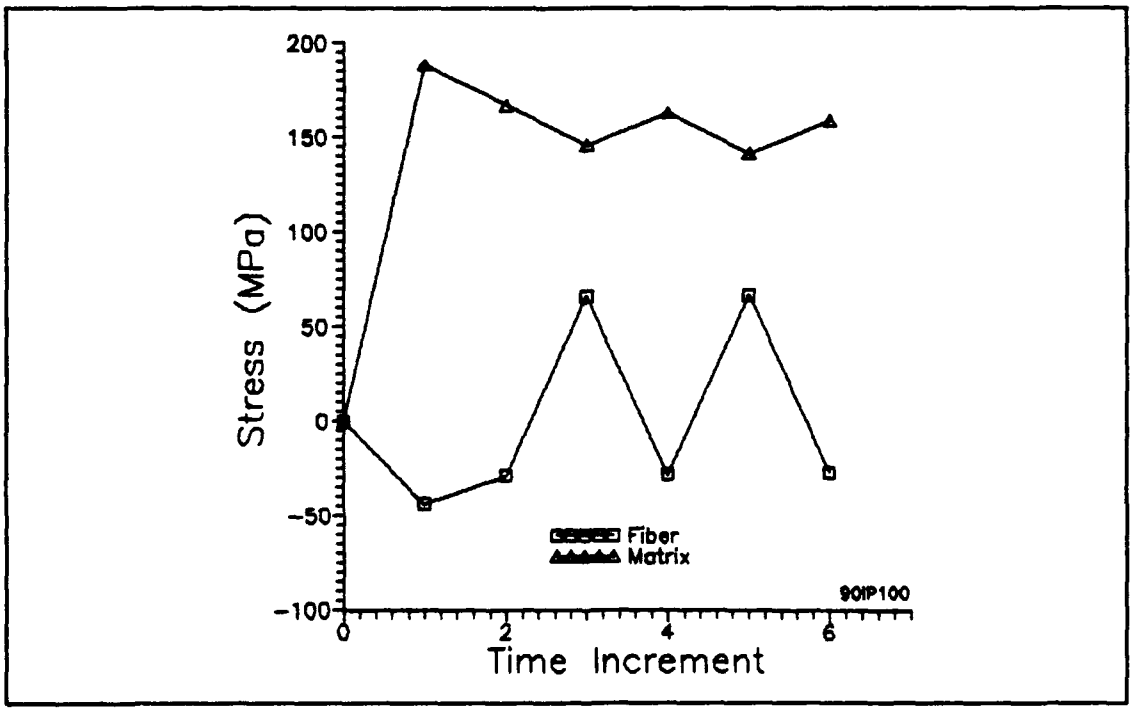

Figure 69. Maximum Stress, 100 MPa, IP, 90° Ply, w/THERM2

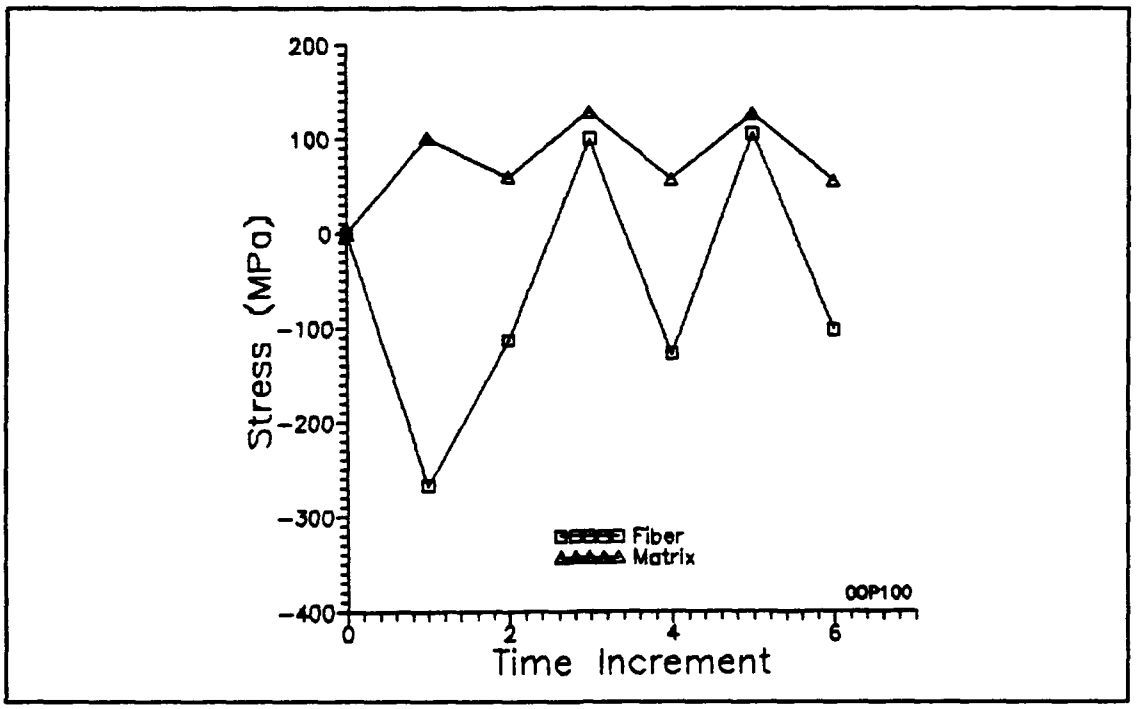

Figure 70. Maximum Stress, 100 MPa, OP, 0° Ply, w/THERM2

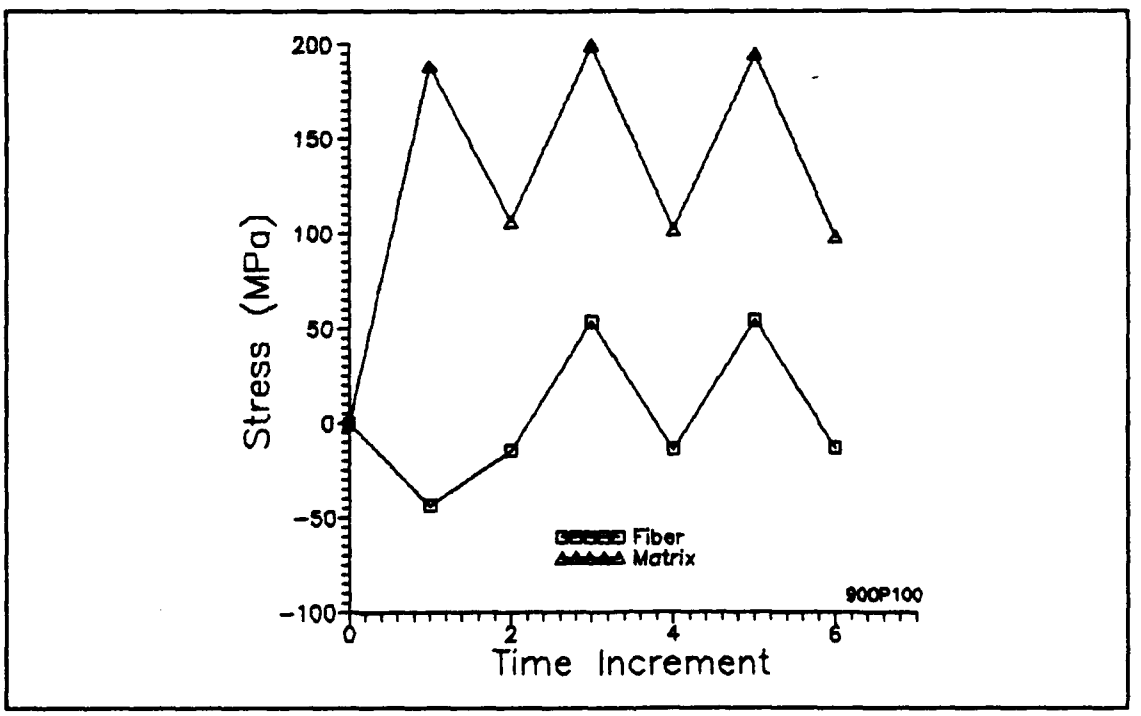

Figure 71. Maximum Stress, 100 MPa, OP, 90° Ply, w/THERM2

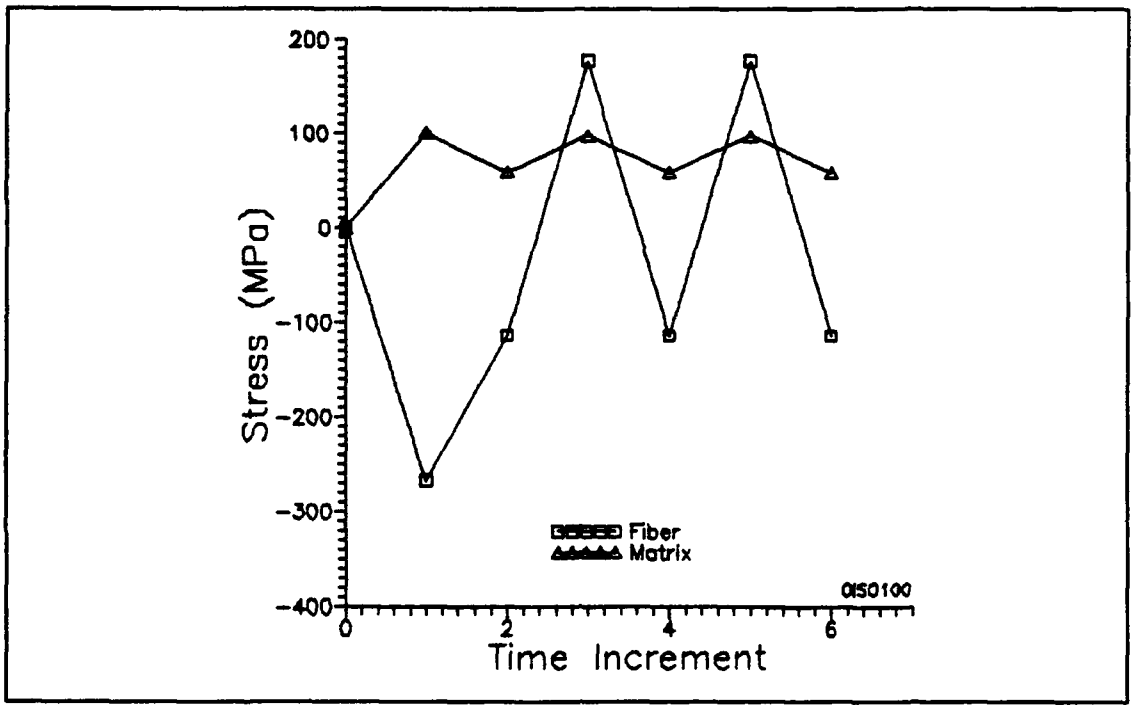

Figure 72. Maximum Stress, 100 MPa, IF, 0° Ply, w/THERM2

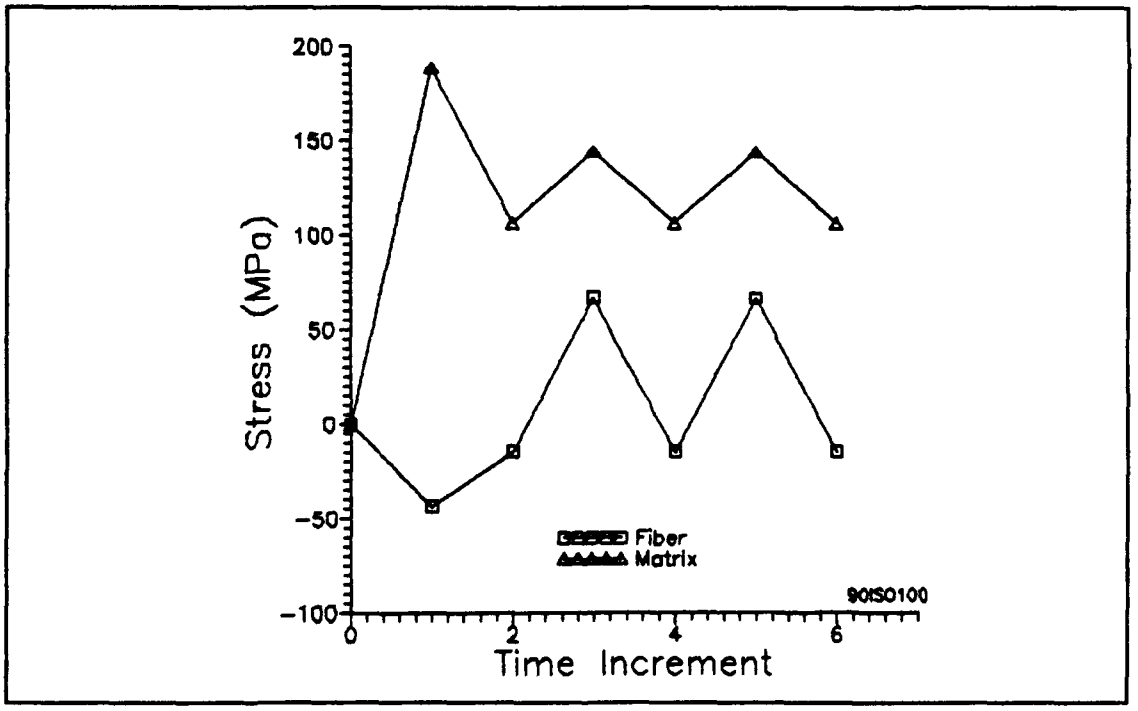

Figure 73. Maximum Stress, 100 MPa, IF, 90° Ply, w/THERM2

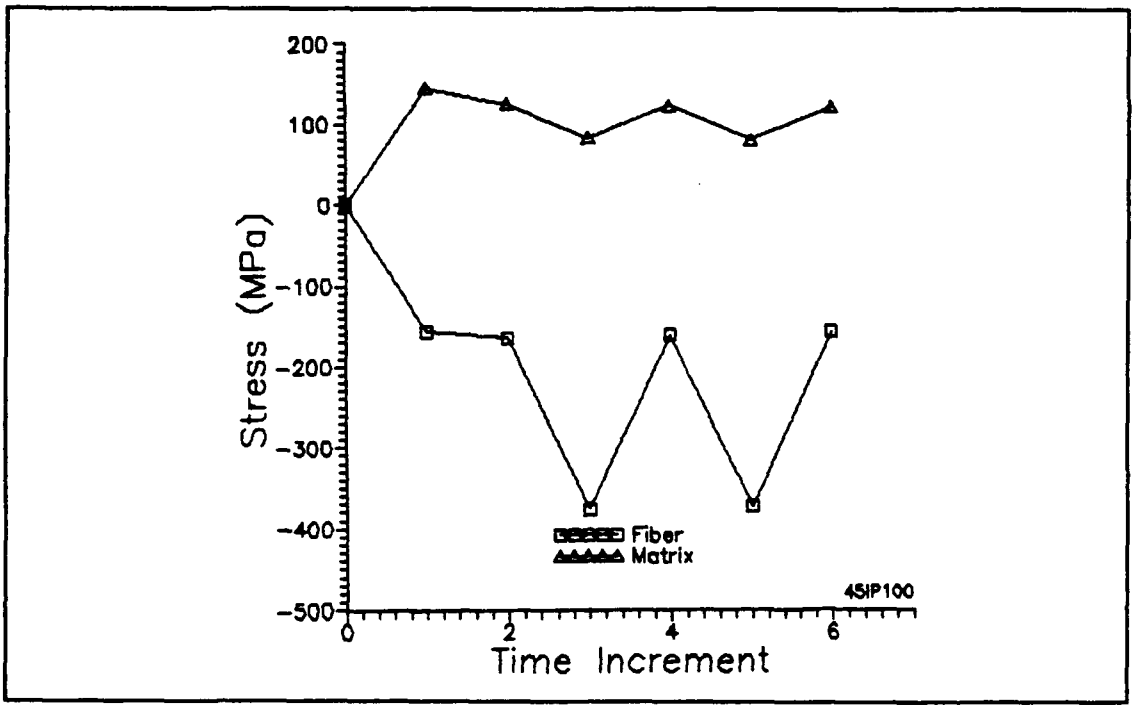

Figure 74. Maximum Stress, 100 MPa, IP, 45° Ply, w/THERM2

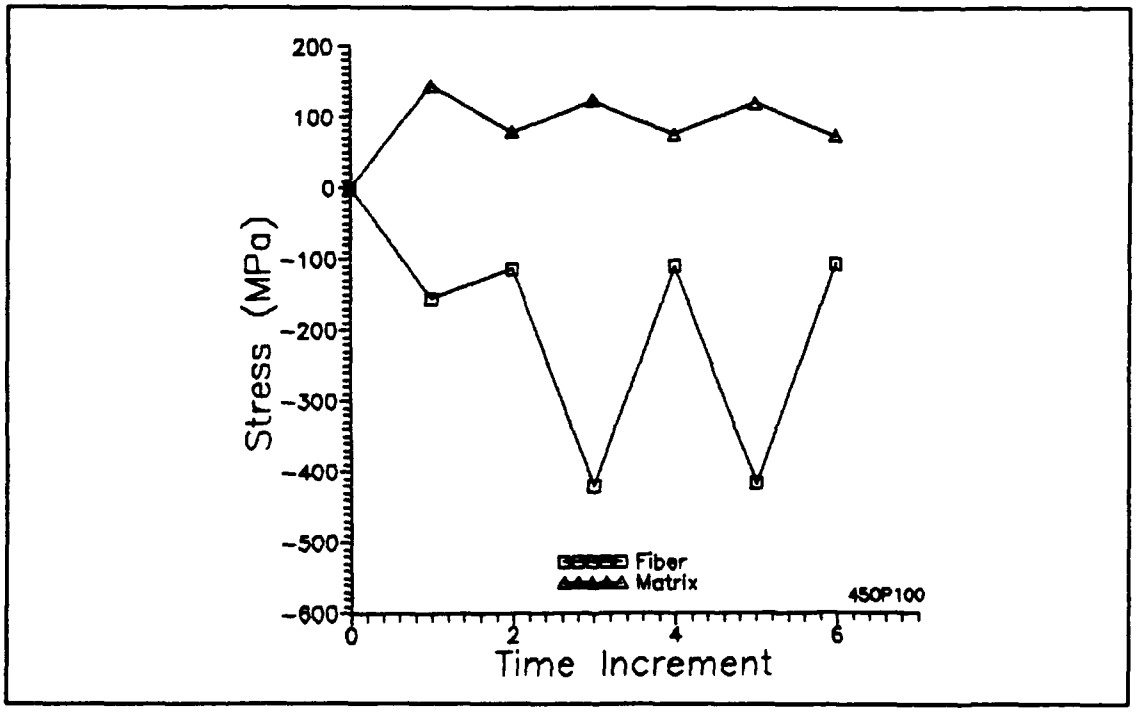

Figure 75. Maximum Stress, 100 MPa, OP, 45° Ply, w/THERM2

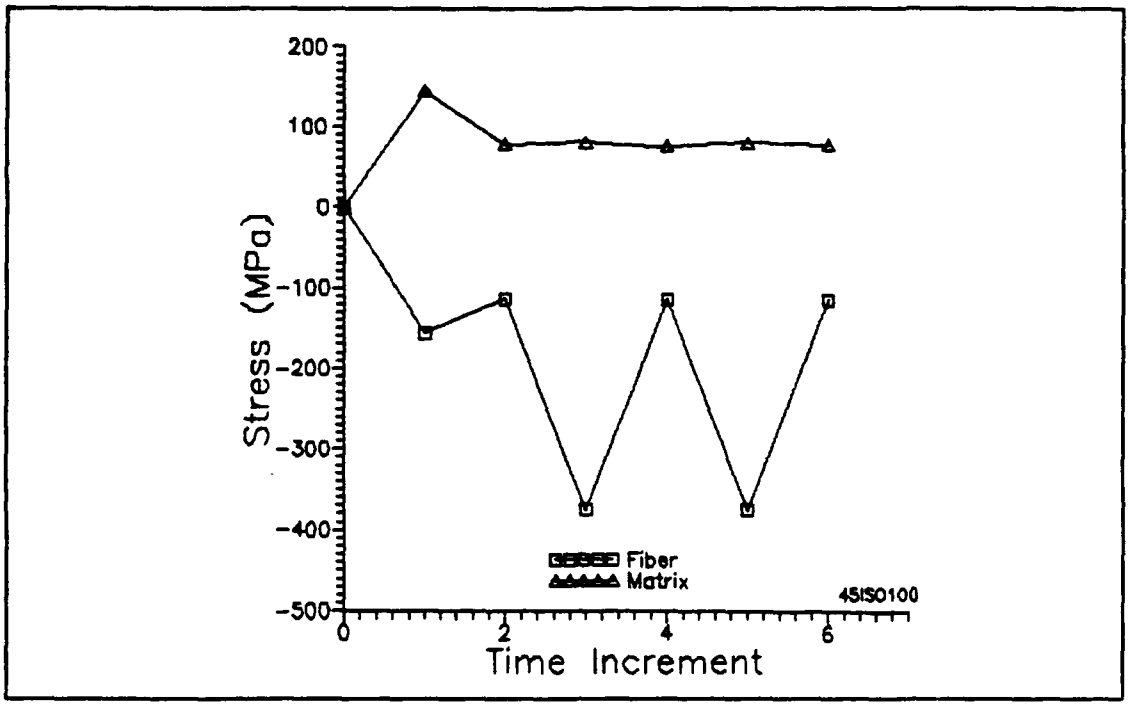

Figure 76. Maximum Stress, 100 MPa, IF, 45° Ply, w/THERM2

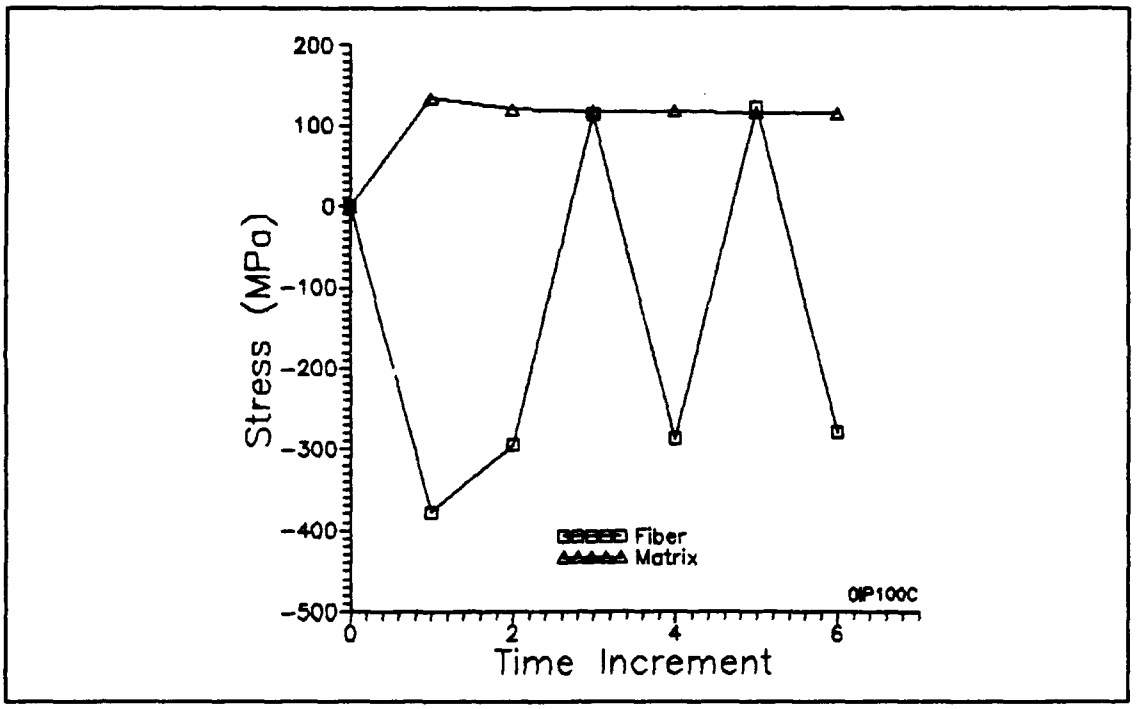

Figure 77. Maximum Stress, 100 MPa, IP, 0° Ply, w/o THERM2

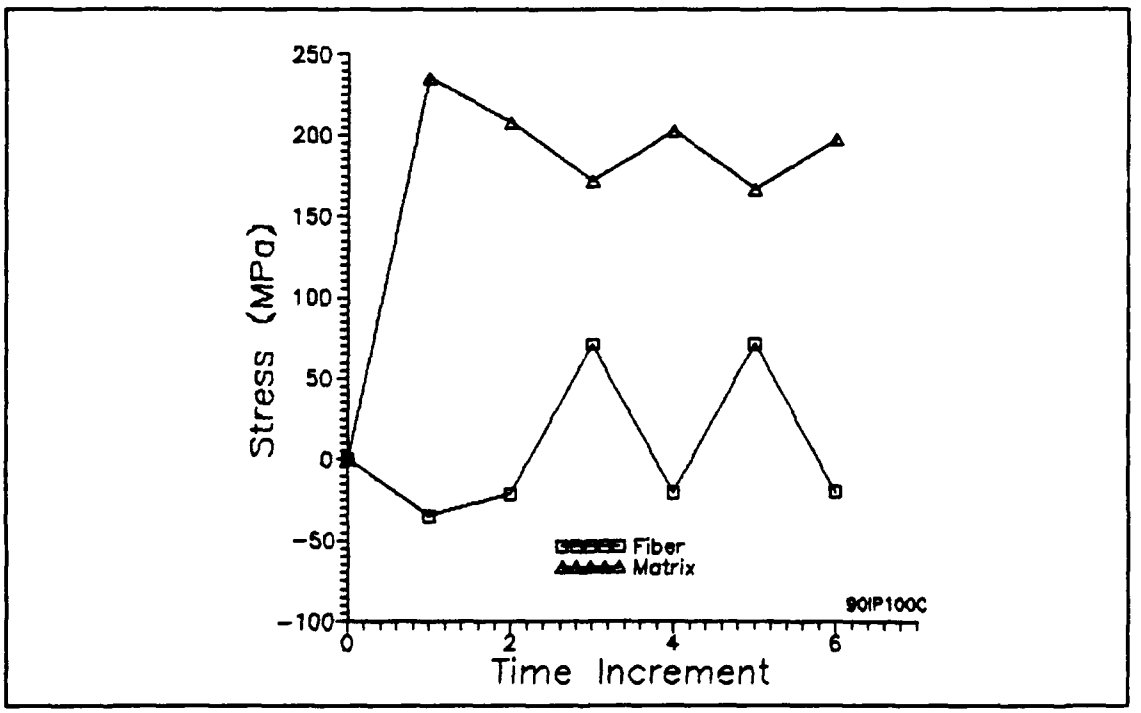

Figure 78. Maximum Stress, 100 MPa, IP, 90° Ply, w/o THERM2

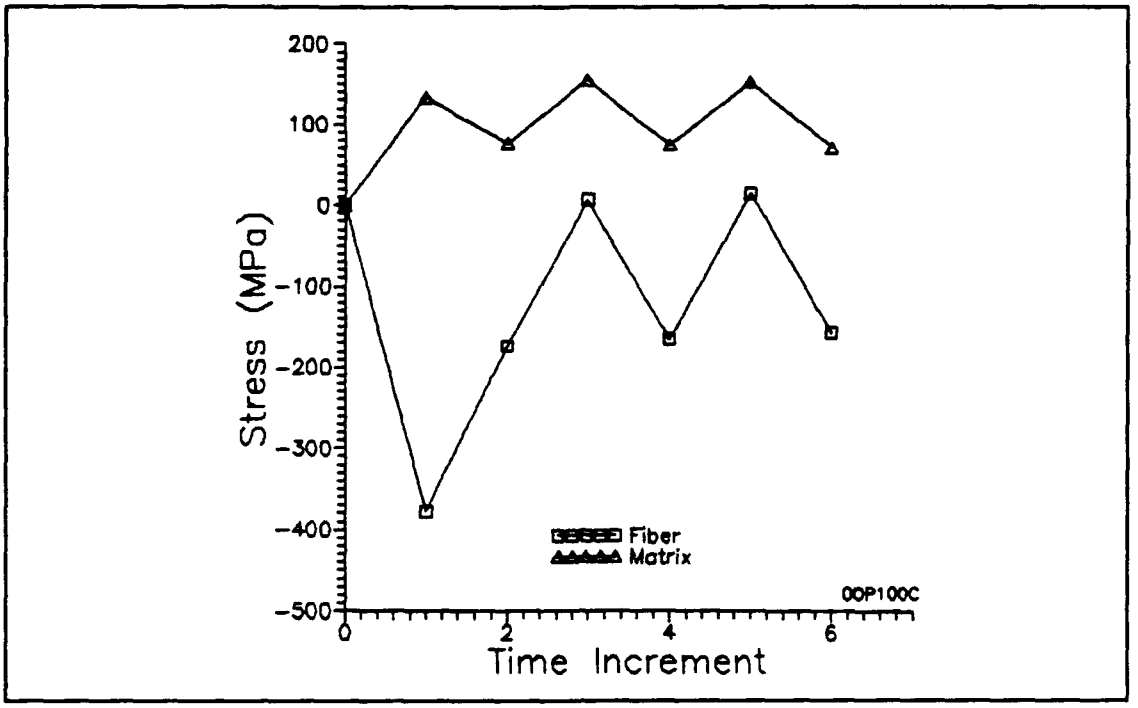

Figure 79. Maximum Stress, 100 MPa, OP, 0° Ply, w/o THERM2

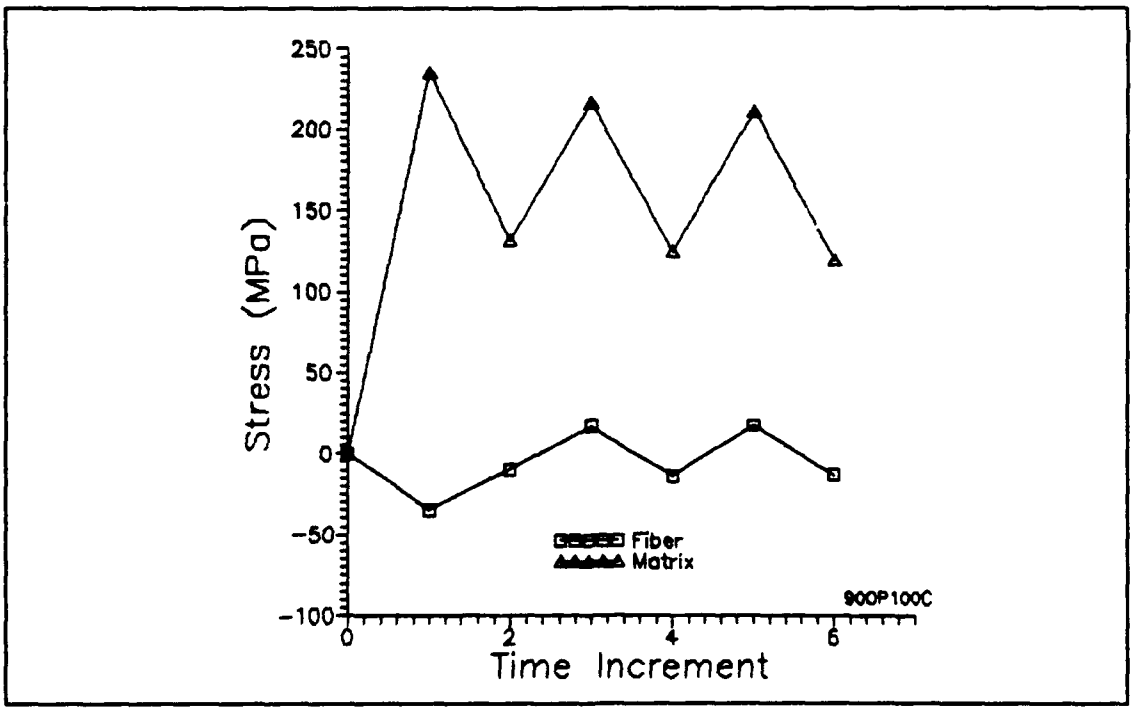

Figure 80. Maximum Stress, 100 MPa, OP, 90° Ply, w/o THERM2

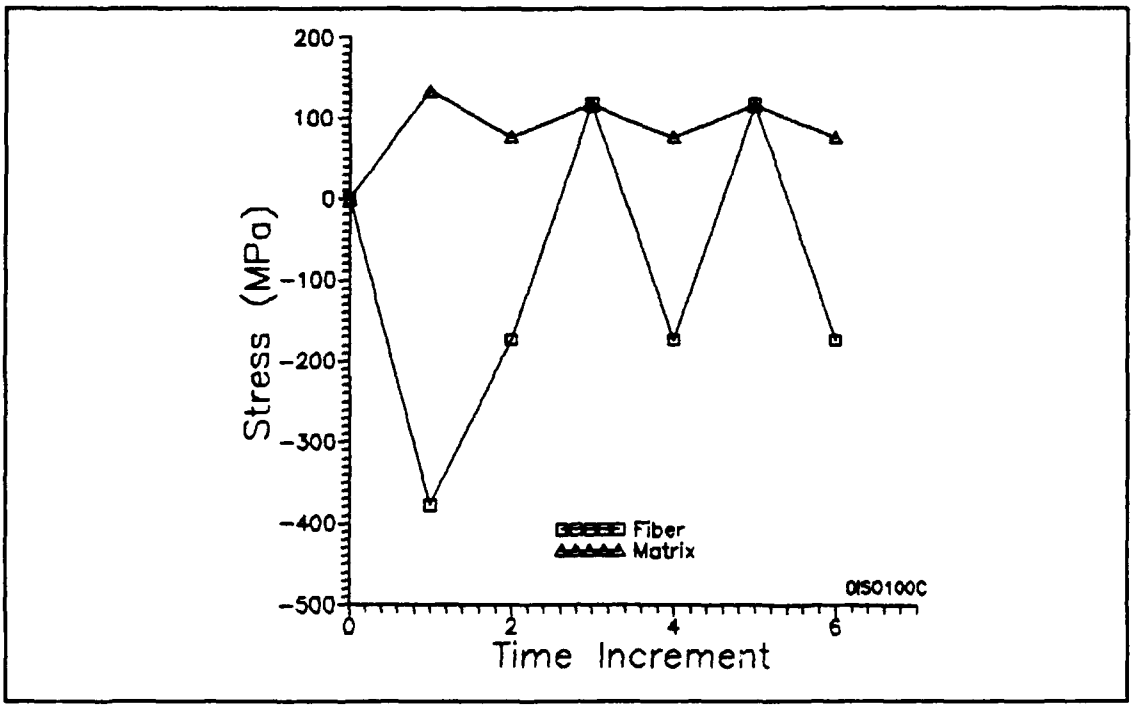

Figure 81. Maximum Stress, 100 MPa, IF, 0° Ply, w/o THERM2

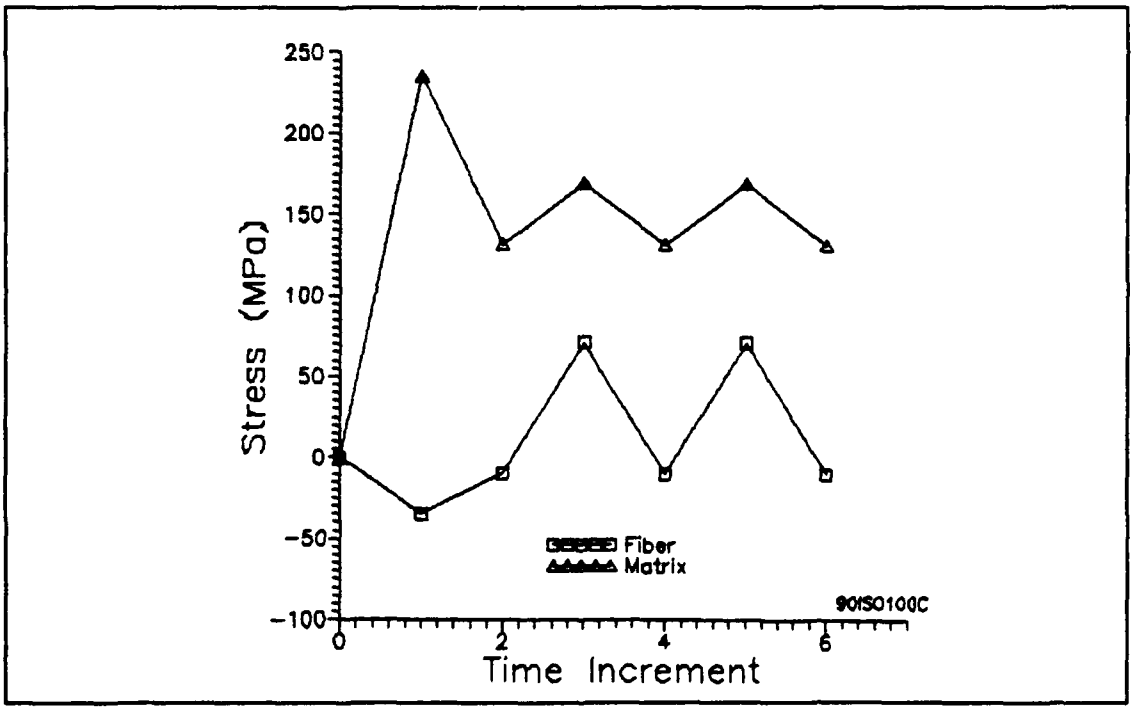

Figure 82. Maximum Stress, 100 MPa, IF, 90° Ply, w/o THERM2

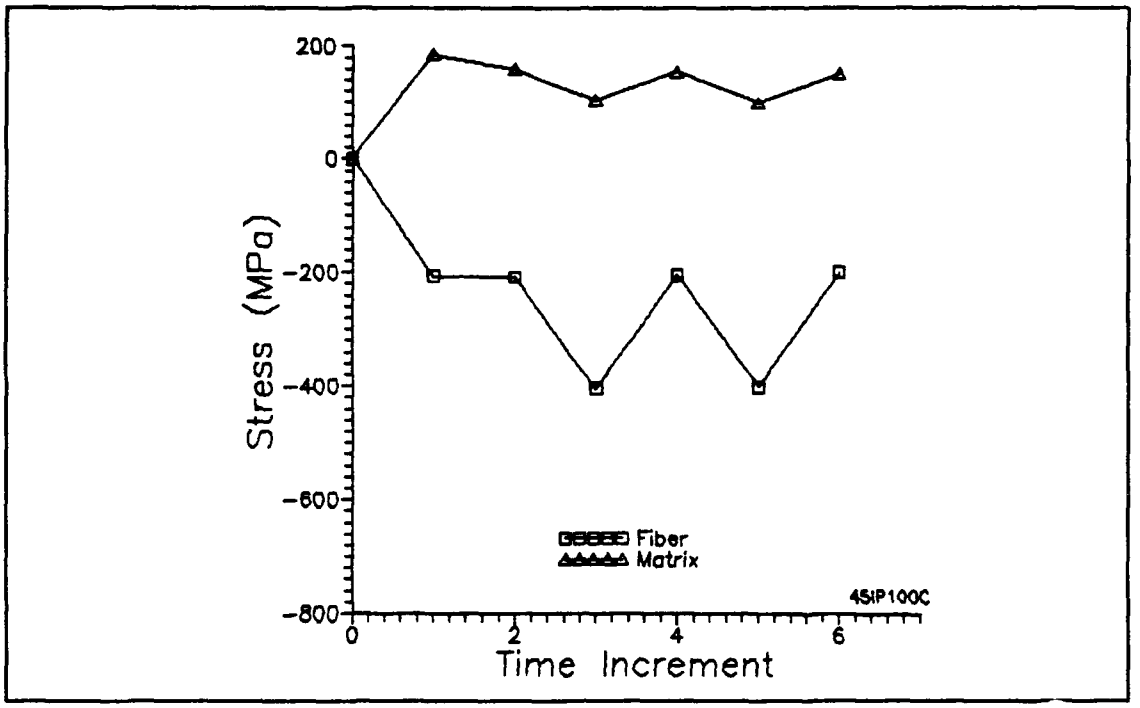

Figure 83. Maximum Stress, 100 MPa, IP, 45° Ply, w/o THERM2

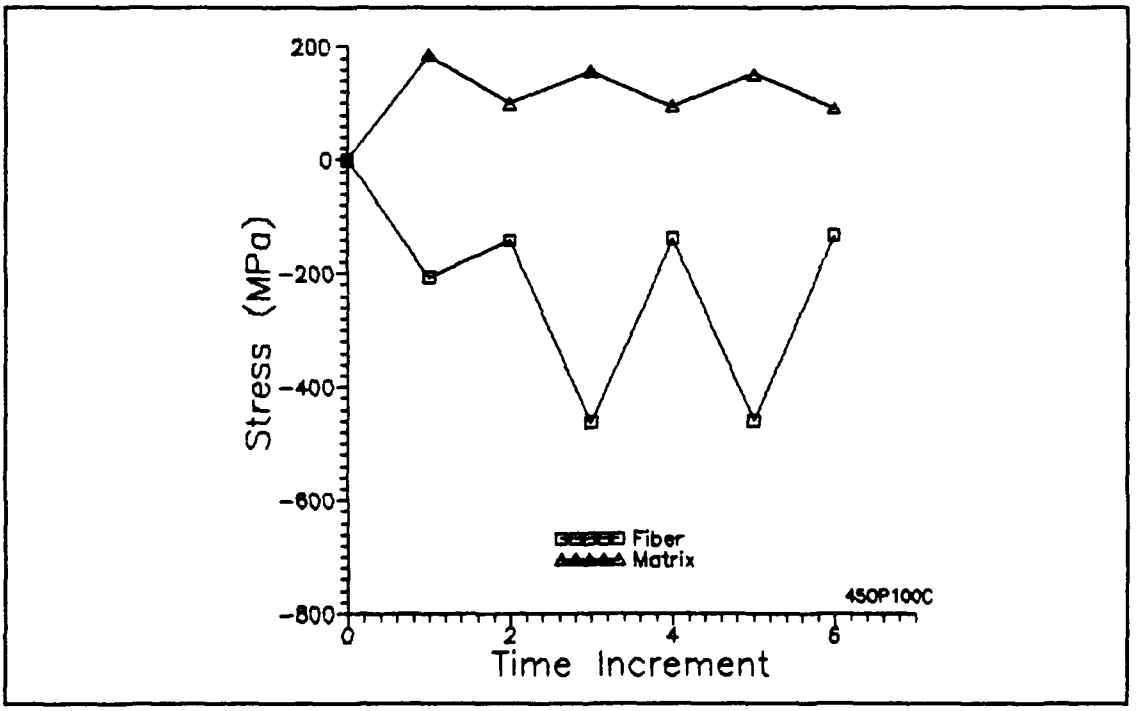

Figure 84. Maximum Stress, 100 MPa, OP, 45° Ply, w/o THERM2

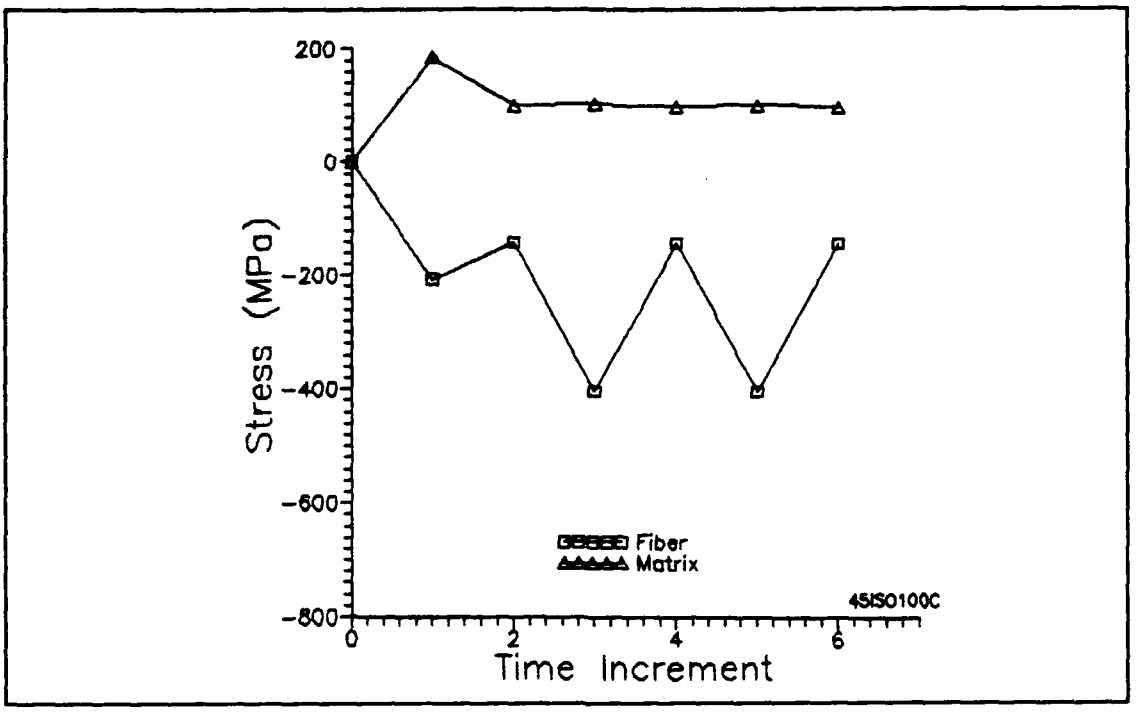

Figure 85. Maximum Stress, 100 MPa, IF, 45° Ply, w/o THERM2

Bibliography

1. Agarwal, B.D. and Broutman, L.J. Analysis and Performance of Fiber Composites. New York: John Wiley & Sons, Inc., 1990.

2. Bates, Mark A. Thermo-Mechanical Fatigue of a Fiber Reinforced Titanium Aluminide Composite. MS Thesis, AFIT/GAE/ENY/91S-1. School of Engineering, Air Force Institute of Technology (AU), Wright-Patterson AFB OH, March 1991.

3. Broek, David. Elementary Engineering Fracture Mechanics. Netherlands: Martnus Nijhoff Publishers, 1986.

4. Castelli, M.G. and others. "Thermomechanical Testing Techniques for High Temperature Composites: TMF Behavior of SiC(SCS_6)/Ti-15-3," Sverdrup Technology, Brook Park, Ohio/NASA Lewis Research Center, Cleveland, OH, Unpublished.

5. Ermer, Capt Paul G. Investigation of the Failure Modes in a Metal Matrix Composite Under Thermal Cycling. MS Thesis, AFIT/GAE/ENY/89D-07. School of Engineering, Air Force Institute of Technology (AU), Wright-Patterson AFB OH, December 1989.

6. Gabb, T. P. and other. "Isothermal and Nonisothermal Fatigue Behavior of a Unidirectional SiC/Ti Composite and the Ti Alloy Matrix," NASA TM-101984, April 1989.

7. Halpin, J.C. "Effects of Environmental Factors on Composite Materials," AFML-TR-67-423, June 1989.

8. Hanson, Dana G. Thermomechanical Fatigue of SCS-6/ß21-S $[0/90]_{2s}$ Composite. MS Thesis, AFIT/GAE/ENY/91D-9. School of Engineering, Air Force Institute of Technology (AU), Wright-Patterson AFB OH, December 1991.

9. Hopkins, D.A. and Chamis, C.C. "A Unique Set of Micromechanics Equations for High Temperature Metal Matrix composites," NASA TM-87154, November 1985.

10. Johnson, W. S., Lubowinski, S. J., and Highsmith, A. L., "SCS6-Ti-15-3 Metal Matrix Composites at Room Temperature," NASA TM-1014, April 1988.

11. Johnson, W. S., Lubowinski, S. J., and Highsmith, A. L., "Mechanical Characterization of Unnotched SCS6/Ti-15-3,

Metal Matrix Composites at Room Temperature," Presented at the ASTM Symposium, November 1988.

12. Lerch, B. and Saltsman, J. "Tensile Deformation Damage in SiC Reinforced Ti-15V-3Cr-3Al-3Sn," NASA TM 103620, April 1991.

13. Majumdar, Bhaskar S. and Golam M. Newaz. "ThermoMechanical Fatigue of a Quasi-Isotropic Metal Matrix Composite," Battelle Memorial Institute, Columbus, OH. Presented at the ASTM Third Symposium on Composite Materials: Fatigue and Fracture, November, 1989.

14. Majumdar, Bhaskar S. and Golam M. Newaz. "ThermoMechanical Fatigue Response and Damage in an Angle-Ply Metal Matrix Composite," Battelle Memorial Institute, Columbus, OH. Submitted to The Journal of Engineering Materials and Technology - ASME, October, 1989.

15. Mall, S. and Hanson, D.G. "Thermomechanical Fatigue Behavior of a Cross-Ply SCS-6/β21-S Metal Matrix Composite." AFIT, Wright-Patterson AFB OH. Unpublished and Undated.

16. Mall, S. and Schubbe, J.J. "Thermomechanical Fatigue Behavior of a Cross-Ply SCS6/Ti-15-3 Metal Matrix Composite." AFIT, Wright-Patterson AFB OH. Unpublished and Undated.

17. Metal Matrix Composite Analyzer, METCAN, Version 3.0, User's Guide. NASA Lewis Research Center, Cleveland OH, December 1989.

18. Mirdamadi, M., Johnson, W.S., and Castelli, M.G. "Analysis of Thermomechanical Fatigue of Unidirectional Titanium Metal Matrix Composites," NASA TM-104105, July 1991.

19. Pollack, W.D. and Johnson, W.S. "Characterization of Unnotched SCS-6/Ti-15-3 Metal Matrix Composites at 650°C," NASA TM-102699, September 1990.

20. Portner, Capt B. Investigation of Fatigue Damage Mechanisms in a Metal Matrix Composite Under Elevated Temperature. MS Thesis, AFIT/GAE/ENY/90D-20. School of Engineering, Air Force Institute of Technology (AU), Wright-Patterson AFB OH, December 1990.

21. Rattray, Capt J. Tensile Strength Characterization of a Metal Matrix Composite With Circular Holes. MS Thesis,

AFIT/GAE/ENY/91D-24. School of Engineering, Air Force Institute of Technology (AU), Wright-Patterson AFB OH, December 1991.

22. Russ, S.M. and others. "Thermomechanical Fatigue of SCS-6/Ti-24Al-11Nb Metal Matrix Composite," Failure Mechanisms in High Temperature Composite Materials, ASME AD-Vol. 22 and AMD-Vol. 122, 1991.

23. Schubbe, Capt J. Investigation of Damage Mechanisms in a Cross-Ply Metal Matrix Composite Under Thermo-Mechanical Loading. MS Thesis, AFIT/GAE/ENY/90D-26. School of Engineering, Air Force Institute of Technology (AU), Wright-Patterson AFB OH, December 1990.

24. Tsai, S.W. and Pagano, N.J. "Invariant Properties of Composite Materials" in Composite Materials Workshop edited by Tsai, Halpin, and Pagano, Technomic Publishing, Stamford, CT, 1968.

Vita

Captain Karl A. Hart was born on 15 November 1960 in Clearwater, Florida. He graduated from Central Catholic High School in Modesto, California in 1978. He then graduated from the California Polytechnic State University at San Luis Obispo, California in June 1983 with a Bachelor of Science degree in Aeronautical Engineering and Mechanical Engineering. He received his commission in October 1983 from the Air Force Officer Training School and served his first assignment at McClellan AFB CA. There, he worked as structural engineer for the A-7, A-10, F-4, and F-106 aircraft. Capt Hart's second assignment brought him to the Aeronautical Systems Division at Wright Patterson AFB OH where he was selected to serve as the lead structural engineer for the Advanced Cruise Missile from September 1989 to May 1991. He entered the School of Engineering, Air Force Institute of Technology, in June 1991.

Permanent Address: 3613 Camino Real
Modesto CA 95356

REPORT DOCUMENTATION PAGE

Form Approved
OMB No. 0704-0188

1. AGENCY USE ONLY (Leave blank)	2. REPORT DATE	3. REPORT TYPE AND DATES COVERED
	DEC 92	Master's Thesis

4. TITLE AND SUBTITLE
Behavior of a Quasi-Isotropic Ply Metal Matrix Composite Under Thermo-Mechanical and Isothermal Fatigue Loading

5. FUNDING NUMBERS

6. AUTHOR(S)
Karl A. Hart, Captain, USAF

7. PERFORMING ORGANIZATION NAME(S) AND ADDRESS(ES)
Air Force Institute of Technology, WPAFB OH 45433-6583

8. PERFORMING ORGANIZATION REPORT NUMBER
AFIT/GAE/ENY/92D-05

9. SPONSORING/MONITORING AGENCY NAME(S) AND ADDRESS(ES)
Dr. Walter F. Jones
AFOSR/NA
Bolling AFB DC 20322-6448

10. SPONSORING/MONITORING AGENCY REPORT NUMBER

11. SUPPLEMENTARY NOTES

12a. DISTRIBUTION/AVAILABILITY STATEMENT
APPROVED FOR PUBLIC RELEASE; DISTRIBUTION UNLIMITED

12b. DISTRIBUTION CODE

13. ABSTRACT *(Maximum 200 words)*

This study investigated the behavior of the SCS6/Ti-15-3 metal matrix composite with a quasi-isotropic layup when tested under static and fatigue conditions. Specimens were subjected to in-phase and out-of-phase thermo-mechanical and isothermal fatigue loading. In-phase and isothermal loading produced a fiber dominated failure while the out-of-phase loading produced a matrix dominated failure. Also, fiber domination in all three profiles was present at higher maximum applied loads and all three profiles demonstrated matrix domination at lower maximum applied loads. Thus, failure is both profile dependent and load dependent. Additional analyses, using laminated plate theory, Halpin-Tsai equations, METCAN, and the Linear Life Fraction Model (LLFM), showed: the "as-received" specimens contained plies where a portion of the fibers are debonded from the matrix; during fatigue cycling, the 90^{0} plies and a percentage of the 45^{0} plies failed immediately with greater damage becoming evident with additional cycles; and, the LLFM suggests that there may be a non-linear combination of fiber and matrix domination for in-phase and isothermal cycling.

14. SUBJECT TERMS	15. NUMBER OF PAGES
Metal Matrix Composites, SCS6/Ti-15-3, Silicon Carbide Fiber, Titanium Matrix, Thermomechanical Fatigue, Isothermal Fatigue, Quasi-Isotropic Layup	170
	16. PRICE CODE

17. SECURITY CLASSIFICATION OF REPORT	18. SECURITY CLASSIFICATION OF THIS PAGE	19. SECURITY CLASSIFICATION OF ABSTRACT	20. LIMITATION OF ABSTRACT
Unclassified	Unclassified	Unclassified	UL